UNIVERSITY
OF TRENTO - Italy
DEPARTMENT OF INDUSTRIAL ENGINEERING

XXXV cycle

Doctoral School in Materials, Mechatronics
and Systems Engineering

Exploring the Potential of Polymer-Ceramic Nanocomposites for Energy Harvesting: The Role of Particle Functionalization in Enhancing Dielectric and Piezoelectric Properties

Nico Zamperlin

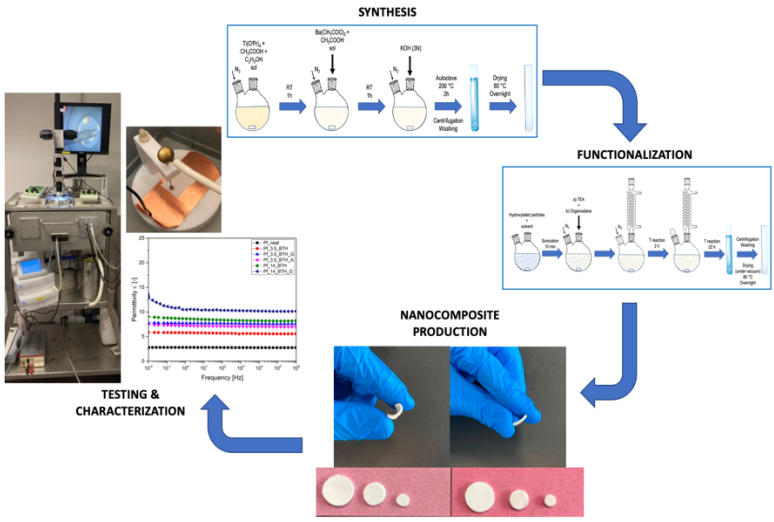

July 2023

UNIVERSITY OF TRENTO

Department of Industrial Engineering

Doctoral School in Materials, Mechatronics, and System Engineering (MMSE)

Exploring the Potential of Polymer-Ceramic Nanocomposites for Energy Harvesting: The Role of Particle Functionalization in Enhancing Dielectric and Piezoelectric Properties

PhD Candidate

Nico Zamperlin

Supervisors:

Prof. Sandra Dirè

Department of Industrial Engineering, *University of Trento, Trento, Italy*

Prof. Alessandro Pegoretti

Department of Industrial Engineering, *University of Trento, Trento Italy*

Prof. Marco Fontana

Institute of Mechanical Intelligence, *Sant' Anna School of Advanced Studies, Pisa, Italy*

Acknowledgments

Completing this thesis has been one of the most challenging achievements of my life, and I couldn't have done it without the support of numerous individuals. I am particularly grateful to my esteemed supervisors, Prof. Dirè, Prof. Pegoretti, and Prof. Fontana, for their invaluable guidance and mentorship throughout my Ph.D. A particular thanks is directed to Prof. Dirè for her exceptional mentorship which has helped me grow not only as a researcher but also as a person. I also want to express my appreciation to Prof. Sylvestre for hosting me during my time in France, it has been a very proficient collaboration and I hope it will continue throughout the years. I also want to thank the research team of the Chemistry Lab, Dr. Emanuela Callone and Prof. Francesco Parrino, for their technical support throughout my studies. Additionally, I am grateful to the University of Trento's Department of Industrial Engineering for funding my Ph.D. I am also deeply thankful to my friends, colleagues, and lab mates for their support over the years.

Last but not least, I want to express my immense gratitude to my parents and my sister, whose unwavering understanding and encouragement have been instrumental in my completion of this thesis.

Sincerely,
Nico

Summary

List of Acronyms and Nomenclature

APEOTES: 2-[acetoxy-(polyethyleneoxy)propyl]triethoxysilane
APTES: aminopropyltriethoxysilane
ATR: Attenuated Total Reflectance
B_0: Magnetic Field
BOS: 1,8-bis(triethoxysilyl)octanosilane
BT: Barium Titanate (sol-gel at ambient pressure)
BTC: commercial barium titanate
BTESPT: bis[3-(triethoxysilyl)propyl]tetrasulfide
BTH: hydrothermal barium titanate
CPMAS: Cross Polarization Magic Angle Spinning
CPMG: Carr-Purcell-Meiboom-Gill
d_{33}: piezoelectric charge constant
DC: Direct Current
DE: Dielectric Elastomer
DEDPS: diethoxydiphenylsilane
DEG: Dielectric Elastomers Generators
DGEBA: Diglycidyl ether bisphenol-A
DS: Dielectric Spectroscopy
E_{BD}: Dielectric breakdown
e_c: convertible energy density
EDXS: Energy-Dispersive X-ray Spectroscopy
FE-SEM: Field Emission Scanning Electron Microscopy
FTIR: Fourier Transform InfraRed
g_{33}: piezoelectric voltage constant
GO: Graphene Oxide
GPTMS: 3-glycidyloxypropyltrimethoxysilane
HV: High Voltage
ICP-OES: Inductive Coupled Plasma – Optical Emission Spectroscopy
k_{33}: electromechanical coupling factor
M: Magnetization
MEMS: Micro Electric Mechanical Systems
MT: Magnesium Titanate
MTES: Methyltriethoxysilane
MW: Molecular Weight
MWS: Maxwell-Wagner-Sillars
N_A: Avogadro Number
NBR: Acrylonitrile Butadiene Rubber
NMR: Nuclear Magnetic Resonance
NR: Natural Rubber
PD: polydopamine
PDMS: polydimethylsiloxane
PEO: Polyethylene oxide

PFOS: 1H, 1H, 2H, 2H - perfluorooctyltriethoxysilane
PMMA: Polymethylmethacrylate
PMVS: poly-dimethyl(vynilmethyl)silane
PP: Polypropylene
PS: Polystyrene
P_s: spontaneous polarization
PTES: phenyltriethoxysilane
PTFE: Polytetrafluoroethylene
PVDF: Poly-vynildienefluoride
PZT: Lead Zirconate Titanate
RF: Radiofrequency
RT: Room Temperature
S/N: Signal to Noise ratio
SA: Stearic acid
SE: Secondary Electrons
SSA: Specific Surface Area
STD: Standard Sample
T_c = Curie Temperature
TEA: triethylamine
TEOS: tetraethylortosilicate
TESPEOD: triethoxysilylpropoxy(polyethyleneoxy)dodecanoate
Teta: triethylenetetraamine
T_g: Glass Transition Temperature
TGA: Thermogravimetric Analysis
U_e: energy density
UV: Ultraviolet
XPS: X-Ray Photoelectron Spectroscopy
XRD: X-Ray Diffraction
ε_0: vacuum permittivity
ε_r: relative dielectric permittivity

List of Figures

List of Tables

Abstract

The demand for portable and wireless electronic devices, coupled with the need to decrease reliance on non-renewable energy sources, has led to an increased need for energy harvesting and piezoelectric materials. Energy harvesting materials can transform ambient energy into usable electrical energy, but their performance is often limited by their intrinsic properties. To overcome these limitations, nanocomposites have emerged as a promising solution. These composites consist of a polymeric matrix coupled with a high-performance dielectric/piezoelectric phase, which enhances their mechanical and electrical properties. The interface between the polymer matrix and the ceramic filler plays a crucial role in achieving the desired properties and performance of the composite material. Several methods, including surface modification of the ceramic filler and functionalization of the polymer matrix, have been developed to control the interface.

This thesis focuses on producing a composite material with high dielectric and piezoelectric properties through a simple and fast production route. Barium titanate ($BaTiO_3$) ceramic nanoparticles are synthesized via wet chemical methods and then embedded into different polymeric matrices to produce nanocomposites. The synthesis parameters for the ceramic nanofillers are optimized to obtain a highly homogeneous final product with a narrow size distribution. The fillers are characterized both structurally and microstructurally through several spectroscopic techniques such as FTIR (Fourier-Transform Infrared Spectroscopy), XRD (X-Ray Diffraction), and SEM (Scanning Electron Microscopy). Then, to enhance their compatibility with the matrix, they are subjected to hydroxylation treatment and functionalized with different organosilanes and characterized. The effectiveness of the functionalization is evaluated through various techniques, proving a successful reaction with high grafting degree for all samples. The particles are then dispersed in epoxy resin and PDMS (polydimethylsiloxane), and nanocomposites are produced with a process that involves the simultaneous application of both heat and electric field and the impact of the presence of surface coupling agents on the particle dispersibility is evaluated through SEM and EDXS (Energy Dispersive X-Ray Spectroscopy). Then, being PDMS the most suitable candidate for the intended applications, an extensive electric and dielectric characterization is carried out on PDMS-based composites through

dielectric spectroscopy in a wide range of frequencies and temperatures and measuring the dielectric breakdown strength to evaluate the energy density of the samples and their suitability for energy harvesting applications. To summarize, the incorporation of organosilanes leads to the creation of stronger interfaces, which result in the production of composites with high dielectric constant, good dielectric breakdown, and improved energy density values, even with lower filler content compared to similar studies. These organosilanes are responsible for activating different polarization mechanisms.

Despite the challenges that still need to be addressed, the development of energy harvesting, and piezoelectric materials based on nanocomposites has the potential to revolutionize the way we power electronic devices that can be successfully used in applications such as wearables, soft robotics, sensors, and actuators. Overall, this work unveils the significant potential of dielectric nanocomposites in various applications and highlights the need for continued research and development in this field.

Introduction

1.1 Piezoelectricity and Energy Harvesting: State of the Art

The progress in low-power electronics, MEMS (Micro Electro Mechanical Systems), sensors, and wearable devices made in the last two decades resulted in a growing interest in piezoelectric and energy-harvesting materials [1–3].

Sensors based on piezoelectric materials are widely used in different fields of application. Piezoelectric materials have been successfully and efficiently used in structural health monitoring: for example, PZT (Lead Zirconate Titanate) patches and PZT-based monitoring circuits are successfully used to detect structural damages in buildings and/or aircraft thanks to electromechanical impedance techniques or to impact monitoring [4,5]. More recently (2022) Nguyen et al.[6] developed a smart polyurethane activate (PUA) – $BaTiO_3$ printable piezoelectric composite for the condition monitoring of bearings that were demonstrated to measure the substrate deformations reliably thanks to piezoelectric electromechanical coupling. Piezoelectric sensors based on laminated PVDF (polyvinyldenefluoride) films have also been recently used by Kalantarian et al. [7] to effectively monitor and evaluate eating habits.

On the other hand, the abrupt increase in the use of wearable devices pushed researchers to find new solutions, with very high performances in terms of power density, lifetime, and so on. All these devices require energy to work properly: energy harvesting materials are a class of materials that can convert energy from different sources into electrical energy [2,8]. Depending on the material and the application, they can convert energy from thermal energy, electromagnetic energy, mechanical vibrations, mechanical stretching/deformation, piezoelectric effect, or triboelectric effect into electrical energy [8–11]. The stored energy can be used to power the devices and allow their correct functioning. For example, the human body offers many possibilities to harvest energy from its movement and in this sense, a pioneering work in 2001 by an MIT research team opened the possibility to scavenge energy from walking by putting piezoelectric materials in shoes [12]. This idea was then picked up and improved throughout the years: Moro et Benasciutti in 2010 designed a piezoceramic (using PZT-5A) energy harvester in a cantilever configuration achieving a maximum power of around 0.4 mW

per footstep [13] while, more recently, in 2014, Zhao and You were able to improve the power output to 1 mW using a PVDF based energy harvester [14]. Also, the new trends in medicine, are pushing researchers to find new solutions, for example, MEMS can be used to harvest energy to allow the correct functioning of pacemakers; in 2016 Abidin et al.[15] developed an interdigitated MEMS supercapacitor based on SiO_2, polypyrrole, and polyvinylalcohol (PVA) to prolong the battery lifetime of pacemakers.

In addition to that, the never-ending growing demand for energy from renewable sources is opening new research topics or expanding older ones. Here, wind and wave energy harvesting are two hot topics: for example, in 2018 Moretti et al.[16] modeled and tested a wave energy converter based on dielectric elastomer generators (DEG), while in 2018 Wang et al. [17] developed a cantilever-shaped bio-inspired piezoelectric wind energy harvester, based on polypropylene-PVDF, with power densities up to 3.5 $\mu W/cm^3$.

All the previous examples demonstrate why piezoelectric materials and materials for energy harvesting are gaining attention during the last years.

In this work, the focus will be on the production of polymer-ceramics composites to convert and harvest energy by exploiting the piezoelectric effect and mechanical deformation. The final piezoelectric harvesting performance of materials depends on many factors that must be optimized, among them:

- Dielectric constant (ε_r)
- Dielectric breakdown (E_{BD})
- Piezoelectric charge coefficient (d_{33}, d_{31})
- Piezoelectric voltage coefficient (g_{33}, g_{31})
- Electromechanical coupling factor (k_{33})
- Loss factor

These properties refer to different characteristics of dielectric and piezoelectric materials and will be discussed in detail in the next paragraphs.

The current limits of polymer-ceramic composites are mainly related to their low dielectric constant, low electromechanical coupling factor, and dielectric breakdown reduction; in

composites, these issues can be addressed to different factors such as big differences in the dielectric constant of matrix and particles, characteristics of the particles (size, distribution, morphology) and particle-matrix interactions [18,19]. For example, the higher permittivity of the filler with respect to the polymeric matrix will result in highly inhomogeneous electric fields inside the composite [18]. Furthermore, the distorted and enhanced local electric field due to the presence of microparticles can also reduce the breakdown strength of composites as reported by Shen et al. [20]. Again, the size of the fillers plays a crucial role in the dielectric properties. Sun et al. [21] tested the dielectric properties of epoxy/(nano/micro) silica composites and observed higher permittivity (accompanied by a higher loss factor) in nanocomposites with respect to micro composites, especially at lower frequencies. For Lewis, these effects are due to the fact that by decreasing the filler size down to the submicrometric and nanometric region the properties of the polymer-ceramic interfaces are preponderant concerning the properties of the single constituents [22,23]. In this scenario, it is clear that also the particle-matrix interaction plays a crucial role. In fact, a poor filler-matrix interaction can result in lower particle dispersibility, cluster formation, and micro/macro-defectiveness of the final samples. Furthermore, these defects can strongly affect dielectric properties and the load-transfer capability of the final material. For example, Li et al. [18] demonstrated that nanoparticles can improve the long-term breakdown failure properties of composites, but the presence of nanoparticle aggregates can strongly affect the short-term breakdown performance of composites.

To these findings, acting on the filler size and aspect ratio and also on the chemistry of the interfaces between fillers and matrices could lead to the creation of stronger filler-matrix interactions resulting in higher materials' performance. The control of matrix-filler interaction is very important both for piezoelectric and energy harvesting applications, in fact, a proper matrix-filler interface can enhance the piezo- and dielectric performance of the final product [24–26]. These are the main reasons behind research on the chemistry of interfaces.

Believing that the control of the surface chemistry and interfaces can help to produce composites with high dielectric and piezoelectric properties, this thesis aims to produce a high-performance nanocomposite material for piezoelectric and dielectric applications (flexible sensor, energy harvesting) with a bottom-up approach. The project starts with the design of ceramic fillers with the idea of producing highly homogeneous piezo-active ceramic

nanoparticles through wet chemical synthesis; an extensive structural microstructural characterization was carried out on the synthesized particles to identify the best synthesis parameters. Then, particular attention was paid to the surface chemistry of the particles, using functionalizing agents to improve particle compatibility and dispersibility prior to the final composite production. Finally, the polymer ceramic composites were characterized both from a microstructural point of view and from an electric, dielectric, and piezoelectric perspective.

1.1.1 Energy Harvesting: Piezoelectric Effect and Piezo-materials

Piezoelectricity was discovered by Jacque and Pierre Curie in 1880 [27]. The piezoelectric effect correlates mechanical stress and electric field. There are two possibilities: when a piezoelectric material is subjected to mechanical stress it results in a charge displacement and consequently, in the generation of a difference of potential, this is called “direct piezoelectric effect”; on the contrary, if an external voltage (electrical potential) is applied, the piezoelectric material will respond with a mechanical strain, this is called “converse piezoelectric effect”[28]. The direct and converse piezoelectric effect working principles are schematized in Figure 1.

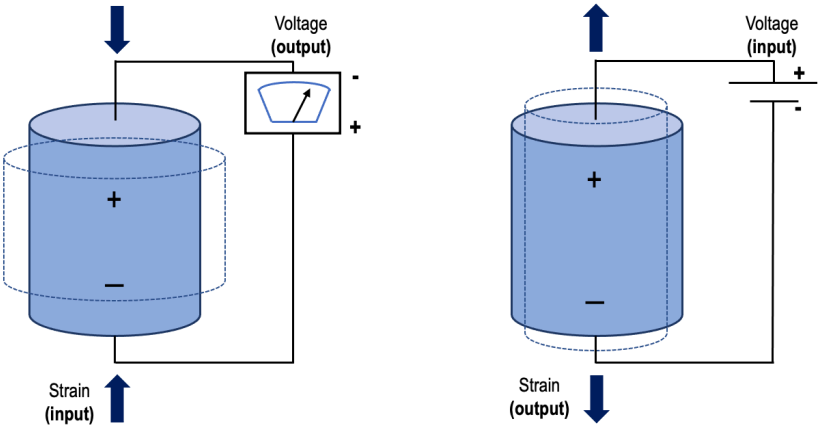

Figure 1 Schematic representation of the direct and converse piezoelectric effect for piezoelectric materials. In the direct piezoelectric effect, an input strain produces a voltage; on the contrary, in the converse piezoelectric effect, a voltage input produces a strain.

Let's focus on the direct piezoelectric effect. The direct and converse effect is fundamental for piezoelectric energy harvesting and it is ruled by constitutive equations that link stress (T) and strain (S), also known as the mechanical domain with the electric field (E) and the electric displacement (D), the electric domain [29]:

$$\begin{cases} D = d\,T + \varepsilon\,E \\ S = s\,T + d\,E \end{cases}$$

Where s is the elastic compliance, ε is the permittivity and d is the piezoelectric coefficient. D and E are vectors, and if expanded, the previous equation will become much more complex, S and T will appear as six-component vectors, s as a 6x6 matrix, and d as a 3x6 matrix. The piezoelectric charge and voltage coefficients, d_{ij} and g_{ij}, are then defined, from the previous equation:

$$d_{ij} = \left(\frac{\partial D_i}{\partial T_j}\right)^E = \left(\frac{\partial S_i}{\partial E_j}\right)^T$$
$$g_{ij} = -\left(\frac{\partial E_i}{\partial T_j}\right)^D = \left(\frac{\partial S_i}{\partial D_j}\right)^T$$

The piezoelectric charge coefficients (or piezoelectric constants d_{33}, d_{31}, etc.) are directly related to the piezoelectric effect (see paragraph 1.2.1) and they are related to the electric charge that is generated (per unit area) when a mechanical input is applied. Their unit measure is C/N (Coulomb per Newton) [30]. The subscripts refer respectively: the first to the direction of the applied field strength, and the second to the direction of the applied stress. Conversely, the piezoelectric voltage coefficient (g_{33}, g_{31}, etc.) is measured in Vm/N and is referred to the electric field produced per unit of mechanical stress applied. In this case, the subscripts refer respectively to the direction of the electric field generated in the material and, as for the piezoelectric charge coefficients, to the direction of the applied stress [30]. The electromechanical coupling factor (k_{33}) is another important parameter for dielectrics and energy harvesting because it indicates the energy conversion efficiency in piezoelectric materials; the higher the electromechanical coupling factor the higher the mechanical-to-electric energy conversion. However, this factor does not take into account dielectric or mechanical losses. In piezoelectrics, the losses can derive from different sources, hysteretic effects, dielectric losses, mechanical damping, and coupling losses. Loss factors consider all these losses.

It is easy to understand the potential behind piezoelectricity. Piezoelectric materials are largely used in everyday devices, starting from gas-igniters to mobile phones, sound amplifiers, sonars, and many others[31–33] that can be grouped into four categories: actuators, voltage generators, vibration detection, and ultrasonic applications. All these categories require high-performance materials with different characteristics according to the desired application.

Among the materials that display piezoelectric behavior, ceramics are the most common. The first material that was found to show piezoelectricity was quartz, discovered in 1880 by Jacque and Pierre Curie. Then it was the turn of barium titanate ($BaTiO_3$) and shortly after lead-zirconate-titanates (PZT) that became the most widely used due to its excellent piezoelectric properties. In the last years, researchers are focused on the production and application of other piezoceramics such as Bismuth titanates or niobates [34–36]. Only a few polymers belong to the

class of piezoelectric materials, among them polyvinylidene fluoride (PVDF) and its co-polymers [37,38], Parylene-C [39], and some natural biopolymers such as collagen and silk[40]. However, the piezoelectric performances of piezo-active polymers cannot even be compared with the ones of ceramics as will be pointed out in the following paragraphs.

1.1.2 Energy Harvesting: Dielectric Elastomers

Dielectric elastomers (DE) are a class of materials based on polymers such as natural rubber (NR), acrylic rubber, and elastomers [41,42]. These materials can be employed to implement DE generators (DEG) to harvest and convert electrical energy from mechanical deformation, and they can be used in different operative conditions: as an actuator, as a generator, or as a sensor [41,43], whatever the mode the idea is to use them as variable capacitors. Additionally, they can be used as actuators, the deformation of the capacitor is induced thanks to the application of electrostatic forces to act against mechanical stress; when used as generators the mechanical deformation will, on the contrary, lead to an increase of the electrostatic potential energy; concluding, in sensor mode the variation of the capacitance is used to sense stresses and strains.

These materials base their capacity to harvest energy on their high deformability coupled with a good dielectric constant and a high dielectric breakdown. DEGs are advantageous as power generators because [41]:

- are light, stretchable, and easily processable.
- can be adapted to several geometries and different scales, from macro to micro/nano applications.
- can exploit high energy densities.
- are usually low-cost materials.

The working principle of DEGs is based on their capacity to store electrical charges acting as a capacitor and then releasing them. The principle is schematized in Figure 2.

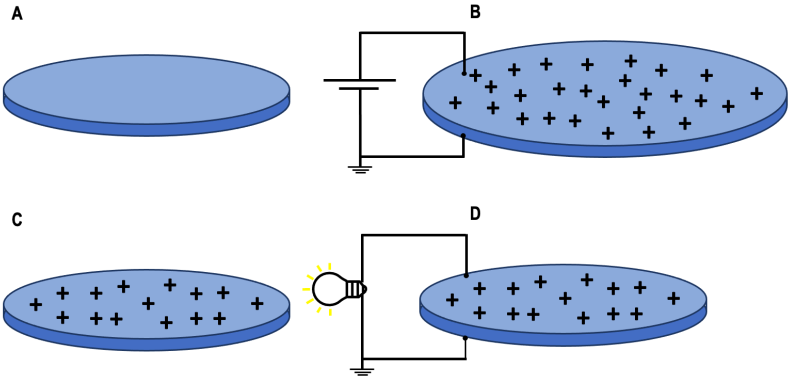

Figure 2 Scheme of the working principle of a dielectric elastomers generator in all its steps: A) unstretched stage; B) charging during stretching; C) stretch release; D) discharge.

In the beginning, the DE is in the un-deformed stage, then it is stretched, and it accumulates charges with an external source (priming), then the external source is disconnected. At this point, the stretch is released, and it returns to the initial undeformed condition. Finally, the discharge occurs when connected to an electric load. According to the DE geometry and stretching type (uniaxial, biaxial, shear, and so on.), the mechano-electrical model is different and different in the way to calculate the convertible energy density [41].

The energy that can be stored in dielectric elastomers is correlated to the following equation:

$$U_e \propto \varepsilon_0 \varepsilon E_{BD}^2$$

Where U_e is the energy density that can be stored in the material, ε_0 is the vacuum permittivity, ε_r is the dielectric permittivity of the material and E_{BD} is the dielectric breakdown of the material. The energy that will be further converted is proportional to this quantity and is also dependent on the type of deformation, being it uniaxial, shear, biaxial, etc.; however, maximizing the U_e value is crucial for the final properties. According to this equation, the key factors influencing the energy density of the material are the dielectric breakdown and the dielectric constant. The dielectric constant (ε_r), or relative permittivity, is a value that refers to the capacity of materials

to store electrical energy when immersed in an electric field. Let's consider a capacitor with a dielectric between the plates: the relative permittivity is the ratio between the capacitance of the capacitor in the presence of the dielectric and the capacitance of the capacitor in a vacuum. Accordingly, relative permittivity can be defined as:

$$\varepsilon_r(\omega) = \frac{C}{C_0}$$

This is the way to measure the dielectric constant under static electric fields. However, relative permittivity can also be seen as the ability of a material to polarize when subjected to an electric field and this polarization can come from different sources: electronic, atomic, ionic, dipolar, and interfacial. These polarization mechanisms can be activated at different frequencies; accordingly, permittivity is a frequency-dependent value as shown by the equation:

$$\varepsilon_r(\omega) = \frac{\varepsilon(\omega)}{\varepsilon_0}$$

where $\varepsilon(\omega)$ is the permittivity of the material (frequency-dependent) and ε_0 is the vacuum permittivity. Permittivity is a dimensionless value, it is a complex number, with a real and an imaginary part. To measure the dielectric constant in function of the frequency, dielectric spectroscopy is used, more insights will be provided in chapter 2.

The dielectric breakdown (E_{BD}), or dielectric strength, is a measure of the ability of materials to sustain high electric fields before the breakdown. Electric breakdown occurs in solids, liquids, and gases even if the involved mechanisms can differ. Depending on the material and its state (solid, liquid, gas), charge carriers (charged particles) can be electrons, ions, charged atoms, or molecules. The concentration and availability of these charge carriers directly affect the insulating/conductive properties of materials. For example, thanks to their big availability of electrons as charge carriers, metals have a very low electric resistivity and behave as conductors. On the contrary, materials with a low amount of charge carriers, as in the case of ceramics, glasses, and polymers (with few exceptions), will behave as insulating materials (or

dielectrics). When an insulating material is subjected to a high voltage, and consequently to a high electric field it can become conductive; this occurs if the applied voltage exceeds the dielectric strength of the material, in this situation the number of charge carriers increases abruptly several orders of magnitude, causing a drop of its resistance and flowing of electrical current. The electric breakdown event can be momentary such as in the case of an electrostatic discharge, or even continuous, as it happens in an electric arc. The dielectric strength, so the maximum operating voltage for a material before the occurrence of the breakdown is measured in V/m (more common in kV/mm or MV/m) and is an intrinsic property of the material; however, it can vary depending on the presence of defects in the material or because of some external factors such as temperature, humidity, or voltage ramp [44]. Materials that couple high values of ε_r and E_{BD} enable the improvement of U_e. That's why the challenge for DEGs today is to increase both the dielectric permittivity and the dielectric breakdown [45] to enhance the energy storage capability. As said before, DEGs are based on rubbers and elastomers which are characterized by a low dielectric constant; combining elastomers with dielectric ceramics, namely producing polymer-ceramic composites, can, for example, increase the value of the dielectric constant and boost the dielectric performance. However, the addition of ceramic filler can also cause some drawbacks such as the reduction of the breakdown strength. These issues can be handled through the control of the interfaces between the polymeric matrix and the ceramic filler to obtain better dielectric properties. Being DEG's mechanism based on sample deformation and stretching release it is also very important to evaluate the properties of the samples when they are subjected to strain. In fact, stretching is reported to have significant effects on both dielectric strength and dielectric constant in two opposite trends: by increasing the dielectric strength but at the same time decreasing the dielectric constant. An evaluation of the dielectric performance under stretching will be given in paragraph 3.6.3.

1.2 Use of Composite Materials

The most recent trends of research on piezoelectric materials and materials for energy harvesting are focused on the use of composite materials [2,3,46] to take advantage of the intrinsic properties of different classes of materials. Piezo ceramics and high-performance dielectric ceramics are characterized by high values of piezoelectric constant, high permittivity, and good

electromechanical coupling factor as summarized in Table 1. Regarding the filler, PZT was widely used since the end of the 70s but the need for non-toxic and non-harmful fillers directed scientists to the research on lead-free perovskitic oxides such as titanates, zirconates, and niobates. For example, Coondoo et al. [47] produced a Pr-modified Ba-Ca, Ti-Zr oxides modified with enhanced piezoelectric properties, and Xu et al. [34] achieved superior piezoelectric properties combining potassium-sodium niobate (KNN) with barium zirconate ($BaZrO_3$, BZ) and bismuth-sodium hafnium oxide ($Bi_xK_{1-x}HfO_3$, BKH). In this scenario, $BaTiO_3$ also re-gained attention thanks to its good properties and ease of production.

Unfortunately, the main limit of ceramics stands in their rigidity: since they cannot be bent, stretched, or easily deformed they can't be successfully used in wearable devices, soft sensors, and many other attractive applications.

Table 1 Main properties of widely used piezo ceramics.

Property [unit]		**quartz**	**$BaTiO_3$**	**PZT-A**	**PZT-B**	**LiNbO3**	**$(K,Na)NbO_3$**	**ZnO**
Density [g/cm^3]		2.7	5.7	7.9	7.7	4.7	4.5	5.6
ε_r	[-]	4.6	1900	1200	2800	85	350	9
d_{33}	[pC/N]	-	190	268	480	6	86	6-13
k_{33}	[-]	-	0.49	0.68	0.72	0.17	0.61	-

On the other hand, piezo-active polymers such as PVDF, Parylene-C, and others are soft and flexible, and they can be easily processed, shaped, and deformed accordingly to the desired application. The use of piezo polymers has enormously extended the possible application areas of piezoelectricity to all the fields that need softness and flexibility. The most largely employed polymers are piezo-active polymers such as PVDF, Parylene-C, and Polylactic acid (PLLA) but also polymers that are not considered piezo-active are widely used. Nayak et al. [48,49] for example, used polyurethane (PU) coupled with titania nanoparticles to produce nanocomposites with good dielectric and piezoelectric properties. Natural rubber (NR) was also used by Salaeh et al. [49] to produce polymer ceramic composites with high flexibility and good mechanical properties. In addition, also epoxy resin [50] and PDMS [51] are widely used thanks to their wide range of properties and ease of manufacturing. Polymers are characterized by low

dielectric and piezoelectric constants if compared with piezoceramics, as summarized in Table 2.

Table 2 Main properties of widely used piezo active polymers.

Property [unit]	PVDF	Parylene-C	Nylon 11	PDMS	collagen	silk	PLLA
Density [g/cm^3]	1.78	1.29	1.05	0.98	1.3-2.9	1.4	1.24
ε_r [-]	12	3.1	3.0	2.7	2.3	6	2.7
d_{33} [pC/N]	25	-	3	-	0.3	1.5	6-12
k_{33} [-]	0.23	0.02	-	-	-	-	-

Accordingly, the main effort of researchers in the last decade is directed toward the development of polymer-ceramic composites that can combine the excellent dielectric and piezoelectric properties of ceramics (high dielectric constant, high piezoelectric constant, good electromechanical coupling factors, etc.) with the softness and flexibility of polymers. The most common and fast way to produce composites with high piezoelectric properties was to combine polymeric matrices with PZT due to its superior dielectric and piezoelectric properties: this approach was followed since 1979 by Furukawa et al. [52] with different polymeric matrices and then, for example, by Arlt and Wegener with PVDF [38] or by Babu and de With, with PDMS [53]. More recent trends are heading researchers to use lead-free ceramics, because of the correlated environmental hazards: for example, Abinnas et al.[36] developed a nanogenerator for mechanical energy harvesting producing a nanocomposite based on PDMS with bismuth titanate under the form of nanosheets; Patnam et al. [54] mixed Ca-doped barium zirconate titanate with PDMS to fabricate piezo/triboelectric hybrid nanogenerators. Accordingly, the use of such new lead-free perovskites to be coupled with polymeric matrices abruptly increased in the last decade.

1.2.1 Production Methods

The design of composite materials allows to finely tune the final properties of the material, accordingly to the intended application, through a proper selection of filler type and matrix,

synthesis route and processing, or the possible addition of functionalizing agents and/or additives. Different production methods can be used both for the synthesis of the fillers and to manufacture the final composite. The use of different synthesis methods leads to ceramic fillers with different sizes (from macro- to nano-) and different shapes such as particles[55], flakes [56,57], wires [58,] or rods[59]. This gives the possibility to build up composites with tailored properties and directionality depending on the type of connectivity between matrix and filler. In addition to that, piezoelectric polymer-ceramic composites can be fabricated through different techniques, such as solution casting, compression molding, 3D printing, and others, to obtain final products with high homogeneity and enhanced piezoelectric properties. The simplest and most widely used process is solution casting. In solution casting the ceramic filler is blended with the polymeric matrices with or without the aid of an additional solvent, the compound is then mixed and sonicated to have a homogeneous mixture. The mixture is cast in a mold and cured to promote the crosslinking of the polymeric part and produce the final composite. Solution casting has been used with a wide range of fillers and polymers [60–63]. 3D printing is also gaining attention in the last years, for example, Tsekilos et al. [64] successfully produced PLA-KNLN (Potassium-Sodium-Lanthanum niobate) composites using a commercial 3D printer FFF (fused filament fabrication) to produce hybrid composites with aligned ceramic filler particles. The alignment of fillers is another interesting solution to enhance the material properties and to build up structured composites with preferred orientation and designed anisotropy. Filler alignment is obtained thanks to the application of an electric field (DC or AC) during the consolidation step. The application of an alternating (AC) electric field is called electrophoresis, this can be done both during 3D printing, as done by Tsekilos et al. [64], or during solution casting as reported by D'Ambrogio et al. [65] with the alignment of PZT/PDMS micro composites. However, particle alignment can be obtained even with the application of a direct electric field as demonstrated by Park and Robertson [66]; carbon nanotubes alignment once subjected to DC electric field in PDMS oil was demonstrated by Takahashi et al. [67]. The application of a DC electric field together with temperature (thermal treatment) is also responsible for the poling of the material. Briefly, poling is a phenomenon that allows orienting dipoles in the material. When a piezoelectric material is subjected to an external electric field, dipoles and piezoelectric domains will align along the direction of the applied electric field, polarizing the material. When the electric

field is removed, part of this polarization is conserved, and it is called “remnant polarization”. The presence of this net polarization is responsible for the piezoelectric properties of the material.

In this work, $BaTiO_3$ nanoparticles (NPs) were used as filler in two different matrices, namely polydimethylsiloxane and epoxy resin, and the composites were produced through solution casting. During the curing step composites were heated with the simultaneous application of a direct electric field to try to promote both poling and alignment of the ceramic filler to produce composites with enhanced piezoelectric and dielectric properties. Poling will be better discussed in paragraph 1.4.1.

1.3 Ceramic Filler: Barium Titanate ($BaTiO_3$)

Barium titanate is a perovskitic material with the general formula ABO_3 where A and B are two metallic cations, in this case respectively Ba and Ti, and O is the anion. Barium titanate was discovered in the US, in 1942, by Wainer and Salomon [68]. At that time, it represented a great improvement in the field of high capacitance-condenser due to its excellent dielectric properties (high dielectric constant, high electromechanical coupling coefficient) [69,70]. However, it was only in 1946 that the piezoelectricity of barium titanate was proved. For a couple of decades $BaTiO_3$ was largely used in the electro-ceramics industry but it was gradually abandoned after the discovery of lead-zirconium titanate-based ceramics (PZT) that have superior piezoelectric properties with respect to $BaTiO_3$. However, the interest in $BaTiO_3$ and other lead-free electro-ceramics has increased again in the last decades due to environmental problems caused by the presence of Pb in PZT-based ceramics. Nowadays, researchers are exploring methods to enhance the dielectric and piezoelectric performance of $BaTiO_3$ and make it suitable for a wide range of possible applications. To accomplish this objective, different strategies are currently explored, such as acting on the production method to obtain particles with precise characteristics in terms of microstructural features, aspect ratio, size, and homogeneity; doping with different methods to tune the electric, dielectric, and piezoelectric properties of the final product or mixing different perovskitic oxides to produce solid solutions with specific properties.

1.3.1 $BaTiO_3$ Structure and Properties

The dielectric and piezoelectric properties of barium titanate are directly correlated to its crystalline structure and the symmetry of the crystalline lattice. Depending on the temperature $BaTiO_3$ can be found in different crystalline structures. At temperatures above 120-130 °C, (i.e., above the Curie Temperature, T_c), $BaTiO_3$ has a cubic structure, in the range 5 °C < T < 120-130 °C the stable structure is tetragonal, below 5 °C it is orthorhombic (monoclinic) while at temperatures below -90 °C the stable phase is the rhombohedral one [71]. All these crystal lattices can be considered as a distortion of the cubic cell along different directions: edge, face diagonal or body diagonal respectively for tetragonal, orthorhombic, or rhombohedral [71]. As mentioned above, electric, dielectric, and piezoelectric properties are directly correlated to the lattice structure. In the cubic structure the Ba^{2+} cations are found at the corners, the O^{2-} anions are positioned in the face centers while the Ti^{4+} occupies the octahedral interstice (Figure 3). This crystalline lattice is centrosymmetric, thus there is no net polarization, resulting in a paraelectric behavior. On the contrary, $BaTiO_3$ tetragonal cell is characterized by an elongated c-axis, leading the Ti^{4+} ion to be displaced from the octahedral interstice (Figure 3), resulting in a net polarization along the c-direction. In fact, the shifting of Ti^{4+} is accompanied by a shifting of all the other cations in the adjacent lattices. The rearrangement of atoms results in the formation of a “ferroelectric domain” that has uniform polarization along a preferential direction. This results in the ferroelectric and piezoelectric behavior of the material. Due to its spontaneous polarization and stability between 5 and 120 °C the tetragonal phase is the most interesting to have piezoelectric $BaTiO_3$. In polycrystalline materials, the existence of several ferroelectric domains leads the final net polarization to be equal to zero since all the domains are randomly oriented to minimize the energy. When an external electric field is applied, the polarization of these ferroelectric domains can align through the direction of the applied electric field (poling) increasing the final net polarization. However, poling of polycrystalline materials, such as $BaTiO_3$, will not allow the full alignment of dipoles in all grains but it will promote 180° and 90° domain switches of materials (with respect to the direction of the applied electric field), with the 90° switch causing also strain within the material. When the electric field is removed some domains will go again through a 90° switch to minimize strain, but no 180° switch will occur. This results in a part of domains that remains aligned through the poling direction resulting in

the so-called “remnant polarization”. Starting from this condition, if the materials are subjected to compressive or tensile stresses, the 90° domain switch will occur changing the polarization of the material, alternatively, with the further application of an external electric field the 90° domains switch will result in stretching or squeezing along the direction of the applied electric field. These are the reasons for the piezoelectric behavior of the material. The piezoelectric effect is quantified by three coefficients, the piezoelectric charge coefficient d_{xy}, the piezoelectric voltage coefficient g_{xy}, and the electromechanical coupling factor k_{xy}. These coefficients have already been discussed in paragraph 1.1.1.

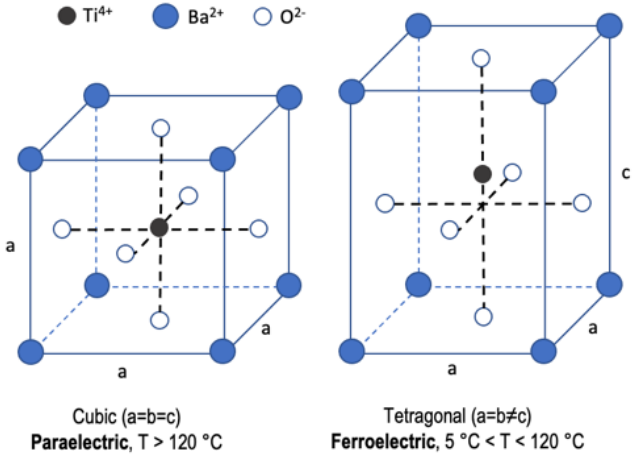

Figure 3 Cubic and tetragonal lattices of $BaTiO_3$. It is evident the displacive transformation along the c-axis in the tetragonal lattice with the Ti^{4+} cation that is displaced from the midplane.

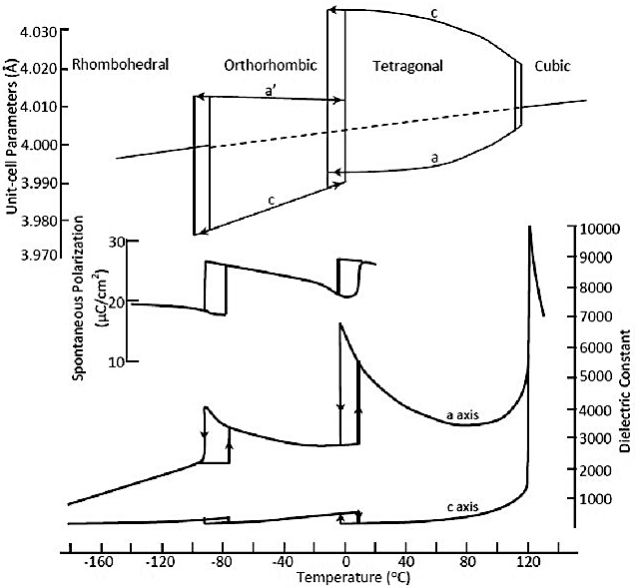

Figure 4 Dielectric constant, spontaneous polarization, and unit cell parameters trends of $BaTiO_3$ in dependence on the temperature and on its phase transformation [69,70] *(image available under license CC BY 3.0, https://creativecommons.org/licenses/by/3.0/)*

Dielectric and piezoelectric properties depend on the crystalline structures and crystalline structures depend on the temperature. Figure 4 shows the trend of dielectric constant, spontaneous polarization (P_s), and the unit cell parameters in function of the temperature. The dielectric constant is higher when $BaTiO_3$ is found in the tetragonal phase and the mean value decreases passing to the orthorhombic and then to the rhombohedral phase, this is also valid for the spontaneous polarization[69,70]. Furthermore, a tetragonal lattice with a high c/a ratio, namely a high value of tetragonality t, is responsible for higher Ti^{4+} displacement, higher spontaneous polarization, and higher final piezoelectric properties (d_{33}, d_{31}, g_{33}, g_{31}) [72]. These properties can be tuned by acting on the microstructural features of the final product: lattice parameters, crystallite size, and grain size strongly influence the dielectric and piezoelectric properties of the material[73]. $BaTiO_3$ particles' grain size, crystal size, and size distribution can be modified either using suitable production methods or by doping with rare earth or other

metallic cations. The following paragraph will explore these two approaches, considering both advantages and drawbacks.

1.3.2 Production Methods

$BaTiO_3$ can be produced through different approaches such as mixed solid-state route, sol-gel process, hydrothermal synthesis, or via the Pechini method. The most simple, common, and easy process is the traditional solid-state synthesis. In solid-state synthesis barium oxides (e.g., BaO, $BaCO_3$) and titanium oxides (e.g., TiO_2) are mixed in a 1:1 Ba/Ti molar ratio, ball milled, and put into a furnace at very high temperatures (1100-1500 °C) [74]. At the end of this step, $BaTiO_3$ is formed with CO_2 as a by-product. The main advantages behind the solid-state synthesis of barium titanate lie in the ease of the process and the high crystallinity of the final product. Unfortunately, $BaTiO_3$ powders produced via solid state route are usually not homogenous in terms of aspect ratio, they present a wide size distribution and the presence of impurities in the final sample strongly depends on the level of impurities of the starting Ba- and Ti-oxides; furthermore, some porosity is inevitably present [75,76]. In addition to that, the process is highly energy-demanding due to the high temperatures required.

Wet chemical methods comprehend all the production processes that start from liquid and colloidal precursors, and they offer the possibility to synthesize highly homogenous, high purity, fine powders even at low temperatures if compared with the classic solid-state route [75,76].

In the sol-gel production process, $BaTiO_3$ is usually synthesized by mixing two sols prepared with Ba and Ti precursors respectively. Hydrolysis-condensation reactions of the metal precursors are run at low temperatures (50 - 200 °C) for several hours times until a gel is formed. The gel is then dried and crushed into powders that are subjected to a final calcination step. This process results in ultrafine and highly pure and highly homogenous $BaTiO_3$ powders. In sol-gel synthesis, the characteristics of the final products depend on many parameters such as time, temperature, sol composition, and the type of precursors. Among these parameters, precursors play a key role because they condition the microstructural features of the final product and, consequently the electric and dielectric properties. In the sol-gel method, the most widely used Ba precursors are barium acetate ($Ba(CH_3COO)_2$)[77–80], barium hydroxide ($Ba(OH)_2$)[81], barium chloride ($BaCl_2$) [55,82] and barium alkoxides while employed Ti-precursors

are titanium dioxide (TiO_2)[83], titanium isopropoxide ($Ti(O^iPr)_4$)[78–81,84], titanium hydroxides ($Ti(OH)_4$)[81] and titanium chlorides ($TiCl_4$)[55,81].

Hydrothermal/solvothermal processes are also based on hydrolysis-condensation reactions which are carried out in a steel-lined Teflon® autoclave, heated up to relatively high temperatures (120 - 300 °C) and subjected to autogenous pressure [75,77,85] with the advantage of strongly reducing the synthesis reaction time.

The Pechini method [86,87] is a production process applied to the preparation of $BaTiO_3$ and other perovskite oxides. It is a wet chemical synthesis method that starts with the production of two metal-citrate solutions that are then mixed to have a Ba-Ti citrate solution. This solution is heated under stirring and transforms into a polymeric resin, which is dried leading to powders that are subjected to a final annealing step.

1.3.3 Doping

The main advantage of the perovskitic structure of $BaTiO_3$ resides in its capability to accommodate in A and B sites a large variety of metallic cations. Literature reports several articles on the doping of $BaTiO_3$ and other perovskitic oxides. In fact, a wide range of dopants has been used, from rare earth [88,89] to metals[90,91], to semi-metallic elements [92], and alkaline elements [93–95]. Doping mechanisms can strongly affect the microstructural, optical, and electrical properties of $BaTiO_3$ ceramics. Depending on the relative ionic radius and the formal charge of the dopant element, the ion substitution can occur in the A or B site even if in some cases also mixed-modes have been proposed [96,97]. For example, alkaline elements will preferably occupy Ba-site, V, Nb, Mo, Ni, and Co are substituents for Ti while elements Ca, Sr, Y, Hg, and Tl can occupy both A and B sites [96]. According to the substitution site and the nature of the dopant, the introduction of different metallic cations generates and activates different mechanisms of charge compensation, vacancies formation/suppression, and defects; moreover, also the crystalline lattice can be distorted, introducing lattice strains. Thus, depending on the nature of the dopant and the site of the substitution it is possible to tune the material's structure acting on the cell parameters, cell size, tetragonality, phase transitions, and phase stability, which will impact electrical properties, optical properties, and the Curie temperature [98–102].

1.4 Polymeric Matrices

When dealing with polymer-ceramic composites, the appropriate choice of the polymeric matrix is essential to obtain a final product with suitable properties for the intended application. For example, to build up a device that must be flexible at room temperature it is preferable to use polymers with a low glass transition temperature (T_g) and if the devices must be subjected to a large strain, the choice falls on elastomers. For instance, ultra-stretchable elastomeric electrets for charge generation have been prepared by Ko et al. [103] by mixing PMMA-based particles with PDMS. These composites can operate with a stretch of up to 600% making them suitable for energy-harvesting applications from mechanical stretching. More recently (2022), Jiang et al. [104] used PMVS (poly dimethyl (methylvynil)siloxane) as a matrix for DEG composites with high efficiency and long fatigue life. On the contrary, to develop a sensor that works on detecting vibration, it is preferable to avoid elastomers since they would dampen the incoming input and use stiffer polymers. For example, James et al. [105] developed a PZT-epoxy-based sensor with an appreciable piezoelectric response that can founds application in sensors and transducers, or again, Kim and Kim [106] in 2018 prepared a high-performance, flexible, piezoelectric pressure sensor by embedding CNTs doped ceramics into an epoxydic matrix. Accordingly, with the idea to explore different possible applications, the present work put focus on the use of two different matrices, an epoxy resin with a low T_g and a silicone-based elastomer, PDMS.

1.4.1 Epoxy Resin: Properties and Applications

Epoxy resins are thermosetting polymers that belong to a class of polymers characterized by the presence of an epoxide (also known as oxirane) group in their structure [107]. Due to their wide range of thermal and mechanical properties, epoxy resins are employed in many application areas as paints and coatings, electronics and printed circuit boards, high voltage applications, structural adhesives, and fiber-reinforced composites for structural applications (e.g., automotive) [108]. The condensation reaction of epoxides was patented in 1934 by Paul Schlack while the most common and used bisphenol-A-based epoxy resins were discovered by Pierre Castan in 1943 [109]. Bisphenol-A-based resins are derived from the reaction of epichlorohydrin with bisphenol-A, resulting in a compound named bisphenol A diglycidyl ether

(DGEBA) as shown in Figure 5. DGEBA is the building block of all bisphenol-A-based resins, and it is subjected to a cross-linking reaction to obtain the final product.

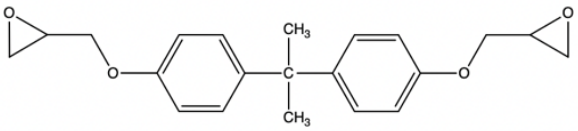

Figure 5 Diglycidyl ether bisphenol-A (DGEBA) block.

The curing reaction of these resins is obtained with the aid of a curing agent that can be amines, anhydrides, imidazole, and others [110,111]. Depending on the nature of the resin and of the curing agent (hardener) the curing step can be carried out through the application of heat or, in the case of UV-sensitive (Ultraviolet) hardeners with the application of UV light. Anyway, independently from the hardener type and curing reaction (thermally/photo activated), the cross-linking reaction occurs because of the oxirane ring opening that leads to bonding the crosslinker; the crosslinker usually has multiple active sites to exploit the ring-opening reaction for several building blocks and this will result in a rigid polymer network as shown in Figure 6.

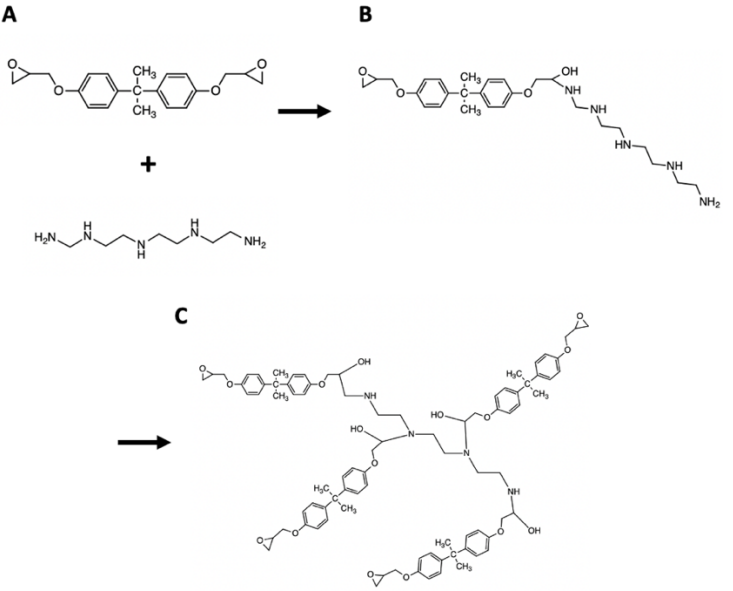

Figure 6 Example of the evolution of the curing reaction of a standard DGEBA epoxy resin with an amine-based hardener, in this case, triethylenetetramine (Teta). A) DGEBA and Teta, starting building blocks; B) Epoxy ring opening and Teta bonding; C) formation of the polymer network

Epoxies can exploit an extremely wide range of chemical, thermal, and mechanical properties. In general, epoxy resins have high thermal resistance and high resistance to chemicals, especially to alkaline solutions [112]. However, the mechanical and thermal properties of epoxy resins are strongly correlated to the type of resin, the nature of the hardener, and the curing cycle. For example, their glass transition range can vary from 10 °C (relatively soft at room temperature) up to 250 °C and their elastic modulus is in the range of 2 - 4 GPa [113,114]. Concerning the electric and dielectric properties, epoxies, like many other polymers, have low dielectric constant, high dielectric strength, and low electric conductivity. As shown before, the combination of all these properties makes epoxy resins very attractive in piezoelectric composites application, especially in sensors.

1.4.2 Polydimethylsiloxane: Properties and Applications

Polydimethylsiloxane (PDMS) is a polymer largely employed in many research fields thanks to its low cost and properties. PDMS belongs to the class of silicones elastomers, it is a siloxane compound formed by a (Si-O) backbone where the silicon is also linked to two methyl (-CH_3) groups [51] Figure 7. The presence of siloxane bonds confers high chemical and thermal stability to the polymer while the methyl groups are responsible for the high hydrophobicity of PDMS.

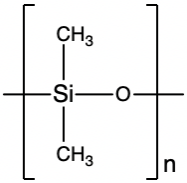

Figure 7 Polydimethylsiloxane (PDMS) repetitive unit structure. The backbone is constituted by Si-O bonds and two methyl groups are linked to the Si atom.

PDMS is usually synthesized by hydrolysis and condensation reaction of dichlorosilanes to produce cyclic and linear polymers. However, to have higher control over the molecular weight of the final product, the industry of polymers moved through ring-opening polymerization using cyclic siloxanes as precursors. Having a high control on the molecular weight of the polymer allows to finely tune several material properties such as viscosity, viscoelasticity, and others. All these properties can also be tuned by acting on the crosslinking reaction. Changing the ratio between polymer and curing agent or using different groups (such as phenyl- or vinyl-) will result in a large property change. For example, there could be an increase/decrease of the mechanical properties (elastic modulus, tensile strength, hardness, etc.) as well as a modification of electric and dielectric characteristics. The cross-linking of siloxanes is usually obtained thanks to the use of Pt-based catalysts as shown in Figure 8.

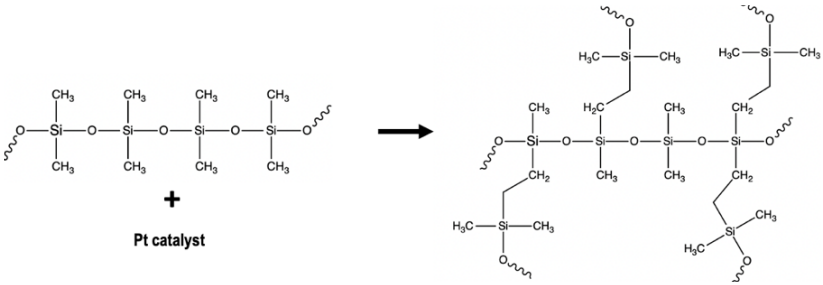

Figure 8 Typical crosslinking reaction of polydimethylsiloxane using Pt-based catalyst.

Polysiloxanes are available in a wide range of compositions, leading to a wide range of chemical and mechanical properties. For what concerns the mechanical properties PDMS usually has low elastic modulus and low tensile strength, nevertheless, it can be subjected to very large strains [115]. Chemically speaking, PDMS is very interesting because it has a high resistance to chemicals, it is chemically inert and non-toxic, it is transparent, and it is thermally stable in a wide range of temperatures and has a glass transition temperature of around -125 °C. Finally, for what concerns the electrical properties, PDMS is a good dielectric, a very good insulator, and presents high electric breakdown voltages [116]. PDMS properties can be enhanced or tuned with the addition of fillers or thanks to the blending with other polymers, making PDMS one of the best choices for a wide range of applications. In fact, PDMS was successfully used coupled with MWCNT and PVDF nanofibers by Wang et al. [117] for wearable devices, furthermore, it was also used coupled with different oxides particles as a tactile sensor for microelectronics, as reported for example by Sappati and Bhadra [118] or by Gao et al. [119]. In addition to that, PDMS reacted with appropriate chemical modifiers and also found an extensive application in microfluidics for biomedical applications, such as cell culture, protein capture/release, and biomolecule separation as shown by Zhou et al. [120].

1.5 Particle Functionalization

The great advantage of composite materials stands in the possibility of combining the properties of both matrix and filler to achieve a final product with superior characteristics. Anyway,

composite materials, in particular polymer-ceramic composites, also present some problems. The main issue of polymer-ceramic composites resides in poor matrix-filler compatibility [121]. The low chemical affinity between the organic matrix and the inorganic ceramic filler can result in reduced final properties of the material. Let's focus on polymer-ceramic composite using a ceramic filler in the form of micro/nanoparticles. If the compatibility between the matrix and the filler is scarce it can, for example, result in a reduced particles' dispersibility and in the tendency to form aggregates; these aggregates can strongly affect the final sample homogeneity and even act as defect sites lowering, for example, the mechanical strength. Extensive studies have been carried out to evaluate the tendency of particulate fillers to form aggregates. Moczo et al.[122] studied the aggregation of $CaCO_3$ filler in polypropylene (PP) finding out that the degree of aggregation increases by decreasing the particle size and of course, by increasing the filler amount. The increase in filler concentration can result in a non-homogeneous filler dispersion into the polymeric matrices. This could be due to the viscosity of the polymer-ceramic paste; in fact, Khastgir and Adachi [123] showed that $BaTiO_3$/PDMS suspensions with more than 10 %vol of barium titanate in the slurry exhibit non-linear viscoelastic behavior, showing thixotropic behavior and plasticity. This will result in an un-proper particle mixing and dispersion and the formation of clusters and aggregates. These effects can be even enhanced when moving from micro- to nanoparticles. In fact, NPs usually present high specific surface area (SSA) making them more reactive and more prone to forming aggregates. SSA, together with particle size is a key parameter as shown by Kiss et al. [124] in a further study on $CaCO_3$ particle aggregation in PP: particles with higher surface area were creating more aggregates, resulting in poorly homogeneous composites. In this scenario, it is easy to understand that the chemistry of interfaces plays a key role in composite materials. Acting somehow at the interface between the filler and matrix can represent a solution to tune and increase the matrix-filler compatibility, improve the homogeneity of the final product, and enhance the final properties of the material.
Particle functionalization is probably the best solution to decrease the surface energy of nanoparticles and achieve this objective. In the previous work, Kiss et al. [124] also observed a decreased tendency to aggregation when the particles were surface coated with surfactants, dramatically changing their behavior. Also, Dormlzasky et al. [125] claim achieving a reduction of

33% in the agglomeration tendency of $BaTiO_3$ particles in epoxy resin through surface functionalization of the particles with phosphonic acid.

More recently, chemically modified nanofillers have been synthesized also to be used in dielectric and electronic applications [126]. Different surface modifying agents, such as surfactants, silane coupling agents, metallic nanoparticles, and others, have been used in literature to obtain an enhancement of piezoelectric and dielectric performance. These results were possible thanks both to the improved quality of the composites in terms of particle dispersibility and final homogeneity and also to the intrinsic properties of the functionalizing agents. For instance, Mensah et al. [127] produced acrylonitrile butadiene rubber (NBR) nanocomposites for piezoresistive and piezoelectric applications using gold functionalized graphene oxide (GO) as reinforcement for the matrix; they obtained an enhancement of the dielectric constant together with a reduction of the loss tangent. Again, Yang et al. [128] used polydopamine (PD) combined with a KH570 silane coupling agent to functionalize $BaTiO_3$ particles; they found out that PDMS-based composites, loaded with such functionalized particles were showing an improvement of both mechanical and dielectric properties, with an increase up to 30% of the dielectric constant depending on the functionalized filler content in the final composite. When dealing with metal oxide particles, silane coupling agents are the most applied functionalizing molecules. For example, Sun et al. [129] modified magnesium titanate (MT) nanoparticles with different silane coupling agents, namely Si-69, KH-570, and stearic acid (SA) obtaining a modified surface and changing the particle behavior from hydrophilic to hydrophobic. KH-570 was also used by Yang et al. [130], the silane was grafted onto the $BaTiO_3$ particles' surface previously treated with a polyamine, and particles were embedded into NBR: the silane's active role in the NBR vulcanization process resulted in molecular interfacial interactions responsible for an improved particle dispersion.

Figure 9 schematizes the behavior of bare and functionalized particles in a polymer-ceramic composite.

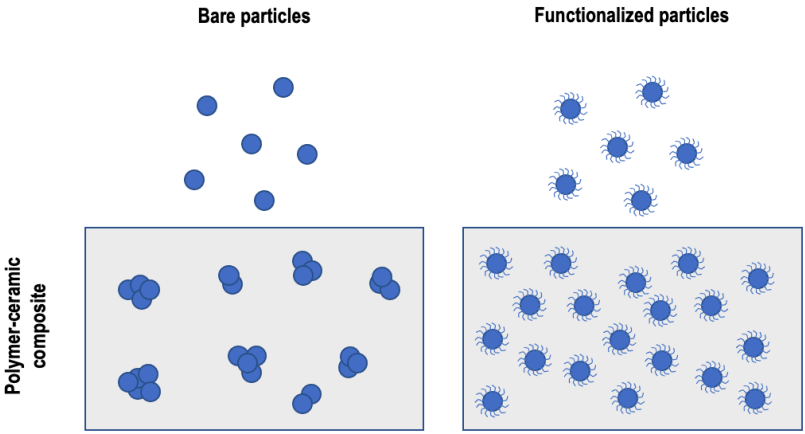

Figure 9 Schematization of working principle of particle functionalization in polymer-ceramic composites. The presence of highly compatibilizing agents results in improved and more homogeneous particle dispersibility.

Grafting of a functionalizing agent on the surface of the particles enhances the chemical affinity with the matrix and different approaches can be used: the first is to bind monomers on the particle surface and then to promote the polymerization (grafting-from approach); the second is to directly attach the functionalizing agent with the desired functional groups on the surface (grafting-to approach) [126,131–133]. However, independently of the grafting method the presence of a proper functionalizing agent on the particles' surface will promote a higher dispersibility into the polymeric matrix, resulting in fewer clusters/aggregates and consequently, in higher final properties [134,135].

1.5.1 Particle Functionalization: Problems and Solution

Particles' functionalization can be sometimes problematic, it could be difficult to efficiently graft functionalizing agents on the surface of the particles. This is mainly because ceramic, crystalline metal oxide nanoparticles, such as $BaTiO_3$ nanoparticles, are poorly reactive. The surface of metal oxide particles generally lacks active grafting sites leading to a low yield of functionalization. An inadequate surface functionalization will not be sufficient to avoid

clusters/aggregates formation. The solution is to increase the number of grafting sites on the particle surface, and this can be done through a hydroxylation process with hydrogen peroxide (H_2O_2) as shown in Figure 10. Li et al. [136] performed a hydroxylation treatment of $BaTiO_3$ particles with H_2O_2 and through XPS (X-Ray Photoelectron Spectroscopy) analysis, they observed an increase in the surface OH fraction from 9.2% of bare particles to 25.0% of H_2O_2 treated particles. Zhu et al. [137] performed a hydrogen peroxide treatment prior to the functionalization with γ-aminoproyltriethoxysilane (APTES) to produce core-shell $BaTiO_3$ nanoparticles; the presence of OH surface groups allowed an easy grafting of the silane coupling agent on the particle surface.

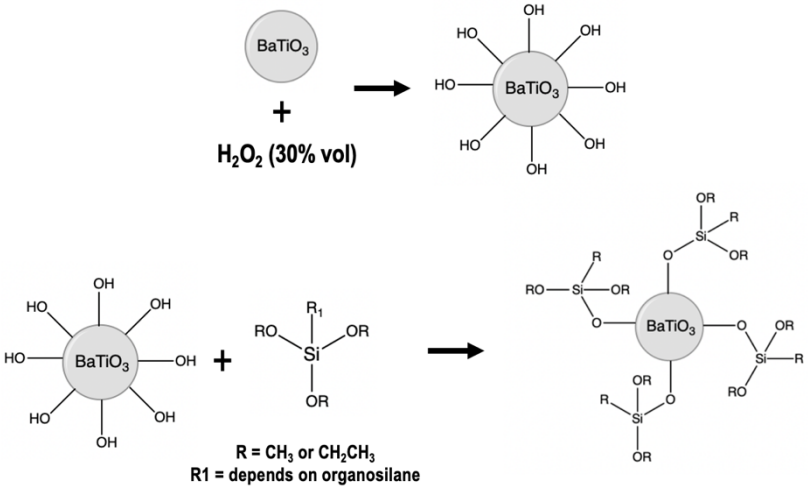

Figure 10 Schematization of hydroxylation process. Treating $BaTiO_3$ NPs with H_2O_2 will create several hydroxyl groups on the particle surface that will act as active grafting sites for the functionalizing agent.

Organosilanes with terminal methoxy or ethoxy groups condense with the hydroxyl groups on the particles' surface creating Si-O covalent bonds with the particle. Fan et al. [133] studied the molecular structure and the reaction path of (3-aminopropyl)trialkoxysilane with hydroxylated $BaTiO_3$ nanoparticles in different solvents, namely toluene, and ethanol, and proposed the

formation of both monolayer and multilayer by organosilane polycondensation (Figure 11). Liu et al. [138] demonstrated that the particle coverage is ruled by the reaction's kinetics which is governed by the reaction conditions (temperature, solvent, etc.).

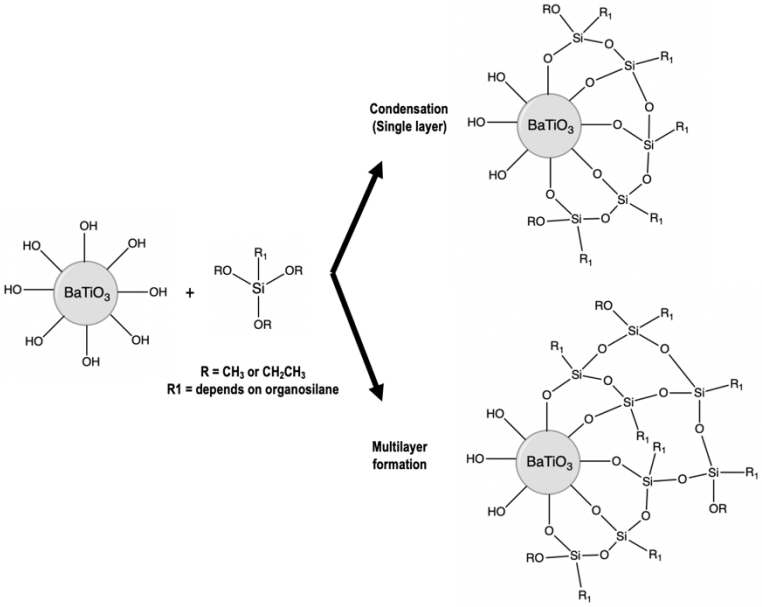

Figure 11 Possible grafting mechanisms of methoxy-organosilane: hydrolysis of methoxy groups with polycondensation of organosilanes on the hydroxylated surface of particles.

When functionalized particles are embedded in polymeric matrices, (for dielectric applications typically, PVDF, PDMS, or Epoxy resin) the silane coupling agent can increase the affinity between the inorganic filler and the organic matrix acting as a medium. In addition to that, the possible presence of functional groups on the silane coupling agents can add functionalities and/or tune the properties of the final product.

1.5.2 Organosilanes

Organosilanes are widely used in materials engineering due to their high reactivity and wide range of properties [139]. According to their chemical structure, organosilanes can also add functionality to the final product. Literature reports hundreds of organosilanes that are used for different purposes, mainly as coupling agents, coatings, crosslinkers, and adhesive agents.[139] For example, Bandl et al. [140] used different organosilanes (namely 1,8-bis(triethoxysilyl)octanosilane, BOS, and 1H,1H,2H,2H-perfluorooctyltriethoxysilane, PFOS), as coatings for molds in the production processes of polymers, resulting in a strong decrease of adhesion forces (up to 50%) and, consequently, in a facilitated demolding procedure. Liang et al. [141] deposited Bis[3-(triethoxysilyl)propyl]tetrasulfide (BTESPT) on graphene oxide sheets that were used for coating metallic surfaces, showing a high hydrophobicity and improved corrosion resistance. Kansara et al. [142] successfully crosslinked hydroxyl-terminated PDMS using different chlorosilanes, such as Trichloro(methyl)silane, trichloro(octylsilane), n-trichloro(octadecyl)silane, and a perfluorinated chlorosilane to obtain PDMS membranes; depending on the used crosslinking agent, the final membranes showed different morphologies, crosslinking degrees, hydrophilicity/hydrophobicity, and separation performances. Similarly, Xia et al. [143] performed an in-situ crosslinking of PVA/organosilica hybrid membranes using different alkoxysilanes, such as APTES, PTES (Phenyltriethoxysilane), and DEDPS (Diethoxydiphenylsilane); the crosslinkers were responsible for different thermal stabilities and separation factors of the hybrid membranes. Alkoxysilane have also been used since the 80s as adhesives agents, in 1981, Boerio and Williams [144] analyzed the structure and the properties of organosilane primer for adhesive bonding; metal joints surface were prepared by treating them with APTES and they observed that APTES-treated joints had higher load at failure and the strength was maintained for longer times, being less susceptible to aging. Similarly, Wang and Feldman [145] studied the effects of organosilanes on the adhesive properties of epoxy-lignin polyblends and they observed a considerable increase in the shear strength (up to 177 %) by coupling A-187 silane (GPTMS) to the epoxy-lignin adhesive.

These examples point out the potential of organosilanes in applications in which the chemistry of interfaces plays a key role in defining the properties of the final product. The use of organotrialkoxysilanes is continuously gaining interest as functionalizing agent for polymer-

ceramic composites for piezoelectric dielectric applications, proving their beneficial effects on the dielectric properties. The choice of the proper functionalizing agent must be done considering several factors such as molecule reactivity, filler type, matrix type, and functional end-group.

In this work, three different organo-alkoxysilanes have been used due to their structure and properties and they will be presented more in detail in the following lines.

3-glycidyloxypropyltrimethoxysilane (GPTMS) is one of the most widely used organosilanes, and its structure is shown in Figure 12. The functionalization reaction with GPTMS is usually carried out in an organic solvent (e.g., hexane, toluene) in a one-step reaction as reported for example by Othman and Apblett [146] with mesoporous silica nanoparticles or by Ma et al. [147] using activated carbon nanotubes as grafting sites. The silane directly condensates on the hydroxyl-rich surface of the substrate with the elimination of methanol as reported in Figure 12.

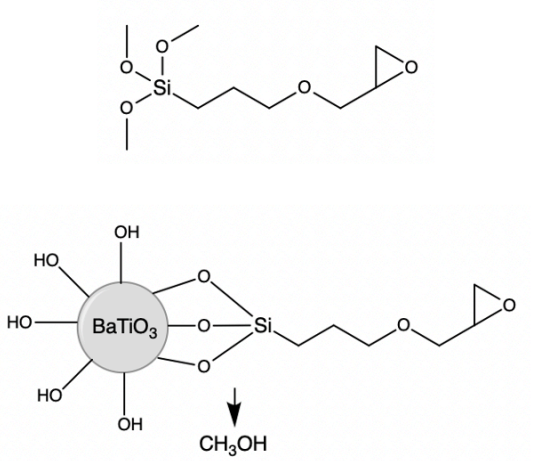

Figure 12 Schematic structure of 3-glycidyloxypropyltrimethoxisilane (GPTMS) and reaction pathway of its functionalization reaction onto hydroxyl-rich $BaTiO_3$ particles

GPTMS is an organosilane characterized by the presence of a glycidyloxypropyl chain which presents an epoxy ring as an end group. The polar oxirane ring is hydrophilic and generally presents high affinity with polymeric matrices due to both reactivity and weak interactions. In particular, during the epoxy resin curing reaction GPTMS can go through a ring-opening reaction and participate in the crosslinking of the epoxy resin, thus creating a strong interface between the oxide particle and the polymer matrix. Covalent bonding between the epoxy matrix and GPTMS functionalized GO was for example reported by Wan et al. [148] resulting in increased mechanical properties such as tensile and flexural strength as well as fracture toughness.

In this work, two organo-trialkoxysilane containing polyethyleneoxy groups were also investigated, namely 2-[acetoxy-(polyethyleneoxy)propyl]triethoxysilane (APEOPTES) and triethoxysilylpropoxy(polyethyleneoxy)dodecanoate (TESPEOD) to evaluate the presence of different functional groups on the final properties of nanocomposites. The structure of these organosilanes is shown in Figure 13.

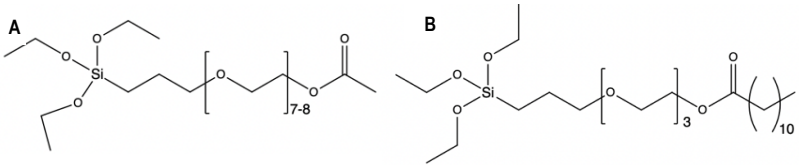

Figure 13 Schematic representation of the molecular structure of: A) 2-[acetoxy-(polyethyleneoxy)propyl]triethoxysilane (APEOTES); B) triethoxysilylpropoxy(polyethyleneoxy)dodecanoate (TESPEOD)

Both organosilanes are characterized by a propylic chain linked to a different number of polyethylene oxide (PEO) units. Moreover, chain ends are characterized respectively by a polar carboxylate group in the case of APEOTES and an apolar dodecanoate chain for TESPEOD. PEO is a polar polymer, that in its amorphous state presents a conductivity that is higher than 10^{-4} S/cm, almost ten orders of magnitude higher with respect to PDMS and epoxy resins [149]. PEO-silanes are relatively new products among tri-alkoxysilanes, and they have been used in the last years in particular in the biomedical field. In literature there are few reports on the use

of such silanes as functionalizing agents for silicones used in implantable medical devices: Rufin et al. [150] observed an improved protein resistance in bulk silicones modified with such silanes in dependence on the length of the PEO-segment, and a similar effect was noted by Hawkins et al. [151] and by Ngo et al. [152] who were able, thanks to reduced protein adsorption on the silicone surface, to improve the thromboresistance of their silicone devices. Concerning the specific selected PEO-silanes, APEOTES was reported in the literature to be used coupled with TEOS (tetraethylorthosilicate) to realize super hydrophilic coatings for photovoltaic applications, as done by Yan et al. [153] while the only reports in the literature about TESPEOD are in the field of integrative and comparative biology [154]. Accordingly, despite the interesting conductive and electrical properties of PEO, the potential of such PEO-silanes as functionalizing agents in composites with dielectric and piezoelectric behavior hasn't still been explored. The idea behind the use of such organosilanes is related to the presence of polar groups (inside or at the end of the chain) and PEO units that should be more sensitive to the electric field. The possibility of particles aligning through the direction of the applied electric field could give rise to some anisotropy in the material; furthermore, the possible polarization of these groups could also lead to an increase in the dielectric properties of the final nanocomposite.

1.6 Aims of the Thesis

Following the previous paragraphs, this thesis aims to explore the potential of new polymer-ceramic nanocomposites for application in energy harvesting. In particular, it focuses on understanding the role of ceramic fillers' functionalization with organosilanes in enhancing the dielectric and piezoelectric properties. Referring to the previously highlighted challenges, the goals of this work are:

- the optimization of $BaTiO_3$ synthesis through a simple and fast hydrothermal process, in order to obtain nanoparticles with controlled morphology, size, and microstructural properties.
- the surface functionalization of nanoparticles with different organosilanes, with the aim of achieving a high degree of grafting, and possibly tuning the particle-matrix interface in polymer-ceramic nanocomposites.

- the production of flexible nanocomposites by incorporating bare and functionalized nanoparticles in different polymeric matrices by evaluating the effect of functionalization on both the particle dispersibility and the microstructure of composites.
- finally, the electrical and dielectric characterization of the obtained nanocomposites to investigate the effectiveness of functionalization in improving the electrical and dielectric properties of these materials for energy harvesting applications..

Materials and Methods

2.1 Materials

Synthesis of $BaTiO_3$ nanoparticles: titanium (IV) isopropoxide $Ti(O^iPr)_4$ (Sigma-Aldrich, Saint Louis, MO, USA, CAS 546-68-9), barium acetate $Ba(CH_3COO)_2$ (Analyticals Carlo Erba, Milan, Italy, CAS 543-80-6), potassium hydroxide KOH (VWR International, Milan, Italy, CAS 1310-58-3), glacial acetic acid CH_3COOH (ITW Reagents, Darmstadt, Germany, CAS 64-19-7) and absolute ethanol C_2H_5OH (Merck KGaA, Darmstadt, Germany, CAS 64-17-5). Commercial BT powders, with an approximate diameter of 500 nm were also purchased from Acros Organics (Geel, Belgium, CAS 12047-27-7).

$BaTiO_3$ hydroxylation and functionalization: 30 %vol aqueous solution of hydrogen peroxide H_2O_2 (Merck, KGaA, Darmstadt, Germany, CAS 7722-84-1) and deionized water DI H_2O, 3-glycidyloxypropyltrimethoxysilane (GPTMS) (Merck KGaA, Darmstadt, Germany, CAS 2530-83-8), 2-[acetoxy(polyethyleneoxy)propyl]triethoxysilane (APEOTES) (Gelest, Morrisville, PA, USA), triethoxysilyl-propoxy(polyethyleneoxy)dodecanoate (TESPEOD) (Gelest, Morrisville, PA, USA, CAS 1041420-54-5), toluene C_7H_8 (Honeywell, Charlotte, NC, USA, CAS 108-88-3), n-hexane C_6H_{14} (Merck KGaA, Darmstadt, Germany, CAS 110-54-3) and triethylamine Et_3N (TEA) (Merck, KGaA, Darmstadt, Germany, CAS 121-44-8).

Nanocomposite production: two-component epoxy system Elan-Tron EC 251 / W 242 (Elantas Europe srl, Collecchio (PR), Italy) and a two-component silicone rubber Wacker Silgel 612 A/B (Wacker Chemie AG, Munich, Germany) were purchased; solvents: acetone $(CH_3)_2CO$ (Merck KGaA, Darmstadt, Germany, CAS 67-64-1) and pentane C5H12 (Merck KGaA, Darmstadt, Germany, CAS 109-66-0). Kapton tape (Dupont, Wilmington, DE, USA), conductive copper tape, and conductive aluminum tape were used for the poling and production process of the composites.

2.2 Synthesis of $BaTiO_3$ Nanoparticles

2.2.1 Sol-Gel Synthesis at Ambient Pressure

The synthesis was performed by modifying the protocol of Hwang et al. [79,80] as reported in Zamperlin et al.[155]. The reaction steps are schematized in Figure 14. Briefly, 0.01 moles of $Ti(O^iPr)_4$ were mixed with CH_3COOH and C_2H_5OH in a 1 : 4 : 8 molar ratio and stirred for 1h. In the meantime, 0.11 moles of $Ba(CH_3COO)_2$ (Ba/Ti = 1.1) were dissolved in 5 ml of DI water together with 0.022 mol of CH_3COOH (mol ratio Ba/Acetic acid = 1/2). The Ba-sol was then slowly added to the Ti-sol and the mixture was stirred at RT for 1h. Then, a KOH solution (3N) was added to the mixed Ti-Ba sol until reaching pH > 13 to promote the formation of $BaTiO_3$ particles, and a milky suspension was obtained which was stirred for 7 h at 45 °C in an inert atmosphere (N_2 flux). Powders were separated through centrifugation (Heraeus Instrument Labofuge 400R), washed with DI water until neutral pH, and dried at 80°C under reduced pressure. Dried powders were annealed at 900 °C (heating rate 10 °C/min) with an isothermal step of 4 h in a SiO_2 tubular oven (Heraeus GmbH, Hanau, Germany) under air flux. Powders were labeled as “BT”.

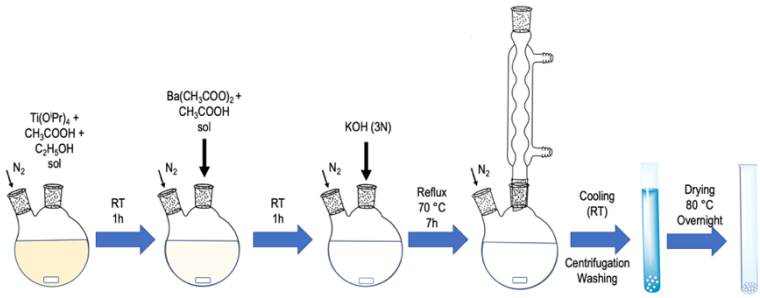

Figure 14 Main steps of the sol-gel synthesis of BT nanoparticles. Ba and Ti sol are prepared, mixed, and homogenized for 1 h. KOH solution is added and a white milky solution is obtained. The suspension is kept under stirring at 70 °C for 7h in N_2 flux. Powders are collected through centrifugation, washed, and dried overnight.

2.2.2 Sol-Gel Synthesis in Hydrothermal Conditions

Steps and conditions were identical to those reported above until the addition of KOH solution and the achievement of a milky suspension. The suspension was immediately transferred to a stainless-steel lined PTFE autoclave. The autoclave was sealed and maintained at 200 °C for different times, then it was cooled down to room temperature (RT), and powders were collected by centrifugation (Heraeus Instrument Labofuge 400R). Powders were washed with DI water until the neutral pH and dried overnight at 80°C. The dried powders were annealed at 900 °C for 4h in a SiO_2 tubular oven in air. The hydrothermal treatment was carried out for 2, 4, 6, and 8h, and obtained samples were respectively labeled BTH (for 2h treatment), BTH_4h, BTH_6h, and BTH_8h.

2.3 Particles' Hydroxylation

Preliminary studies to define the hydroxylation conditions were carried out with commercial $BaTiO_3$ particles (BTC). Different reaction times were used to identify the condition allowing the introduction of the highest amount of hydroxyl groups onto the $BaTiO_3$ NPs' surface to achieve the highest yield of organosilane grafting. The hydroxylation procedure is schematized in Figure 15.

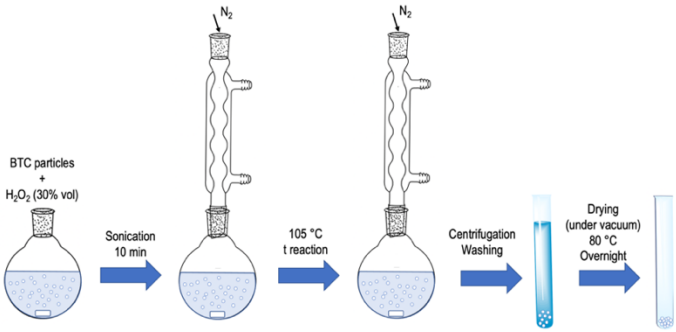

Figure 15 Hydroxylation procedure of $BaTiO_3$ nanoparticles. The mixture made by H_2O_2 and BTC particles is sonicated and then mixed at 105 °C with a reflux condenser for different reaction times. Particles are collected through centrifugation, washed with DI water, and dried under vacuum overnight.

1g of BTC was put in a round bottom flask together with 100 ml of H_2O_2 (30%vol). The mixture was ultra-sonicated in a bath sonicator (Ceia CP104) for 10 minutes to improve dispersibility and break particles' aggregates and clusters. After sonication, the mixture was kept under reflux at 105 °C for different reaction times: 2h, 4h, 8h, 24h, and 48h. After cooling to RT, hydroxylated particles were collected by centrifugation, washed three times with DI water, and finally dried at 80 °C under vacuum overnight. Hydroxylated particles were labeled respectively BTC_2, BTC_4, BTC_8, BTC_24, and BTC_48.

2.4 Particles' Functionalization

To identify the conditions leading to the highest yield of functionalization, preliminary studies were carried out using hydroxylated commercial barium titanate powders and GPTMS as a functionalizing agent. In detail, 0.450 g of hydroxylated particles were put in a round bottom flask with 30 ml of toluene. The mixture was sonicated for 10 minutes and then magnetically stirred under N_2 flux. 4.3 ml of GPTMS were slowly added to have a molar ratio GPTMS : $BaTiO_3$ = 10 : 1 and the mixture was refluxed at 120 °C for 24h under N_2 flow. After cooling down to RT, particles were collected through centrifugation, washed, and centrifuged twice with toluene, and dried overnight in a vacuum at 80 °C. BTC functionalized particles were labeled, in

dependence on the hydroxylation time, labeled as BTC_2_G, BTC_4_G, BTC_8_G, BTC_24_G, and BTC_48_G.

Following the results obtained from the hydroxylation-functionalization of BTC particles, BTH particles were hydroxylated using the optimal hydroxylation time and then functionalized with different organosilanes. Functionalization of BTH particles with GPTMS was performed using the same procedure previously described. The functionalization procedures with APEOPTES (A) and TESPEOD (T) were inspired by Maitra et al. [149]. 200 mg of hydroxylated BTH particles were put in a round bottom flask with 16 ml of n-hexane. The mixture was sonicated for 10 min. 0.28 ml of triethylamine (TEA) were slowly added under N_2 flux (weight ratio TEA : $BaTiO_3$ = 1) then APEOTES was slowly added in a molar ratio APEOPTES : $BaTiO_3$ = 2. The mixture was then heated at 75 °C and refluxed for 24h in an inert atmosphere (N_2 flow). After cooling, particles were collected through centrifugation, washed twice with acetone, and dried overnight in a vacuum at 80 °C. The functionalization with TESPEOD followed the same procedure employed for APEOTES, but functionalized particles were washed with n-hexane. Functionalized particles were labeled BTH_G, BTH_A, and BTH_T respectively for particles functionalized with GPTMS, APEOTES, and TESPEOD. Table 3 summarizes all the particle labeling depending on the stage of the study. The functionalization procedure is schematized in Figure 16.

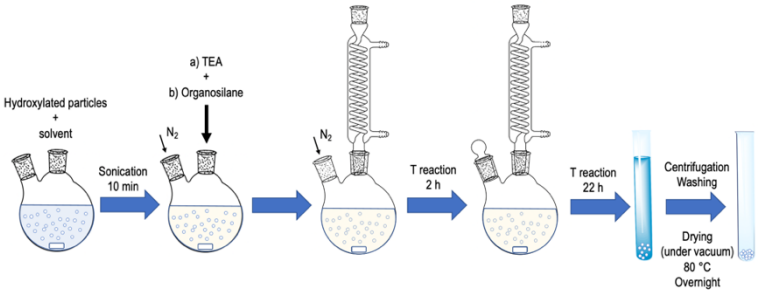

Figure 16 Schematization of functionalization procedure. First, hydroxylated particles are dispersed in an organic solvent through sonication, then TEA and the functionalizing agent are added, and the reaction is

carried out for 24h in an inert atmosphere. Particles are finally separated, washed, centrifuged, and dried overnight.

Table 3 Particle labeling depending on the particle type and stage of the process. The flags "HydroT" stands for hydrothermal treatment, and "G/A/T-funct" for functionalization with the relative organosilane.

Particle type	Label	Stage of process
Commercial	BTC	Bare
	BTC_2_G	2h hydroxylation + G-funct
	BTC_4_G	4h hydroxylation + G-funct
	BTC_8_G	8h hydroxylation + G funct
	BTC_24_G	24h hydroxylation + G funct
	BTC_48_G	48h hydroxylation + G funct
	BTC_G (GPTMS)	8h hydroxylation + G funct
Sol-Gel (Ambient Pressure)	BT	Bare (Annealing 900 °C)
Sol-Gel (Hydrothermal)	BTH	2h HydroT (Annealing 900 °C for all BTH)
	BTH_4h	4h HydroT
	BTH_6h	6h HydroT
	BTH_8h	8h HydroT
	BTH_G (GPTMS)	2h HydroT + 8h hydroxyl + G-funct
	BTH_A (APEOTES)	2h HydroT + 8h hydroxyl + A-funct
	BTH_T (TESPEOD)	2h HydroT + 8h hydroxyl + T-funct

2.5 Nanocomposites Production

Nanocomposites were produced with two different polymeric matrices, namely Epoxy Resin and PDMS adding bare and functionalized BTH particles as fillers.

1.5-2 mm thick disks were produced with both Epoxy Resin and PDMS, while films with thickness of about 100 μm were produced only with PDMS. The two production processes are summarized in this paragraph.

2.5.1 Thick Disks

To produce epoxy-based composites, 1.43 g of resin (Elan-Tron EC 251) were weighed in a beaker, and then, 5 ml of acetone were added while stirring. After homogenization, 0.56 g of hardener (Elan-Tron W 242) in a 100 : 40 weight ratio were added. Particles were slowly added while stirring in a closed vessel, the resultant white mixture was stirred in the closed vessel for 1 h and sonicated for 10 minutes. After that mixture was stirred for about 1 h to allow solvent evaporation and then degassed. Finally, an adequate volume of the mixture, to have final samples around 1.5 – 2 mm thick was poured into a cylindrical PTFE mold (2 cm diameter) equipped with Kapton-covered aluminum electrodes (Figure 17).

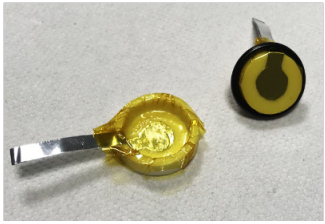

Figure 17 PTFE molds to produce thick disks. The molds are equipped with a Kapton-covered aluminum electrode. The counter mold (on the right) is also equipped with a Kapton-covered Al-electrode and an O-ring to keep the electrode in place and adjust the final thickness. [from [181] Zamperlin et al. Molecules 2022, 27(19), 6499, supplementary information]

The samples were further degassed, the molds were then closed with the counter electrode and put into a homemade polystyrene (PS) chamber at RT. The electrodes were connected to the HV power supply (Spellman SL3, Spellman high voltage electronics corporation). The temperature was then set at 80 °C, and the voltage was increased to have an applied electric field of about 3 kV/mm. The combined curing-poling step was carried out for 90 min. After this time both heating and voltage were turned off allowing natural cooling of the system. Samples were then removed from the molds.

For what concerns PDMS-based samples, the procedure was basically the same with few exceptions: 1.33 g of resin (Wacker Silgel 612 A) were mixed with 0.67 g of hardener and 5 ml

of pentane were added. The applied electric field was higher than for epoxy-composites, about 7 kV/mm. For samples prepared as thick disks, labeling, and composition are summarized in Table 4.

Table 4 Summary of all samples produced in the form of thick disks and their relative labeling.

Matrix	Filler content [vol %]	Particles	Composite labeling
Epoxy Resin	0	-	E_neat
	3.5	BTH	E_3.5_BTH
		BTH_G	E_3.5_BTH_G
		BTH_A	E_3.5_BTH_A
	21	BTH	E_21_BTH
		BTH_G	E_21_BTH_G
PDMS	0	-	P_neat
	3.5	BTH	P_3.5_BTH
		BTH_G	P_3.5_BTH_G
		BTH_A	P_3.5_BTH_A
	21	BTH	P_21_BTH
		BTH_G	P_21_BTH_G
FILMS	**Filler content [vol %]**	**Particles**	**Composite labeling**
PDMS	0	-	Pf_neat
	3.5	BTH	Pf_3.5_BTH
		BTH_G	Pf_3.5_BTH_G
		BTH_A	Pf_3.5_BTH_A
	14	BTH	Pf_14_BTH
		BTH_G	Pf_14_BTH_G

2.5.2 Films

PDMS-based films were prepared with a similar procedure, but the solution was applied to a polymethylmethacrylate (PMMA) substrate with Kapton-covered aluminum electrodes using a film applicator (Elcometer 4340 Automatic Film Applicator), with an application speed of about 3 cm/s, as shown in Figure 18. Sample labeling for composite films is reported in Table 4.

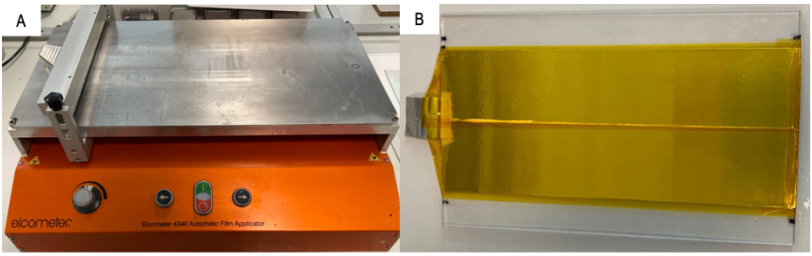

Figure 18 Setup to produce PDMS-based film composites. Figure A: the film applicator. Figure B: the plastic substrate with the Kapton-covered aluminum electrodes for the combined curing and poling procedure.

2.6 Characterization Techniques

2.6.1 Structural and Microstructural Characterization

Fourier-Transform Infrared Spectroscopy (FT-IR)

FT–IR spectroscopy was performed using two different instruments. FT–IR spectra of particles were acquired with a Thermo Nicolet Avatar 330 in transmission mode on KBr pellets with the following parameters: range 4000 – 400 cm^{-1}, 64 scans, resolution 4 cm^{-1}. Infrared spectra of composites were collected with a Varian 4100 FT–IR Spectrometer in ATR (Attenuated Total Reflectance) mode with the following parameters: diamond ATR crystal, range 4000 – 550 cm^{-1}, 64 scans, resolution 4 cm^{-1}.

Thermogravimetric Analysis – Differential Thermal Analysis (TGA-DTA)

TGA-DTA curves of hydroxylated and functionalized particles were collected with a TA Instruments TGA Q5000 between 30 and 800 °C and a heating rate of 10 °C/min in flowing air. The weight losses associated with the decomposition of the organosilane chains were calculated by the difference between the value at 800 °C and the value at the inflection point (350 – 400 °C). The results were then compared with quantitative NMR experiments.

Differential Scanning Calorimetry (DSC)

DSC analyses were carried out using a Mettler DSC30 (Mettler Toledo) in a temperature range from -30 to 100 °C for epoxy-based samples and from -160 to 100 °C for PDMS-based samples, with a heating/cooling rate of 10 °C/min.

X-Ray Diffraction (XRD)

XRD diffraction patterns were collected with a Rigaku III-D Max diffractometer (Rigaku, Tokyo, Japan), using CuKα radiation and a curved graphite monochromator in the diffracted beam. All samples were analyzed using the following parameters: 40 kV, 30 mA, 10°< 2θ < 90°, step 0.05°, acquisition time 2 s. The phase analysis was performed using JADE8 software (Materialsdata Inc., MDI, Livermore, CA, USA). Pattern analysis was performed with a Rietveld-based software, namely MAUD [156] (https://maud.radiographema.eu) to estimate the phase composition, lattice parameters, and crystallite size. To consider the instrumental broadening of the peaks during the deconvolution procedure, a calibration was performed using KCl as a reference material.

Nuclear Magnetic Resonance (NMR)

Solid state NMR spectra were collected with a Bruker 400WB spectrometer operating at a proton frequency of 400.13 MHz Cross Polarization - Magic Angle Spinning (CP-MAS) spectra were collected for ^{13}C, ^{29}Si, and ^{1}H. ^{13}C: frequency 100.48 MHz, contact time 2 ms, decoupling length 5.9 µs, recycle delay 3 s, 50 k scans (30 k scans for quantitative analysis of particles functionalized with GPTMS). ^{29}Si: frequency 79.48 MHz, contact time 5 ms, decoupling length 6.3 µs, recycle delay 10 s, 4 k scans. 1H: frequency 400.13 MHz, pulse length 5.0 µs, recycle delay 1s, 64 scans. Samples were put in 4 mm zirconia rotors and spun at 8 kHz in airflow. Adamantane and Q_8M_8 were used as external secondary references, Si species are labeled according to the usual ^{29}Si notation: T^n represents a SiO_3C unit with n equal to the number of bridging oxygens. Liquid-state NMR spectra of organosilanes were collected for ^{13}C and ^{29}Si. ^{13}C: frequency 100.48 MHz, π/2 pulse 7.2 µs, recycle delay 3 s, 1 k scans, decoupling length 80 µs. ^{29}Si: frequency 79.48 MHz, π/4 pulse 4.3 µs, recycle delay 15 s, 64 scans, decoupling length 5.2 µs. Samples were put in 4 mm zirconia rotors without spinning.

To quantitatively evaluate the degree of particle functionalization ^{13}C CPMAS experiments were performed by weighing the 4 mm zirconia rotors before and after filling them with functionalized $BaTiO_3$ particles. The areas of the ^{13}C resonances of methylene belonging to the propyl group of organosilanes were compared with the same resonances of the ^{13}C CPMAS spectrum of a known amount of a xerogel sample prepared with a 33 %mol of GPTMS as described elsewhere

[157] (GPTMS was considered completely hydrolyzed in the standard sample, STD); all the spectra were acquired and processed with the same parameters to allow the comparison.

Further solid-state NMR experiments called Relaxation Experiments [158] were carried out, here on ^{1}H nucleus, in order to achieve further insights about interactions at the interface in composite materials, which could affect the molecular structure, but also other intrinsic parameters, such as conformation and mobility that depend both on homonuclear and heteronuclear interactions. Accordingly, the proton spectrum intensity (M, "magnetization") as a function of t (a variable time interval, which depends on the specific experiment, during which M relaxes until the original equilibrium state is reached) can be recorded with various experiments to focus on different specific ranges of molecular dynamics. For all of them, the trend of M(t) is generally an exponential decay with a characteristic time constant. Three different experiments were tested in order to extract the time constants T_{1H}, $T_{2,}$ and $T_{1\rho(H)}$, which are related to different frequency ranges and therefore their values are sensitive to molecular motions on different time scales. The values are calculated by fitting the experimental curve with single or multiple exponential laws depending on homogeneity, segregation, and/or domain size [159,160].

For the present work the ^{1}H relaxation experiments were run on selected samples with a Bruker Advance III 400MHz, using saturation-recovery pulse sequence with variable relaxation delay in the range 0.001-20 s for T_1 evaluation, and spin-lock pulse sequence with variable spin-lock pulse in the range 0.5 – 500 ms (four different frequency fields from 11 to 70 kHz were used for the spin-lock field B1) for $T_{1\rho(H)}$. T_2 relaxation measurements were obtained using a Carr-Purcell-Meiboom-Gill (CPMG) pulse sequence [161,162] with a 180° pulse separation of 1 ms.

The saturation-recovery data (M decay curves) were fitted with by Mt = M0*[1-exp(-t/T)], which allows calculating the relaxation parameter T_{1H} (spin-lattice relaxation time) and both CPMG and spin-lock data with Mt = M0*[exp(-t/T)] for the evaluation of T_2 (spin-spin relaxation time) and $T_{1\rho(H)}$ (spin–lattice relaxation time in the rotating frame), respectively [159,160].

Field Emission Scanning Electron Microscopy (FE-SEM)

$BaTiO_3$ particles and composites were analyzed with a Carl Zeiss Gemini Supra 40 Field Emission Scanning Electron Microscopy (FE-SEM) using secondary electrons (SE) as the main signal with the following parameters: for particles accelerating voltage of 8 kV, magnification

80'000x; for composites accelerating voltage 7.5 – 10 kV at 20'000x, 10'000x, 5'000x, 2'000x, and 1'000x both. Before imaging, samples were metal sputtered with a Q150T coater (Quorum Technologies Ltd) with Pt/Pd-80/20 alloy. Particle size analysis was performed by ImageJ software (https://imagej.nih.gov/ij/, accessed on 29 July 2021).

Energy Dispersive X-Ray Spectroscopy (EDXS)

EDXS images were collected on composites with a Jeol JSM-5500 SEM equipped with an EDXS detector and an operating voltage of 20 kV at 2'000x, 1'000x, and 500x magnification.

Raman Spectroscopy

Raman spectra were acquired using a LabRAM Aramis (Horiba Jobin-Yvon) equipped with an optical microscope and a 100x objective. A diode-pumped solid-state laser source of 532 nm was used for the excitation of the Raman signal that was detected with an air-cooled charge-coupled device. A diffraction grating with 1800 lines mm^{-1} was used for the collection of all spectra with an overall spectral resolution of 1 cm^{-1}. Raman spectra were collected with an acquisition time of 4 s and a power set at 3 mW.

2.6.2 Electric and Dielectric Characterization

Piezoelectric measurements

Piezoelectric constant d_{33} of composites was measured with a Berlincourt type Piezo d33-(Piezoelectric meter PK3-2000-F10N, PolyK Technologies, State College (PA), USA) meter applying an oscillating force of 0.25 N with a frequency of 110 Hz.

Dielectric Spectroscopy

DS involves the application of an alternating voltage to the materials over a wide range of frequencies, and the experimental response is used to calculate various dielectric quantities such as the complex dielectric constant, loss factor, loss tangent, ac conductivity, complex modulus, and impedance. The dielectric constant is the most crucial quantity as it is linked to the ability of a material to store electrical energy. When an electric field is applied to an insulator, the dielectric material polarizes, with the negative charges orienting themselves toward the positive electrode and vice versa. This polarization effect opposes the applied field, accumulating energy in the capacitor. The ability to store energy in an electric field is the dielectric constant or relative permittivity ε_r, and the degree of polarization P is related to the

dielectric constant and electric field strength. A dielectric's total polarization comes from the sum of four sources of charge displacement: electronic displacement P_e, atomic displacement P_a, the orientation of permanent dipoles P_d, and space charge displacement P_s:

$$P_{tot} = P_e + P_d + P_a + P_s$$

The amount of charge stored in a material depends on how easily it can be polarized, resulting in higher stored electrical energy. However, different polarization mechanisms have different response times when subjected to an electric field. Thus, the activation of different polarization mechanisms at different frequencies of the applied alternating electric field (as shown in Figure 19) means that the net effective polarization to the dielectric constant is frequency dependent. Dielectric spectroscopy can explore and investigate all these mechanisms according to the microstructure and molecular structure of composites. The following is a brief overview and characteristics of the polarization mechanisms:

Electronic Polarization: This occurs in all atoms under the application of an electric field, where the nucleus of the atom and the center of its electron cloud shift away from each other, creating a tiny dipole with a very small polarization effect. Electronic polarization occurs rapidly and at frequencies up to 10^{15}.

Atomic (Ionic) Polarization: This effect occurs in ionic solids like ceramic materials, where the ions are symmetrically arranged in a crystal lattice with a net zero polarization. Once an electric field is applied, the cations and anions are attracted to opposite directions, creating a relatively large ionic displacement that can result in high dielectric constants in ceramics popularly used in capacitors. Atomic polarization is slower and occurs at frequencies up to 10^{10}.

Dipole (or Orientation) Polarization: Certain solids have permanent molecular dipoles that, under an electric field, rotate themselves in the direction of the applied field, creating a net average dipole moment per molecule. Dipole polarization occurs at frequencies less than 10^5 10^6 and is more common in polymers, which permit reorientation due to their atomic structure.

Space Charge (or Interfacial) Polarization: This phenomenon arises from extraneous charges that come from contaminants or irregular geometry in the interfaces of polycrystalline solids. These charges are partly mobile and migrate under an applied field, causing this extrinsic

type of polarization. Space charge polarization is the slowest and occurs at frequencies less than 10^0 - 10^1. Interfacial polarization phenomena are also known as Maxwell-Wagner-Sillars (MWS) interfacial polarization. When the frequency is reduced, the phenomenon of MWS interfacial polarization becomes significant. This can be observed through a peak in the dielectric loss, indicating the shift towards lower conductivity values. Additionally, an increase in the net permittivity values can also be noted, which is a common characteristic of interfacial polarization [163].

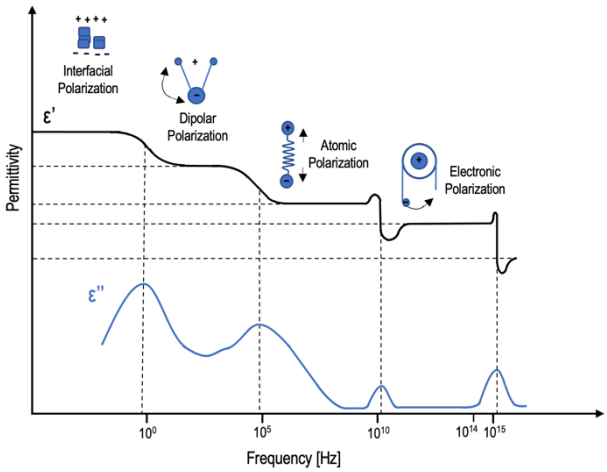

Figure 19 Influence of different types of polarization mechanisms on the real and imaginary part of permittivity in dependence on the frequency. Dealing with polymer-ceramic nanocomposites the analysis will be done at frequencies lower than 10^6 Hz.

In accordance with the described effects, Figure 19 shows the trend of the complex dielectric constant (both real and imaginary parts) as a function of the frequency; as the frequency of the applied electric field increases, the effectiveness of polarization mechanisms decreases, resulting in a decrease in the dielectric constant and capacitance value. In real-world dielectrics, relaxation time, or the lag of polarization mechanisms with frequency, generates dielectric

losses. In an AC circuit, the voltage and current across an ideal capacitor are 90 degrees out of phase. The angle by which the capacitor's current lags behind the ideal determines the material property called the loss tangent or dissipation factor (tan(δ)). Materials with higher dielectric constants typically have higher dissipation factors. The frequency at which a dielectric is used affects the relaxation time and therefore the losses generated. There are three cases to consider: in case 1, where the relaxation time is much longer than the field reversals, losses are small because ions cannot follow the field; in case 2, where the relaxation time is much faster than the field reversals, losses are small because polarizing processes can easily follow the field frequency; in case 3, where the relaxation time and field frequency are the same, losses are highest due to the lag of the ions. Ceramic dielectric formulations display a range of relaxation times over the frequency spectrum, resulting in a parameter known as the Q factor in high-frequency applications, which is the reciprocal of the loss tangent: $Q = 1/(\tan \delta)$.

DS measurements were performed with Novocontrol technologies Alpha-A High-Performance Frequency Analyzer with the following parameters: applied voltage 1-3 V, frequency range 10^{-2} - 10^{6} Hz, acquisition factor 1.6, temperature range -140 °C < T < 120 °C, electrode material Au (200 nm), electrode thickness 4 mm, material thickness 80 - 150 µm. For measurement at high/low T: 3 washing cycles with nitrogen (vacuum + N_2 filling). DS spectroscopy setup is shown in Figure 20.

Figure 20 Dielectric spectroscopy setup is reported. In Figure A: Low-Frequency Analyzer (1), System software (2). In Figure B: test cell (3), Linkam temperature controller (4), liquid nitrogen reservoir (5), vacuum pump (6). In Figure C: the inner part of the test cell, bottom electrode (7), top electrode/probe, (8).

Dielectric Breakdown

Dielectric breakdown (E_{BD}) measurements were performed on PDMS film composites. The setup is shown in Figure 21. A High Voltage (HV) source (5 kV) was connected to a Keithley oscilloscope that was used to impose a controlled voltage ramp. In the testing box, a plastic frame houses a spherical upper electrode connected to the HV and a grounded copper bottom electrode. The material was placed between the two electrodes. Finally, a multimeter was also connected to the testing box to register the breakdown voltage. E_{BD} measurements were carried out with the following parameters: voltage ramp 50 V/s, range 0 – 5000 V, 15 measurements per sample.

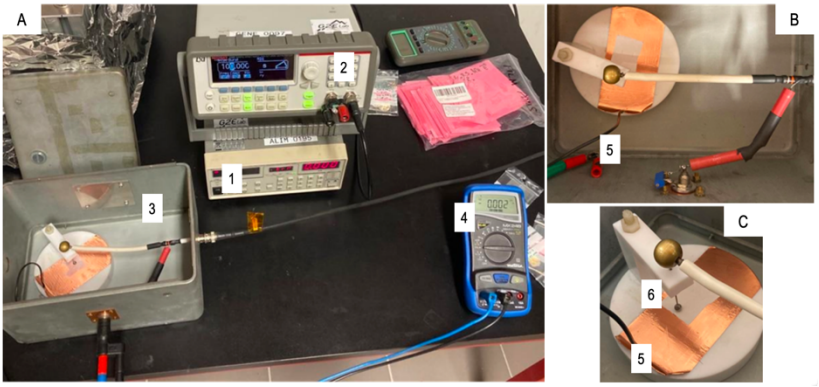

Figure 21 The setup for dielectric breakdown measurements is here reported. In Figure A: 5 kV HV source (1), Keithley oscilloscope (2), testing box (3), digital multimeter (4). In Figures B and C: plastic frame for the testing with the grounded bottom copper electrode (5) and the spherical top electrode (6) connected to the HV source.

Results and Discussions

This chapter is divided into two main sections, namely parts A and B. Part A will go through the entire production of polymer-ceramic composites, from the synthesis of the fillers to their functionalization, and finally to particles embedding in polymeric matrices to produce nanocomposites. At each step, materials have been thoroughly characterized to improve production processes. On the other hand, Part B will be focused on the electric, dielectric, and piezoelectric characterization of composites with particular attention to the properties of PDMS-$BaTiO_3$ films for energy harvesting purposes, ending with the calculation of the theoretical energy density that can be exploited by the nanocomposites.

Part A) $BaTiO_3$ Synthesis, Nanoparticles Functionalization, and Nanocomposites Production: Structural and Microstructural Characterization.

3.1 Synthesis of $BaTiO_3$ Nanoparticles: Ambient Pressure VS Hydrothermal Conditions

In the first step of the production process, barium titanate particles were synthesized via a sol-gel process at ambient pressure and in hydrothermal conditions (see paragraphs 2.2.1 and 2.2.2). The next paragraphs account for the effects of synthesis conditions on the microstructural features of $BaTiO_3$ nanoparticles as reported in the paper "Effect of Hydrothermal Treatment and Doping on the Microstructural Features of Sol-Gel Derived $BaTiO_3$ Nanoparticles" by Zamperlin et al. [155]

Preliminary studies (not reported) were done to optimize the Ba/Ti ratio in the wet synthesis. First, a Ba/Ti ratio equal to 1 was used but it led to the formation of some metastable non-stoichiometric phases such as $BaTi_2O_5$, $Ba_2Ti_5O_{11}$, and $Ba_4Ti_{13}O_{30}$, as also reported in the literature [101,164]. Accordingly, the Ba/Ti ratio was increased to 1.1 both for the synthesis at

ambient pressure and in hydrothermal conditions to reduce un-desired non-stoichiometric phases and obtain pure $BaTiO_3$.

3.1.1 Ambient Pressure vs Hydrothermal Conditions

Barium titanate powders were annealed at 900 °C with an isothermal step of 4 h to promote the cubic-to-tetragonal phase transformation of $BaTiO_3$ using the lowest possible annealing temperature. The thermal treatment was set up based on the results of the powders' thermogravimetric analysis. Figure 22 shows TG-DTA curves of BT powders produced at ambient pressure in the range of 20 – 1000 °C. In the TG curve, two weight loss steps can be identified: the first (about 6 % wt. loss) between 20 and 800 °C is ascribable to the condensation of surface hydroxyl groups, the combustion of organic residuals from the synthesis and the decomposition of some barium carbonate ($BaCO_3$) impurities; the second weight loss is much weaker (about 1 %) and can be attributed to the release of lattice hydroxyl defects that are typical of powders prepared by wet chemical syntheses [165]. The sample seems to be thermally stable above 900 °C; in fact, according to Ashiri et al. [166] above 800 °C $BaCO_3$ is completely removed, and the transformation of barium titanate is completed. The DTA curve in Figure 22 presents a broad exothermic peak centered at 386 °C that is ascribable to the burning of residual organics, $BaCO_3$ decomposition, and possible intermediate phases [167]. Literature reports different temperatures for the transformation into the tetragonal phase. The cubic-to-tetragonal phase transformation was reported at 850 °C [166] but it was also demonstrated that the tetragonal phase starts to appear even from 600 °C [168]. The appearance of the tetragonal phase at "low temperatures" can be due to the formation of intermediate structures in the short-range environment of the crystal lattice. Accordingly, the exothermic peak centered around 740 °C is ascribed to the crystallization of $BaTiO_3$ in the tetragonal phase [78].

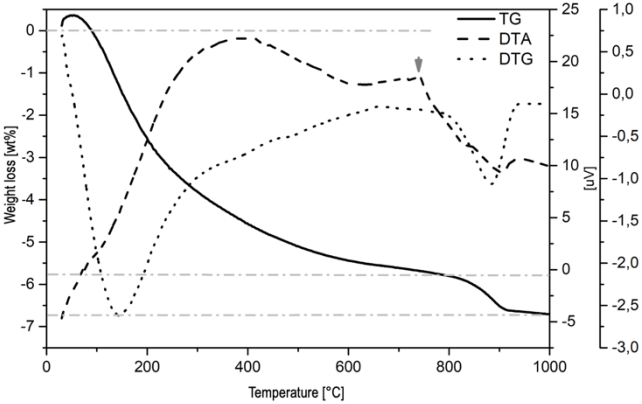

Figure 22 Thermogravimetric analysis of BT powders. TG, DTA, and DTG curves in the range RT-1000 °C are reported. The arrow indicates the tetragonal phase crystallization. [Adapted from [155] Zamperlin et al., Materials, 2021, 14(15), 4345]

Structural and microstructural analyses of particles were obtained by FTIR, XRD, and SEM techniques. Figure 23 shows the FTIR spectra of BT and BTH (prepared with 2h hydrothermal treatment), in both as-prepared and annealed conditions. Metal-Oxygen (M-O) vibrations are usually found below 800 cm^{-1}, for $BaTiO_3$ the Ti-O stretching and Ti-O-Ti bending vibrations were centered at 550 and 425 cm^{-1}, respectively [166,169]. In the spectrum of BT and BTH particles (Figure 22, left), several signals are found in the region 1700 – 1250 cm^{-1}. The main component is located around 1444 cm^{-1} [170] and can be related to the normal vibration of carbonate groups; also, peaks related to residual acetate are detected in the range 1550 – 1300 cm^{-1} [171–173]. The band centered at 1630 cm^{-1} is attributed to the scissoring vibration of adsorbed water and the -OH stretching band is found at 3500 cm-1. It is worth noting that particles produced via hydrothermal synthesis present narrower M-O peaks and much less intense signals related to acetate residuals. The annealing step, (Figure 23 right) results in the almost disappearance of peaks related to carbonate vibration and acetate residuals, in agreement with the results of thermogravimetric analyses. The FTIR spectrum of BTC, reported in Figure 23 (right) for the sake of comparison, does not present noticeable differences with respect to BTH powders, except for the peak shape of Ti-O and Ti-O-Ti signals, proving the goodness of hydrothermal synthesis with respect to a solid-state route.

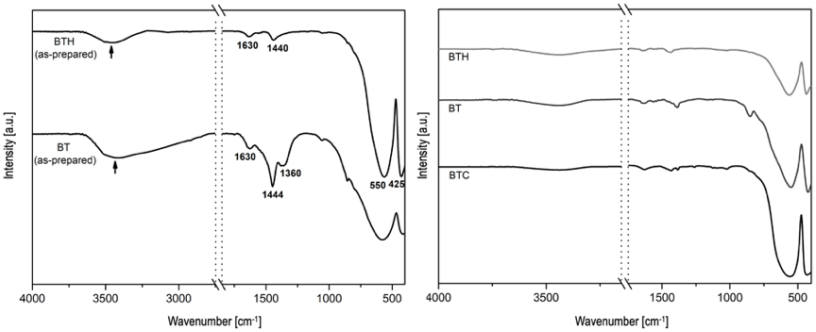

Figure 23 FTIR spectra of powders produced by the sol-gel method at ambient pressure (BT) and with 2h hydrothermal treatment (BTH) as prepared (left) and after annealing at 900 °C (right). BTC spectrum is also reported for the sake of comparison. [Adapted from [155] Zamperlin et al. Materials, 2021, 14(15), 4345]

Parameters affecting the piezoelectric performance are tetragonality, phase compositions, grain size, domain size, and orientation [174,175]. Accordingly, X-Ray diffraction patterns were acquired on all samples to estimate the phase composition, lattice parameters, crystallinity, and crystallite size. Figure 24 shows XRD patterns of BT, BTH, and BTC (for the sake of comparison) powders. Diffraction patterns of BT and BTH samples evidenced the presence of both tetragonal and cubic phases. In fact, the tetragonal phase of $BaTiO_3$ (PDF 5-626) is characterized by the presence of a doublet at the diffraction angle $2\theta = 45°$, the cubic phase (PDF 31-174) by a single peak, and the coexistence of the two phases by a peak and a shoulder [176,177]. BTC diffraction pattern has a doublet at $2\theta = 45°$ while both BT and BTH powders present a mixed situation, with the coexistence of tetragonal and cubic phases. No further phases are detected in BTH (except for cubic and tetragonal) while BT powders present traces of $BaTi_2O_5$ (monoclinic, PDF 8-368). Ritter et al. [164] demonstrated that different Ba-Ti oxides such as $BaTi_2O_5$, $BaTi_5O_{11}$, and Ba_2TiO_4 can form depending on the Ba/Ti ratio. These metastable phases can crystallize around 700 °C and they are stable up to 900 – 1100 °C. The formation mechanisms of these oxides are still unclear and very complex, but both water and acetic acid used in the synthesis are supposed to play a key role. Rietveld analysis was performed on the diffraction pattern to evaluate phase composition and lattice parameters, results are summarized in Table 5. Compared to BTC powders that present a 100% tetragonal phase,

BTH and BT particles show the coexistence of tetragonal and cubic phases, and the BT sample presents traces of additional metastable phases. Concerning lattice parameters and consequently tetragonality, BTC particles show the highest achievable value of tetragonality, 1.010 [178]. However, BTH powders display a very good value of tetragonality (1.007), which is higher with respect to particles produced at ambient pressure (1.003).

Table 5 Size distribution, quantitative phase analysis, crystallite size, lattice parameters, and tetragonality value of commercial particles (BTC) and particles produced via wet chemical synthesis at ambient pressure (BT) and in hydrothermal conditions (BTH). [Adapted from [155] Zamperlin et al. Materials, 2021, 14(15), 4345]

Property [unit]	**BTC**	**BT**	**BTH**
Size [nm] (std. dev)	496 (178)	376 (99)	117 (27)
Phase [wt. %] (std. dev)	Tetragonal 100	Tetragonal – Other 85(2) – 15(2)	Tetragonal – Cubic 75(1) – 25(1)
Crystallite size [nm] (std. dev)	114(1)	46(1) – n.a.	77(4) – 82(14)
a [Å]	3.9995	4.0105	4.0039
c [Å]	4.0393	4.0239	4.0333
t = c/a	1.0100	1.0033	1.0074
Rwp [%]	15.09	12.94	18.05

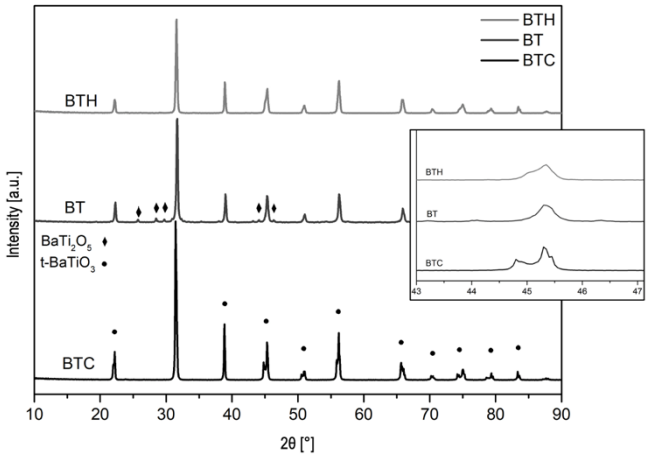

Figure 24 XRD patterns of BT, BTH, and BTC (for the sake of comparison) powders. The respective signals at 2θ = 45° are magnified in the inset on the right. [Adapted from [155] Zamperlin et al. Materials, 2021, 14(15), 4345]

Raman spectra were collected on powders produced by wet chemical synthesis and compared with commercial powders, the spectra of BTC, BT, and BTH powders are reported in Figure 25. Raman spectroscopy is a very sensitive spectroscopic technique to probe the short- and mid-range structure in materials. The scattering Raman bands at 250, 520, and 720 cm^{-1} and the peak at 306 cm^{-1} are characteristic signals of tetragonal $BaTiO_3$ as reported in literature [179]. The typical Raman-active modes of tetragonal $BaTiO_3$ are detected, in the specific, the $A_1(TO_2)$ around 270 cm^{-1}, the $A_1(LO_2)/E(TO_3)$, and the B_1 (reported in Figure 25); the phonon modes were attributed according to Dixit et al. [180] while the anti-resonance at 183 cm^{-1} is attributed to the coupling of $A_1(TO_1)$ and $A_1(TO_2)$ modes [181]. Raman spectroscopy confirms the findings from XRD spectroscopy, the lower tetragonality of BTH and BT with respect to BTC particles is proved from the lower intensity of the peak centered at 306 cm^{-1}.

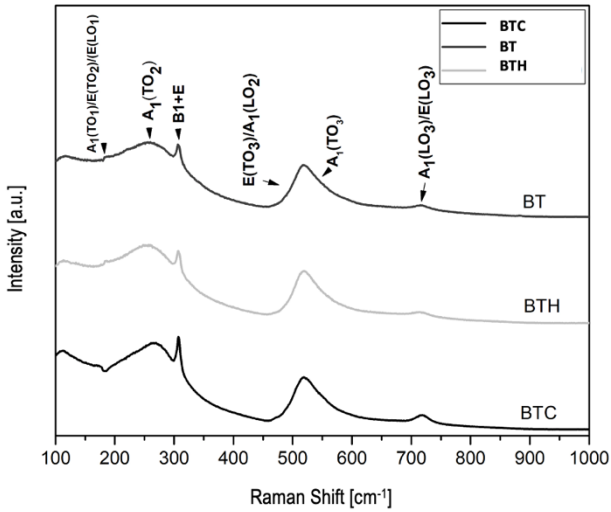

Figure 25 Raman spectra of BaTiO3 powders for BT, BTH, and BTC as a comparison. The main active modes are also reported in the figure. [Adapted from [155] Zamperlin et al. Materials, 2021, 14(15), 4345]

Particles' morphology, aspect ratio, and size distribution were investigated by means of SEM imaging. SEM micrographs of BTC, BT, and BTH particles are shown in Figure 26. The results of particle analysis done with ImageJ are summarized in Table 5. Commercial particles have a mean size of around 500 nm, broad size distribution, and irregular morphology. On the contrary, both BT and BTH samples produced via wet chemical synthesis present spherical morphology, furthermore, particles produced in hydrothermal conditions are smaller (average particles' diameter is 117 nm for BTH with respect to 376 nm for BT) and present narrower size distribution. Both BT and BTH particles result from the agglomeration of primary particles [79,81], as clearly visible in the zoomed SEM images of BT and BTH in Figure 27.

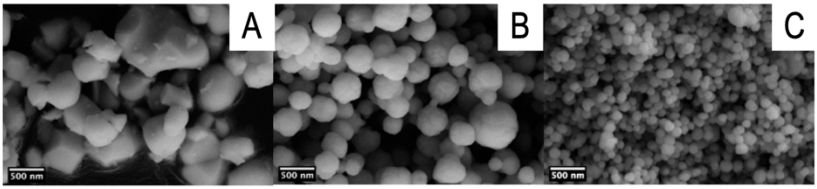

Figure 26 SEM micrographs of BTC (A), BT (B), and BTH (C) particles. [Adapted from [155] Zamperlin et al. Materials, 2021, 14(15), 4345]

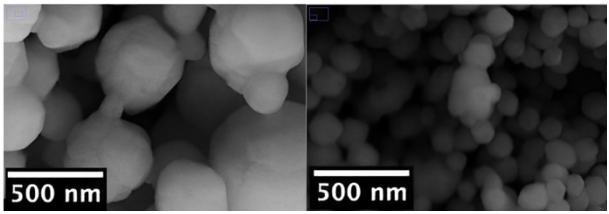

Figure 27 Zoomed images of BT (left) and BTH (right) particles showing the particles' formation resulting from the agglomeration of primary particles.

According to the previous findings, powders produced by the sol-gel synthesis in hydrothermal conditions present the best characteristics. In fact, particles produced by hydrothermal synthesis are spherical and with a very narrow size distribution with respect to standard solid-state synthesis and the classic sol-gel route. Even in their as-prepared state, BTH powders present fewer residual organics. In addition to that, XRD proved BTH particle purity, and the Rietveld refinement of XRD patterns showed a good amount of tetragonal phase and a high value of tetragonality compared to BT. Accordingly, we decided to focus on the production of particles in hydrothermal conditions. The next paragraph will analyze the effect of varying the hydrothermal reaction time on particle morphology and microstructural features.

3.1.2 Hydrothermal Reaction Studies

The evaluation of the effect of different hydrothermal reaction times on the microstructural features of particles produced by hydrothermal synthesis was done by means of SEM analysis and X-Ray Diffraction. Figure 28 shows SEM micrographs of BTH powders at different hydrothermal reaction times [77]. By increasing the hydrothermal reaction time from 2 to 8 h there are no relevant effects on the particles' dimensions; there is a slight increase from 117 nm to 162 nm accompanied by a broader size distribution. Results are summarized in Table 6. Concerning the aspect ratio, higher hydrothermal reaction times lead to slightly bigger and elongated particles which start to form necks and agglomerates with an 8 h reaction time that is detrimental to particles' dispersibility in composites. Accordingly, shorter reaction times are preferable.

XRD patterns were acquired on all samples. The results of the Rietveld refinement are summarized in Table . Concerning the phase composition, the amount of tetragonal phase is around 75% independent of the hydrothermal reaction time. The overlapping of the characteristics diffraction signals of tetragonal and cubic phases can affect the evaluation of crystallite size, resulting in higher errors in the values for the cubic phase. Crystallite size is about 75-77 nm for powders produced in hydrothermal conditions, compared to BTC and BT powders that present crystallite dimensions respectively of 114 and 46 nm (Table 6). Finally, Figure 29 shows the trend of the tetragonality value against the hydrothermal reaction time. In the range of reaction times used (2 – 8 h), the effect on the lattice parameter is poor and consequently, the value of tetragonality is almost constant.

Table 6 Size distribution, quantitative phase analysis, crystallite size, lattice parameters, and tetragonality value of particle produced under hydrothermal conditions. [Adapted from [155] Zamperlin et al. Materials, 2021, 14(15), 4345]

Property [unit]	BTH	BTH_4h	BTH_6h	BTH_8h
Size [nm] (std. dev)	117 (27)	127 (31)	131 (40)	162 (56)
Phase [wt. %] (std. dev)	Tetragonal – Cubic 75(1) – 25(1)	Tetragonal – Cubic 73(3) – 27(3)	Tetragonal – Cubic 74(3) – 26(3)	Tetragonal – Cubic 78(2) – 22(2)

Crystallite size [nm] (std. dev)	77(4) – 82(14)	75(1) – 114(18)	73(3) – 92 (16)	75(4) – 171(46)
a [Å]	4.0039	4.0053	4.0049	4.0042
c [Å]	4.0333	4.0305	4.0318	4.0342
t = c/a	1.0074	1.0062	1.0069	1.0075
Rwp [%]	18.05	20.00	16.04	15.43

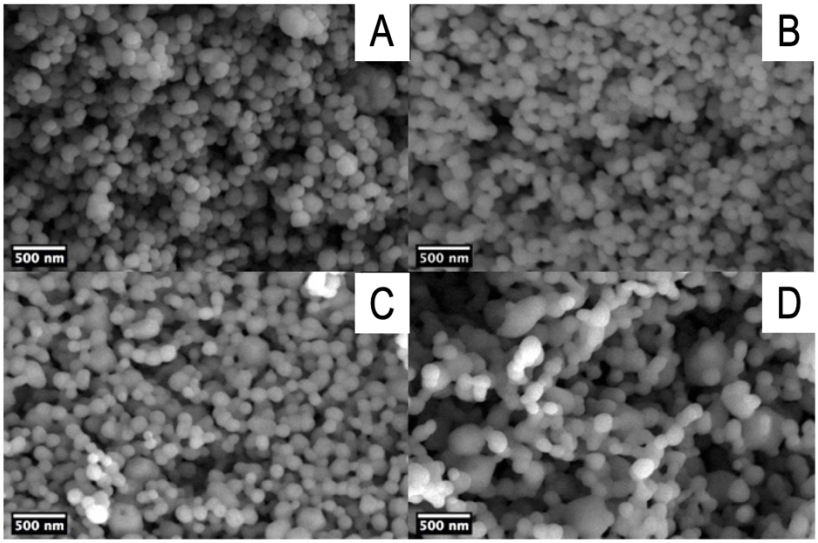

Figure 28 SEM micrographs of BTH particles produced at different hydrothermal reaction times, in the specific: 2h (A), 4h (B), 6h (C), and 8h (D). Coalescence and necks among particles are found in 8h sample. [Adapted from [155] Zamperlin et al. Materials, 2021, 14(15), 4345]

These findings point out that shorter hydrothermal reaction times result in better properties of the final powders in terms of aspect ratio, size distribution, amount of tetragonal phase, and tetragonality. Furthermore, shorter reaction times allow a faster process with reduced energy consumption.

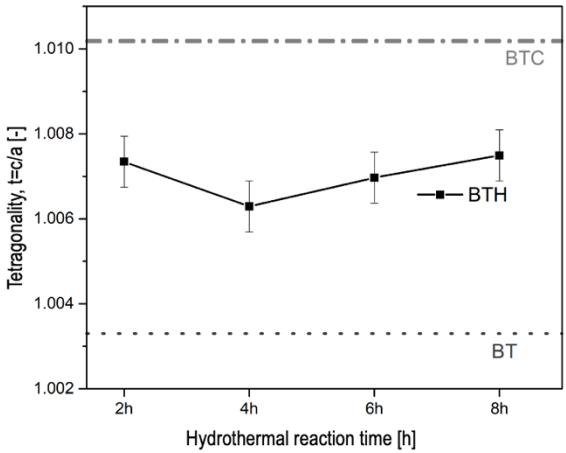

Figure 29 Trend of the tetragonality value (c/a ratio) as a function of the hydrothermal reaction times. The figure also reports the reference line values for BTC particles and for particles produced via the sol-gel method at ambient pressure (BT). [Adapted from [155] Zamperlin et al. Materials, 2021, 14(15), 4345]

3.2 Hydroxylation Process

This paragraph is based on the article by Zamperlin et al. on the functionalization of barium titanate nanoparticles with different organosilanes [182] focusing on the hydroxylation studies. The process of particle functionalization started with particle hydroxylation. As explained in paragraph 1.5.1 crystalline $BaTiO_3$ particles are poorly reactive. Thus, to improve the grafting efficiency surface hydroxylation was carried out. The hydroxylation studies were performed on commercial particles (BTC), which were reacted with H_2O_2 for different reaction times and then functionalized with 3-glycidyloxtrimethoxysilane.

3.2.1 Effect of Hydroxylation Time on Particles Morphology

SEM micrographs of hydroxylated BTC particles are shown in Figure 30. Bare BTC powders have an average diameter of about 500 nm as reported in Table , they present a limited degree of aggregation and broad size distribution. The degree of aggregation seems to be enhanced

by the hydroxylation steps, especially for higher hydroxylation times such as 24 h and 48 h. The increased aggregation reduces the available surface not favoring functionalization, as it will be confirmed by thermogravimetric analysis and NMR spectroscopy in the following paragraph.

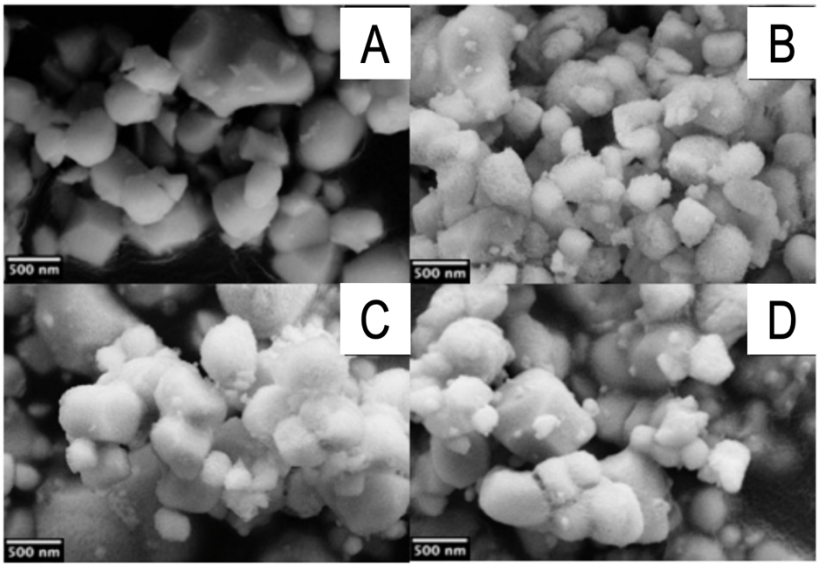

Figure 30 SEM micrographs of BTC particles (A) and BTC particles hydroxylated for different reaction times: 8h (B), 24h (C), and 48h (D). [Adapted from [181] Zamperlin et al. Molecules 2022, 27(19), 6499]

3.2.2 Effect of Hydroxylation Time on Particles Functionalization

EDXS elemental maps of Si, Ti, and Ba were collected for particles showing the highest weight loss, namely BTC_8_G, BTC_24_g, and BTC_48_G, maps are reported in Figure 31. The signal of silicon, due to the presence of grafted GPTMS on the surface of the particles is clear in all the analyzed samples, proving the effective functionalization.

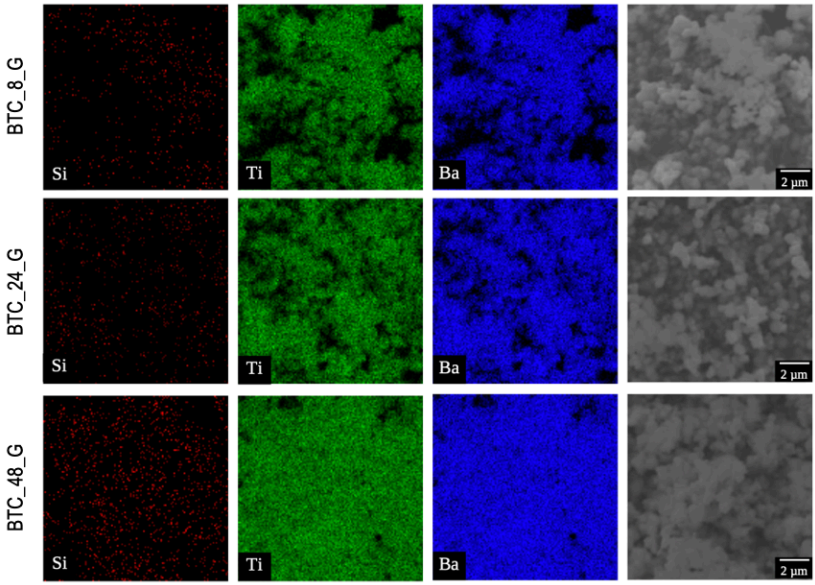

Figure 31 EDXS elemental maps of Si (red), Ti (green), and Ba (blue) of BTC particles hydroxylated at 8, 24, and 48 h and functionalized with GPTMS. Namely, BTC_8_G, BTC_24_G, and BTC_48_G.

The effect of different hydroxylation times was studied by FTIR spectroscopy. Figure 32 shows FTIR spectra of hydroxylated and GPTMS-functionalized BTC particles. Characteristics Ti-O and Ti-O-Ti signals around 550 and 430 cm^{-1} are found in all samples and they tend to be slightly narrower by increasing the hydroxylation reaction time. Hydroxylated particles present stronger signals due to OH stretching vibrations at 3500 cm^{-1}, in particular in the sample BTC_8 (commercial particles subjected to an 8h hydroxylation process). Concerning functionalized particles, their spectra present some differences with respect to hydroxylated particles, especially in the region 1200 – 1000 cm^{-1}, 1500 – 1350 cm^{-1}, and for the modification of some signals in the region 3000 – 2800 cm^{-1}. For example, the signals at 1195 cm^{-1} and 1106 cm^{-1} can be respectively attributed to CH_3 rocking vibrations of non-hydrolyzed methoxy groups of GPTMS and to Si-O asymmetric stretching of condensed GPTMS. The weak, broad band between 1500 and 1350 cm^{-1} can be attributed to C-H vibration deformations of GPTMS, while

the small shoulder at 908 cm^{-1} that can be detected in BTC_8_G and BTC_24_G can be assigned to the signal of asymmetric deformation vibration of the monosubstituted epoxy ring. Furthermore, the appearance of weak signals at 2940 and 2870 cm^{-1} in particular for the sample BTC_8_G also indicates the grafting of GPTMS to the particles. Finally, all the functionalized spectra present reduced intensities for peaks related to -OH vibrations with respect to non-functionalized particles.

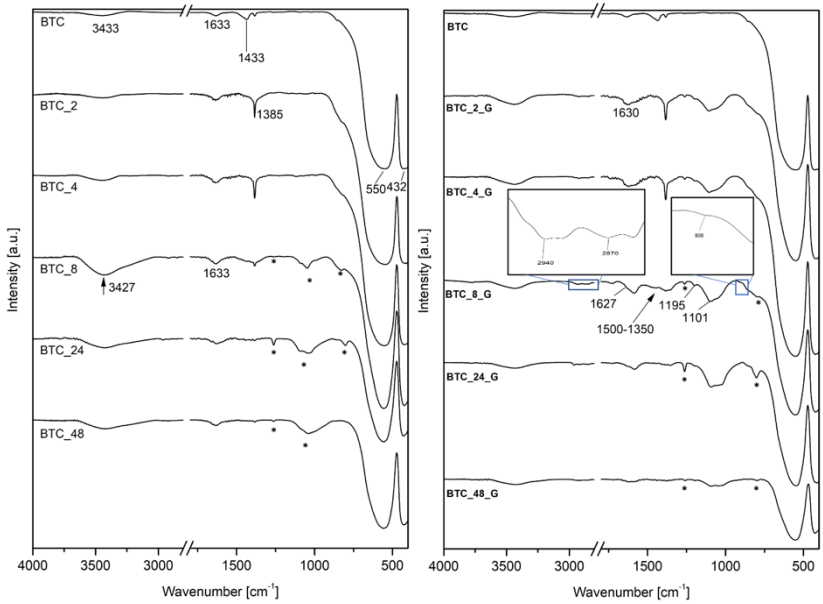

*Figure 32 FTIR spectra of commercial barium titanate particles (BTC): hydroxylated with different reaction times (on the left), and after functionalization (on the right). The spike at 1385 cm^{-1} is an instrumental artifact. Signals identified by * are due to silicone grease pollution of samples (as confirmed by ^{29}Si NMR analyses).*

Thermogravimetric analyses were performed on functionalized particles, and by looking at the weight loss in the region 300 – 600 °C the yield of functionalization was evaluated and compared with the results of NMR analyses.

Figure 33 shows the TG curves of BTC particles hydroxylated at different reaction times (4, 8, 24, and 48 h), and then functionalized with GPTMS. Two main loss steps were identified. The first weight loss occurs in the region of 100 – 300 °C due to the loss of adsorbed water and residual hydroxyl groups, and it is more pronounced in BTC_8_G and BTC_24_G. The second weight loss in the region of 300 – 600 °C is ascribable to the thermal decomposition of organic groups of GPTMS, the functionalizing agent. BTC_8_G is the sample with the highest weight loss in this range, resulting in a more effective functionalization with respect to samples prepared with longer hydroxylation times, which probably favor the condensation of -OH groups making available a lower number of hydroxyl groups for GPTMS grafting. The weight losses, reported in Table , were used to calculate the number of grafted molecules per square nanometer (molecules/nm^2) attached to the particle surface (see next paragraph).

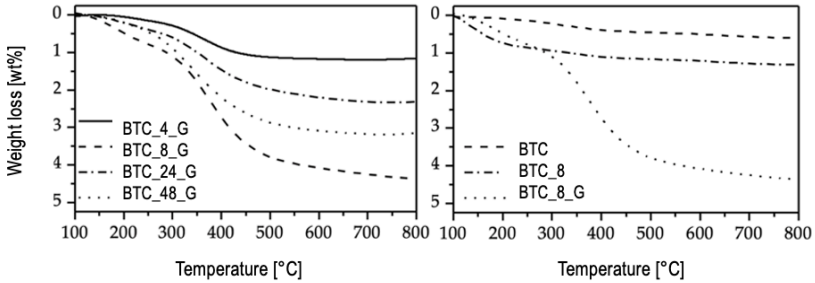

Figure 33 Left: TGA curves of BTC particles hydroxylated at different reaction times and then functionalized with GPTMS. Right: TGA curves of pristine BTC, 8 h hydroxylated BTC, and 8 h hydroxylated and functionalized BTC. TGA plots are shown in the range of 100 – 800 °C. No evident thermal phenomena below 100 °C. [Adapted from [181] Zamperlin et al. Molecules 2022, 27(19), 6499]

NMR analyses were performed to have further insights into the GPTMS grafting and to quantitatively evaluate the yield of the functionalization in correlation with the hydroxylation time. Carbon-13 solid-state NMR experiments were carried out on functionalized BTC samples to evaluate the degree of condensation of the organosilane (GPTMS), check the organic chain integrity, and calculate the yield of functionalization. ^{13}C CPMAS spectrum of functionalized

BTC particles subjected to 8h hydroxylation (BTC_8_G) is reported in Figure 34, together with the GPTMS spectrum for the sake of comparison; resonances are assigned according to the scheme in the figure. Resonances of methylene carbons are located at 9 (1), 23 (2), and 73.1 (3, 4) ppm; methine (6) and methylene (5) resonances of epoxy carbons are located respectively at 43.1 and 50.9 ppm [157]. The -OCH_3 signal at 50 ppm almost disappears in BTC_8_G, evidence of complete hydrolysis of the organosilane. Focusing on peak 1, the signal is broad and shifted downfield with respect to the pure reagent; this can be explained both with GPTMS grafting onto the particles and partial self-condensation of the organosilane. Furthermore, the reduced intensity of peaks 5 and 6 is a hint of a partial epoxy ring opening accompanied by diol formation, this is confirmed by the weak resonance at 64.8 ppm and by the intensities of peaks 3 and 4.

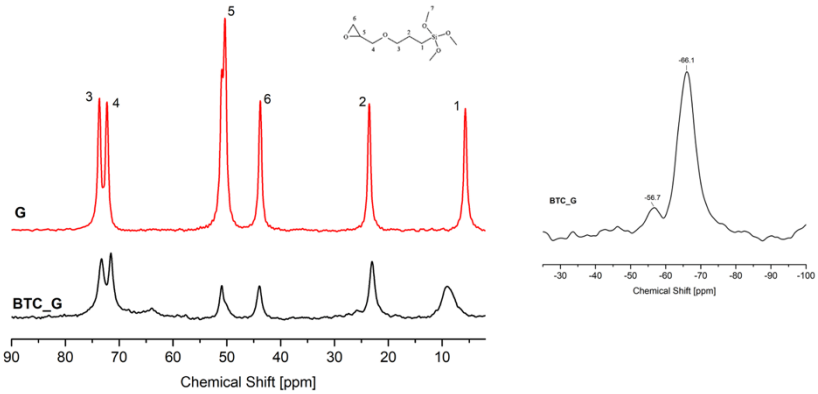

Figure 34 Left: [13]C CPMAS NMR spectra of neat GPTMS (G) and BTC particles functionalized with G after a hydroxylation step of 8 h; carbon atoms are labeled according to the GPTMS scheme shown on the top of the figure. Right: [29]Si CPMAS NMR spectrum of BTC particles functionalized with G after an 8 h hydroxylation step. [Adapted from [181] Zamperlin et al. Molecules 2022, 27(19), 6499]

The condensation of the grafted organosilane is confirmed by the [29]Si CPMAS spectrum, also reported in Figure 34. The spectrum of BTC_8_G presents a signal at -56.7 ppm, and it is due to $SiCO_3$ units with two bridging oxygens (T^2 units) and the main resonance at -66.1 ppm representative of fully condensed $SiCO_3$ units (T^3 units). The T^2/T^3 ratio is 7/93.

Quantitative analysis of grafted organosilane on the BTC surface was done using the procedure described in Chapter 2. In detail, zirconia rotors were weighed before and after filling with the samples, and a standard (STD) was prepared using a mixture of GPTMS, MTES, and TEOS as described by Fedel et al. [157]. For standard sample (STD) moles calculation, GPTMS was considered completely hydrolyzed. ^{13}C CP-MAS spectra were collected and signals were integrated based on the methylene resonance of the propyl group of GPTMS. The ratio between the area of these peaks and the STD peak area is multiplied by the moles of the STD to obtain the number of moles of GPTMS. To obtain the GPTMS relative weight amount the moles of GPTMS were multiplied by the MW of GPTMS and divided by the sample weight. Results are reported in Table 7; quantitative analyses from TGA and NMR are in good agreement, showing that a hydroxylation reaction time of 8 h leads to the best results in terms of yield of functionalization.

Table 7 Amount of grafted GPTMS on commercial $BaTiO_3$ particles (BTC) hydroxylated with different reaction times, calculated both from thermogravimetric analyses and quantitative nuclear magnetic resonance experiments. [Adapted from [181] Zamperlin et al. Molecules 2022, 27(19), 6499]

	BTC_4_G	BTC_8_G	BTC_24_G	BTC_48_G
TGA [wt. %]	0.6	2.1	1.4	1.8
NMR [wt. %]	0.8	2.4	1.7	2.0

Therefore, the 8 h hydroxylation step was selected for improving the reactivity towards the functionalization with different organosilanes of particles produced by hydrothermal synthesis with a hydrothermal reaction time of 2 h, namely BTH powders.

3.3 Particles Functionalization

This paragraph presents the results on the functionalization of BTH nanoparticles with different organosilanes reported in “Barium Titanate Functionalization with Organosilanes: Effect on Particle Compatibility and Permittivity in Nanocomposites” by Zamperlin et al. [182].

Figure 35 shows TG and DTG curves of BTH particles hydroxylated for 8h and functionalized with GPTMS, APEOTES (2-[acetoxy(polyethyleneoxy)propyl]triethoxysilane), and TESPEOD (triethoxysilyl-propoxy(polyethyleneoxy)dodecanoate), i.e. respectively BTH_G, BTH_A, and BTH_T samples. It is worth noting, that hydroxylated BTH particles present a similar behavior to hydroxylated commercial particles Figure 33 but the final weight loss is almost double with respect to BTC powders. The difference in weight loss is ascribable to a higher amount of hydroxyl groups on the surface of the particles that act as active grafting sites for functionalizing agents, thus improving functionalization. Functionalized particles, namely BTH_G, BTH_A, and BTH_T, have a similar trend to BTC_G powders, with a first weight loss in the region below 300 °C due to loss of residual hydroxyl groups and adsorbed water and a second weight loss in the region above 300 – 350 °C ascribable to the decomposition of organic chains of silanes, suggesting a successful functionalization; the TG/DTG curves of the two PEO-based organosilanes are very similar, the inflection points ascribable to the organic chain decomposition are located at 327 °C and 350 °C respectively for A and T-functionalized particles.

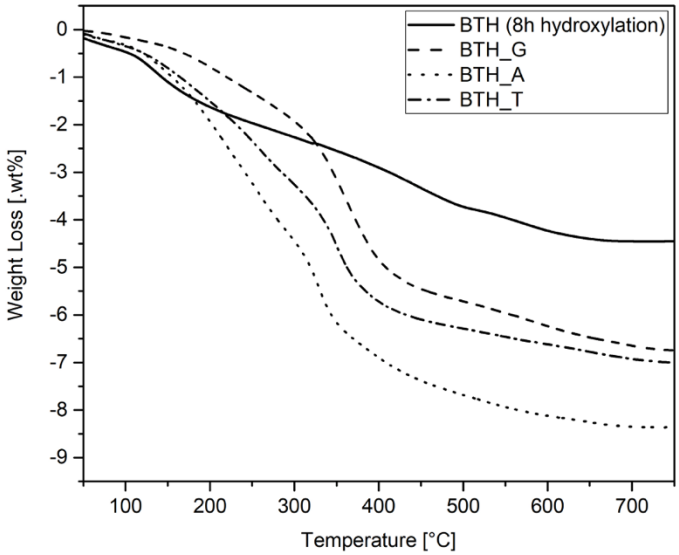

Figure 35 TG/DTG curves of BTH particles hydroxylated, and BTH particles functionalized respectively with G, A, and T.

The presence of functionalizing agents on the particles' surface was confirmed by FTIR spectroscopy (Figure 36). All the samples present the typical $BaTiO_3$ signals below 600 cm^{-1}, in the specific centered at 561 and 432 cm^{-1} related to Ti-O and Ti-O-Ti vibrations of the TiO_6 octahedron, moreover, the shape of the signal is different from commercial powders, being narrower. Figure 36 shows the FTIR spectra of BTH particles after the hydroxylation and functionalization steps. Hydroxylated BTH particles (BTH_8) present more intense signals related due to hydroxyl groups at 3433 cm^{-1}, and at 1633 cm^{-1} with respect to as-prepared BTH and corresponding hydroxylated BTC (Figure 32). The broadband in the region 1100 – 1000 cm^{-1} in spectra of functionalized particles is due to siloxane bonds, as observed in G-functionalized BTC (Figure 32). The FTIR spectrum of BTH_G is comparable to that of BTC_G, while spectra of BTH_A and BTH_T present a few more signals related to the different organic chains. In all three BTH_G, BTH_A, and BTH_T, the appearance of a broad band in the region 1100-1000 cm^{-1} is due to siloxane (Si-O) stretching vibrations coming from the condensation of

the organosilanes. Furthermore, the signal at 952 cm^{-1} is attributed to C-O-C symmetric stretching of the PEO segment in PEO-silanes; this signal is more evident in A-functionalized particles due to the longer PEO-segment in APEOTES (A) with respect to TESPEOD (T). Again, the peak at 1735 cm^{-1} is attributed to the stretching of C=O in the acetate terminal group of APEOTES while the peak centered at 1253 cm^{-1} can be ascribed to the C-O-C symmetric stretching of the acetate group. Concerning the T-functionalized sample, the spectrum presents more intense signals at 2920 and 2854 cm^{-1} assigned respectively to the asymmetric and symmetric C-H stretching vibrations of the dodecanoate chain.

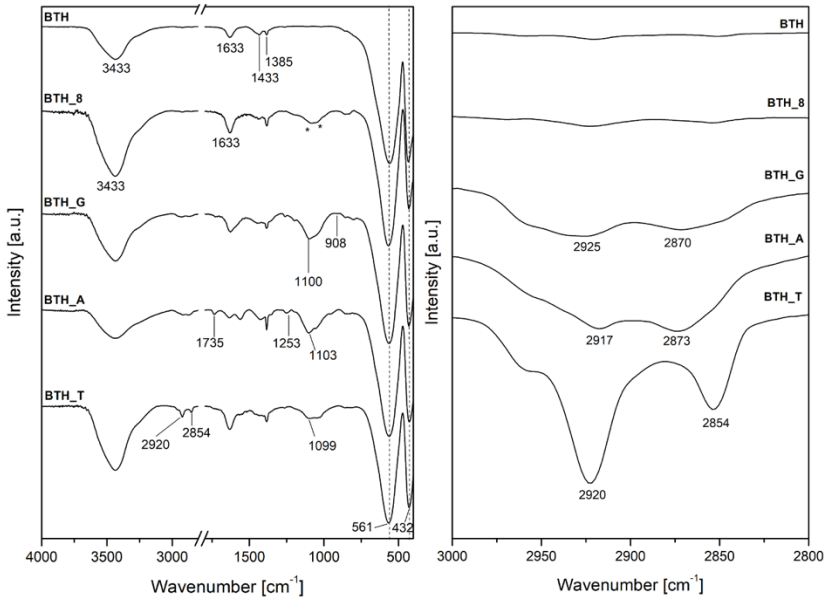

*Figure 36 FTIR spectra of bare BTH particles, hydroxylated BTH particles, and functionalized BTH particles, namely BTH_G, BTH_A, and BTH_T. On the right, magnification of FTIR spectra in the C-H stretching vibration range (2800 – 3000 cm^{-1}). Contamination by silicone grease (as confirmed by ^{29}Si NMR) is indicated by *.*

As for BTC particles, NMR analyses were carried out to characterize them in more detail particle functionalization. Figure 37 reports the ^{13}C CPMAS spectra of organosilanes (whose structure and carbon labeling is also reported in the figure) and BTH particles, respectively functionalized with 3-glycidyloxypropyltrimethoxysilane (G), 2-[acetoxy(polyethyleneoxy)propyl]triethoxysilane (A), and triethoxysilylpropoxy(polyethyleneoxy)dodecanoate (T). All the resonances of pristine organosilanes are effectively present in the related spectra of functionalized particles. Furthermore, comparing the BTH_G spectrum in Figure 37 with the NMR spectrum of BTC_G in Figure 34, they are very similar, but the relative intensities of the peaks suggest an improved functionalization in BTH particles with respect to BTC. More in detail, the signal-to-noise ratio (S/N) of BTH_A is lower with respect to BTH_G, this is probably ascribable to a lower amount of grafted silane. These considerations are also valid for BTH_T. The lower grafting degree of A and T with respect to G is probably due to the different reactivity of the silanes. A and T present much longer organic chains with respect to G, this results in steric hindrance and electronic inductive effects that can reduce the final amount of anchored silane. BTH_A spectrum also presents two resonances assigned to C=O at 183 and 169 ppm with an 82/18 ratio; this is probably due to diverse local environments that the carbonyl groups can encounter in folded or open chains. Concerning BTH_T signals of residual ethoxy groups are found at 60 and 15 ppm, suggesting incomplete hydrolysis of the organosilane. In addition to that, the lower degree of functionalization of BTH_A and BTH_T with respect to BTC_G (Figure 34) is confirmed by the ^{29}Si spectra reported in Figure 38. These spectra are also affected by a low S/N ratio, attributed to the low grafting degree. BTH_A and BTH_T samples present a broad resonance peak owed to the overlapping of T^2 and T^3 peaks, located respectively at -55 and -65 ppm. The T^2/T^3 ratio is 30/70, confirming a lower silane condensation degree with respect to BTH_G.

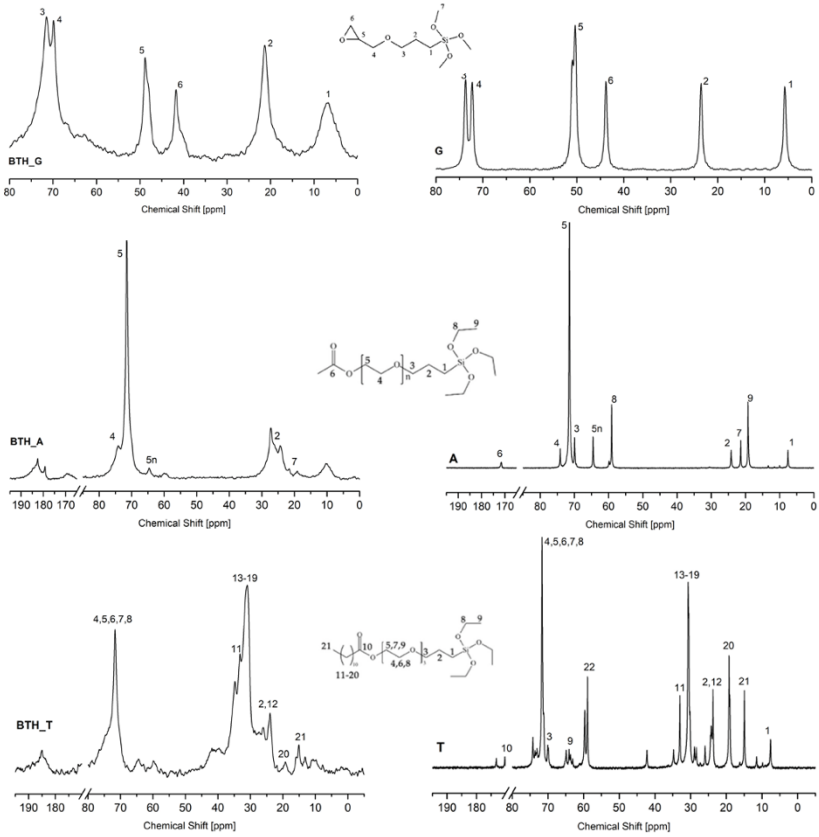

Figure 37 Left: [13]C CPMAS NMR spectra of BTH particles functionalized with GPTMS (BTH_G), APEOTES (BTH_A), and TESPEOD (BTH_T). Right [13]C NMR spectra of neat alkoxysilane (G, A, and T); the carbon labeling is shown in the schemes. [Adapted from [181] Zamperlin et al. Molecules 2022, 27(19), 6499]

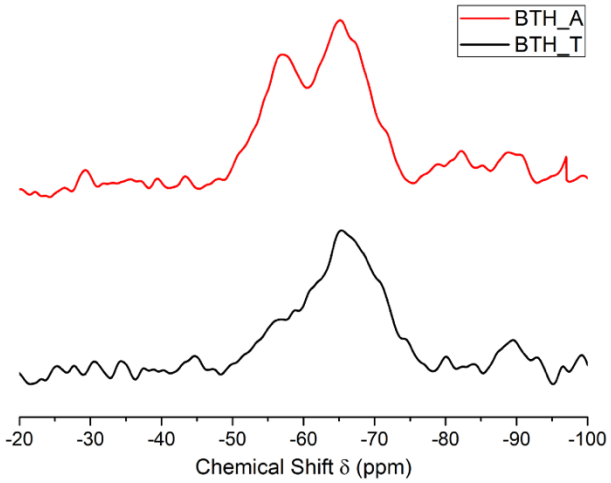

Figure 38 ^{29}Si NMR spectra of $BaTiO_3$ particles functionalized with TESPEOD (BTH_T) and APEOTES (BTH_A)

Finally, the grafting density was calculated from TG results, considering the weight loss in the region 300 – 600 °C, which was assigned to the silane decomposition. The weight losses were respectively 3.3 wt% for BTH_G, 3.0 wt% for BTH_A, and 2.5 wt% for BTH_T. The degree of functionalization σ, expressed as silane molecules per nm^2 of particles' surface, was calculated according to Maitra et al. [149] using the following equation:

$$\sigma = \frac{m_{sil} \cdot N_A}{MW} \cdot \frac{1}{mBTH \cdot SSA} = \frac{X_{wt}}{1 - X_{wt}} \cdot \frac{N_A}{MW \cdot SSA} \quad [molecules \cdot nm^{-2}]$$

where m_{sil} is the organosilane weight loss, N_A is the Avogadro number, MW is the silane's molecular weight, m_{BTH} is the powder mass, SSA is the specific surface area (calculated under the hypothesis of dense particles, using the geometric surface), and X_{wt} is the weight loss percentage. Accordingly, the resulting grafting densities were calculated respectively as 10.6 molecules·nm^{-2} for BTH_G, 3.5 molecules·nm^{-2} for BTH_A, and 3.2 molecules·nm^{-2} for BTH_T.

These results are congruent with the previous considerations on NMR results. It is worth noting that A and T organosilanes have longer organic chains and ethoxy groups are generally less reactive with respect to methoxy groups present in G [133]. The combination of alkoxy groups' nature, steric hindrance, and electronic effect may play a role in the reduced grafting degree of A and T. Despite these characteristics, the functionalization was successful in all cases and the grafting density is high, especially for GPTMS.

3.4 Nanocomposites

BTH particles present a higher surface density of organosilane molecules if compared with BTC particles, making hydrothermal particles much more attractive to produce nanocomposites. In accordance with that, PDMS- and epoxy-based nanocomposites were produced using both bare particles and particles functionalized with 3-glycidyloxypropyltrimethoxysilane (BTH_G) and 2-[acetoxy(polyethyleneoxy)propyl]triethoxysilane (BTH_A). Since we wanted to check the response of PEO units to the application of the electric field during nanocomposite production, the choice of using only BTH_A and not BTH_T was due to the slightly lower yield of functionalization and the shorter PEO segment in T chain with respect to A (3 repetitive units vs 7-8 PEO units). To evaluate the effect of functionalization on particles' dispersibility in the polymeric matrices, composites with bare and G-functionalized particles were produced with two different filler contents, low ≃15 wt%, and high ≃60 wt%, respectively 3.5 vol%, and 21 vol%. In the case of BTH_A powders, only the sample at 3.5 vol% was prepared. The samples were produced in the form of disks through a solution-casting process that involved both thermal curing and the application of an electric field. The PDMS composites showed greater flexibility (Figure 39), and a smoother appearance with fewer surface defects when compared to the epoxy-based composites. However, PDMS composites prepared with 21% loading of bare BTH presented defects, which on the contrary were not found in the corresponding sample prepared with BTH_G powders, proving the beneficial effect of particle functionalization on a macroscopic level. The addition of low amounts of nanoparticles did not have significant effects on the thermal properties of the polymer matrix, as demonstrated by DSC analyses of the composites, whose results are summarized in Table 8. PDMS samples exhibited T_g values ranging from -

120 to -125 °C, and low filler concentrations did not have a noteworthy impact on crystallization and melting enthalpies. However, at high filler concentrations, lower crystallization and melting enthalpies were observed. As for the epoxy-based samples, their glass transition temperature was generally in the range of 6-9 °C, except for E_21_BTH_G, which has a Tg of 26 °C. This can be attributed to the high loading of G-functionalized particles, which provided a large number of oxirane rings available for the ring-opening reaction, thereby increasing the cross-linking degree.

Table 8 Main thermal parameters from DSC analysis of polymer composites. [Adapted from [181] Zamperlin et al. Molecules 2022, 27(19), 6499, supplementary information]

Sample	T_g [°C]	T_m [°C]	ΔH_m [J/g]	T_{cc} [°C]	ΔH_{cc} [J/g]
E_neat	9				
E_3.5_BTH	6				
E_3.5_BTH_G	8				
E_21_BTH	8				
E_21_BTH_G	27				
P_neat	-125	-41	-28.24	-81	27.49
P_3.5_BTH	-120	-37	-23.66	-84	24.14
P_3.5_BTH_G	-124	-42	-23.52	-79	24.21
P_21_BTH	-125	-42	-11.12	-82	10.73
P_21_BTH_G	-127	-43	-13.67	-79	13.75

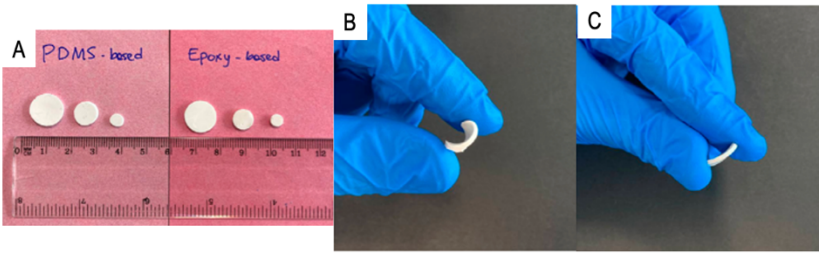

Figure 39 PDMS-based and Epoxy-based composites produced in different sizes in the form of thick disks (A); PDMS-sample (B) has higher flexibility than Epoxy-based (C). [Adapted from [181] Zamperlin et al. Molecules 2022, 27(19), 6499]

Figure 40 shows ATR-FTIR spectra of composites based on epoxy and PDMS, respectively. The FTIR spectra of epoxy-based composites are similar to that of cured epoxy resin, except for the Ti-O band due to the presence of barium titanate below 700 cm^{-1}, which becomes more prominent at higher filler content. In the composites, E_3.5_BTH_G and E_21_BTH_G, an additional peak at 916 cm^{-1} is observed, which is attributed to residual, unreacted epoxydic rings in the epoxy resin. This signal can be due both to unreacted epoxydic rings in the epoxy matrix or the GPTMS chain. A possible explanation could be linked to the reduced mobility resulting from the shorter length of the silane organic tail; when a GPTMS molecule is grafted onto the matrix, the matrix-particle system becomes more rigid, making it more difficult for nearby GPTMS organic chains to crosslink with the matrix. Another possibility is related to the simple introduction of the filler that hinders the chain motility of epoxy resin. The FTIR spectra of PDMS composites do not show significant differences compared to that of pure PDMS, except for the Ti-O band below 700 cm^{-1}.

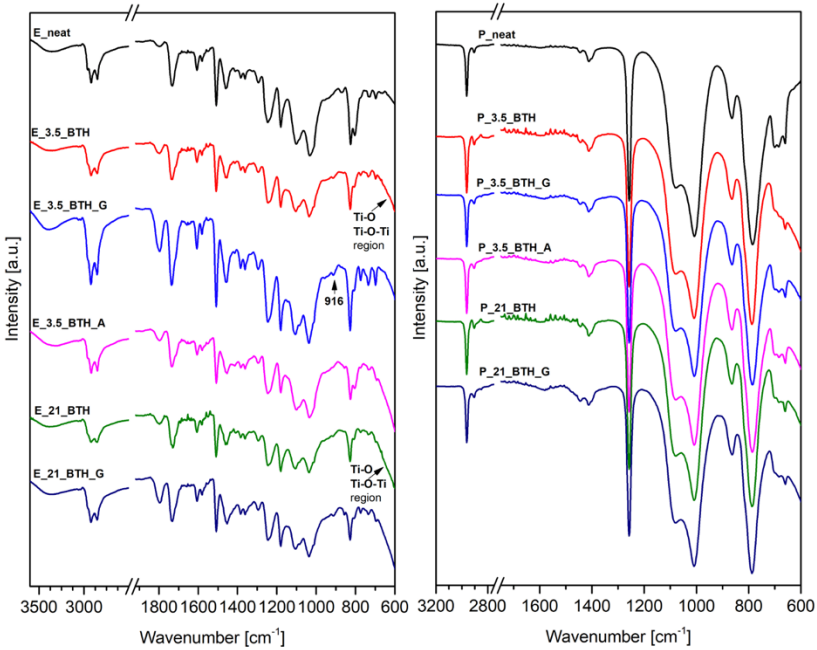

Figure 40 FTIR spectra in ATR mode of epoxy-based nanocomposites (on the left) and of PDMS-based nanocomposites (on the right).

3.4.1 Microstructural and EDXS Analyses

Figure 41 presents the SEM micrographs of epoxy composite disks with 21% filler content. Images highlight different particle-matrix interfaces for bare and functionalized particles. These images are cross-sections corresponding to sample regions between the electrodes that were subjected to a DC field. In the case of bare BTH, higher magnification (inset in Figure 41) highlights poor filler-matrix interaction with well-defined particles. In contrast, using BTH_G particles (Figure 41) leads to a more uniform and smoother surface, with particles embedded in the epoxy matrix, confirming the beneficial effect of functionalization on the polymer-$BaTiO_3$ interface. The corresponding composites at 3.5 vol.% filler content exhibit similar characteristics, and BTH_A particles behave similarly, improving the filler-matrix compatibility

of the epoxy composite at 3.5 vol.% loading (Figure 42). EDXS elemental maps of Ba were obtained on sections of epoxy composites loaded at 3.5 vol.% and subjected to the DC field to assess the dependence of particle dispersibility on organosilane functionalization (Figure 44). The composite with bare BTH NPs (Figure 44A) presents regions with particles aggregated in clusters and others with no fillers. The sample with G-Functionalized BTH particles (Figure 44B) shows that particles are finely distributed, with some slightly smaller clusters. By contrast, BTH functionalization with A silane (Figure 44C) results in a significant improvement in particle dispersion in the epoxy matrix. The better dispersibility of BTH_A compared to BTH_G is likely due to the different reactivity of the end-chain group of the two silanes, resulting in different strengths of the filler-matrix interface. With G, the epoxy ring at the end of the silane chain is expected to react with the epoxy matrix, while A-functionalized particles have less intense interaction with the matrix, leading to less hindered particles and improved dispersibility.

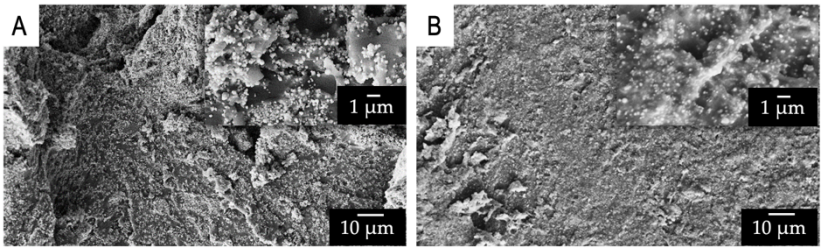

Figure 41 Cross-section images at 2000x (inbox 20'000x) of epoxy composites loaded at 21% filler content. Composites are loaded with pure BTH particles (A), and with BTH_G particles (B). [Adapted from [181] Zamperlin et al. Molecules 2022, 27(19), 6499]

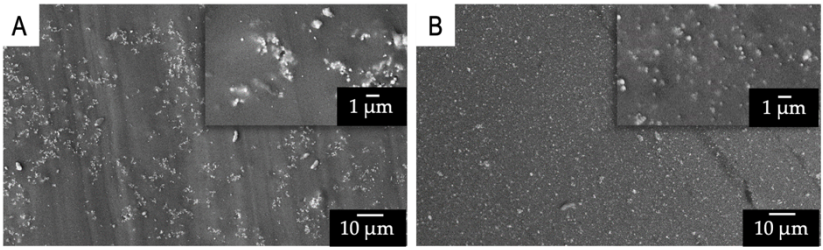

Figure 42 Cross-section images at 2000x (inbox 20'000x) of epoxy composites loaded at 3.5% filler content. Composites are loaded with pure BTH particles (A) and with BTH_G particles (B). [Adapted from [181] Zamperlin et al. Molecules 2022, 27(19), 6499]

SEM images of the cross-sections of PDMS composite disks display good filler-matrix compatibility without evident changes, independently from the employed particles. However, EDXS elemental maps of Ba reveal noticeable modifications, and in particular particle alignment due to the application of the DC field on composites produced with particles differing in surface modification (Figure 45). The alignment of barium titanate particles in polymeric matrices is known to depend on several factors, such as particle size, aspect ratio, applied field, etc. With bare BTH particles (Figure 45), large clusters and depletion regions are formed. At lower magnification, large clusters with partial segregation of particles at the bottom of the sample are also visible, with macro metric filaments extending vertically in the direction of the electric field and, in some cases, reaching the top face of the sample as shown in Figure 43.

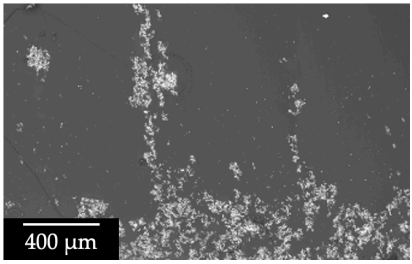

Figure 43 Low magnification (60x) SEM micrograph of PDMS composites loaded with BTH particles at 3.5 vol%. [From [181] Zamperlin et al. Molecules 2022, 27(19), 6499, supplementary information]

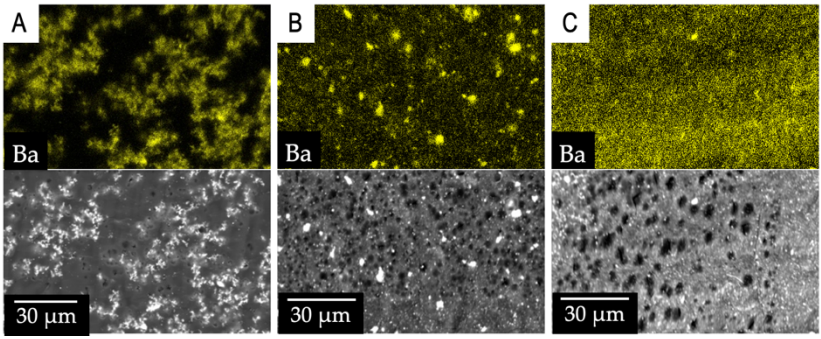

Figure 44 EDXS elemental maps of Ba and images of the reference areas of epoxy-based composites loaded at 3.5 vol% of filler respectively with BTH (A), BTH_G (B), and BTH_A (C). [Adapted from [181] Molecules 2022, 27(19), 6499]

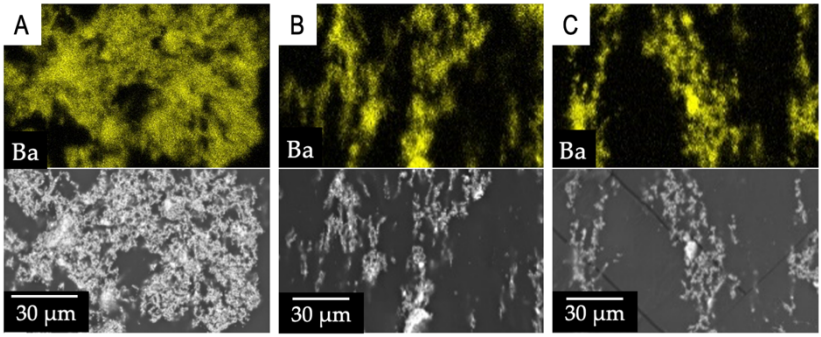

Figure 45 EDXS elemental maps of Ba and images of the reference areas of PDMS-based composites loaded at 3.5 vol% of filler respectively with BTH (A), BTH_G (B), and BTH_A (C). [Adapted from [181] Molecules 2022, 27(19), 6499]

This behavior is even more evident using particles functionalized with G silane, where filaments aligned along the direction of the applied electric field are observed, spanning a few tens of micrometers. Similarly, using BTH particles functionalized with the A silane yields results comparable to those of BTH_G particles. These findings demonstrate that surface modification

of the particles with G and A organosilanes significantly affects the distribution of BTH particles in both epoxy and PDMS composites. The homogeneity of particle distribution is enhanced by particles' functionalization in the epoxy matrix, with the A silane achieving the best results, while in the case of PDMS, surface modification allows increasing the filler content and leads to particle alignment in narrower filaments along the poling direction, avoiding the formation of large clusters and segregation of particles at the bottom of the sample, with no noticeable difference between the two silanes. Silane coupling agents' effect on $BaTiO_3$ NPs' alignment has received little attention in the literature, but Todd and Shi [183] suggested that these agents could play a crucial role in modifying molecular polarizability. Therefore, these results suggest that dispersibility and alignment depend on the chemical features of the particle-matrix interfaces. The functionalized particles and the final polymer-ceramic composites are subjected to a poling process, through the application of a DC dielectric field. The polar groups, as oxirane ring and PEO units in the functionalizing agents, are sensitive to the electric field and this could result in a tendency of the particles to align through the direction of the applied electric field, giving rise to some kind of anisotropy in the material; furthermore, the possibility of polarizing these groups can also lead to an increase of the dielectric properties of the final product, resulting in a final nanocomposite with superior dielectric and piezoelectric properties. The alignment of particles in PDMS is probably dependent on the intensity of particle-matrix interactions but could also be related to the lower viscosity of the starting liquid PDMS resin with respect to the epoxy resin; the lower viscosity could result in less hindered particles and a higher capacity to float in the liquid resin. It has been demonstrated the viscosity of a polymer-ceramic mixture depends on several factors such as the starting viscosity of the liquid polymer, the particle size, the volume fraction, and the size of particle aggregates [184]. However, further studies are needed in this sense. Anyway, the possibility of aligning fillers in the presence of a DC electric field has been reported in the literature for carbon nanotubes [67], but there are no studies, to the best of our knowledge, related to the use of such functionalizing agents and their effect on dielectric and piezoelectric properties in $BaTiO_3$ nanocomposites. Figure 46 shows the possible mechanisms of particle alignment under the application of a direct electric field.

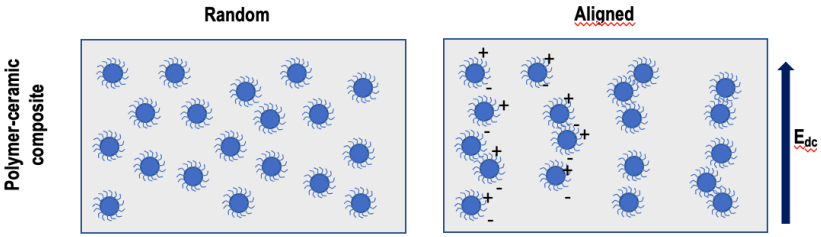

Figure 46 Possible mechanism for alignment of functionalized particles, functionalizing agents polarize under an electric field, pushing particles to align towards the direction of the applied electric field.

3.4.2 NMR Spectroscopy on PDMS Samples

The composites disks obtained through the dispersion of bare and G-functionalized BTH particles in PDMS display ^{1}H, ^{13}C, and ^{29}Si MAS NMR spectra dominated by the single resonance of PDMS, which is particularly sharp due to the elastomeric nature of the PDMS. Figure 47 shows the proton spectra of different samples with respect to PDMS characterized by the single resonance at about 0 ppm of the methyl groups of the skeleton. It is possible to notice small shifts and linewidth variations: the addition of functionalized hydrothermal nanoparticles both at 3.5% and 21% causes a small upfield shift, and the higher amount of NP also induces a broadening of the signal, probably due to increased rigidity of the system. Considering the EDXS maps that highlight the different NP distributions, the upfield shift of methyl resonance can be related to the changes in the chemical environment experienced by PDMS protons, the larger upfield shift being observed for the sample prepared with 3.5% of BTH_G.

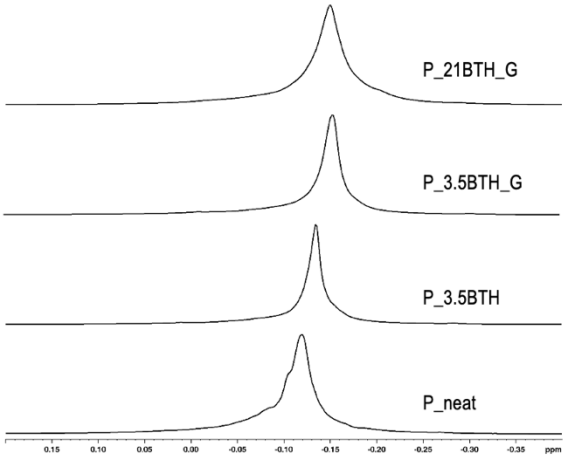

Figure 47 ^{1}H MAS NMR spectra of P_neat, P_3.5BTH and G-functionalized samples, P_3.5BTH_G and P_21BTH_G

^{13}C and ^{29}Si MAS NMR spectra, which are respectively dominated by the single resonance of methyl carbons and the signal due to D (SiC_2O_2) siloxane units of PDMS skeleton, appear superimposable for all the analyzed samples as expected, since the dispersion of NPs does not impact the chemical structure of the polymer and the relative amount of silanes grafted onto the particles is too low to be observable in the spectra (Figure 48 and Figure 49).

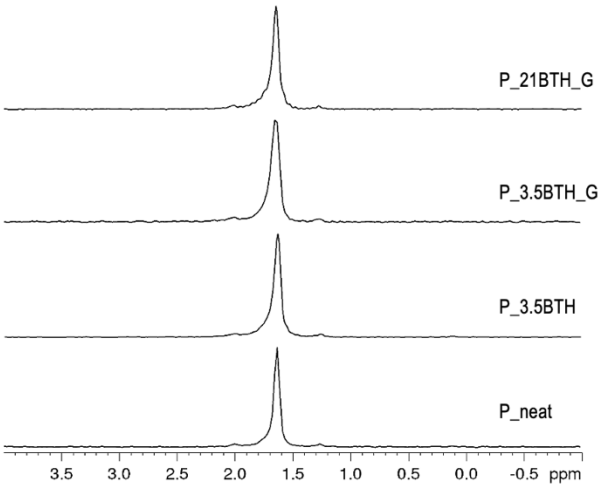

Figure 48 ^{13}C MAS NMR spectra of P_neat, P_3.5BTH and G-functionalized samples, P_3.5BTH_G and P_21BTH_G

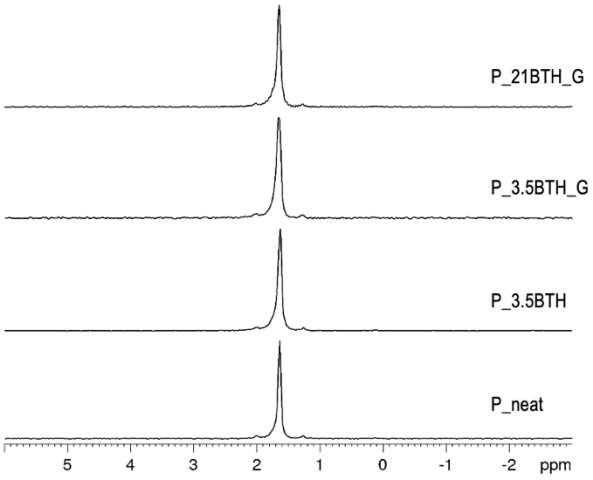

Figure 49 ^{29}Si MAS NMR spectra of P_neat, P_3.5BTH and G-functionalized samples, P_3.5BTH_G and P_21BTH_G

The features of PDMS suggest the feasibility of NMR molecular dynamics study in different dynamic ranges. Accordingly, the set-up for T_1, $T_{1\rho(H)}$, and T_2 relaxation parameters have been established [185,186]. Following the work of Garrido et al., [187] spin–lattice relaxation times (T_1), sensitive to the motion in the MHz range, were obtained through the inversion recovery pulse sequence, and spin–spin relaxation times (T_2) were obtained using the CPMG pulse sequence. Garrido studied elastomers reinforced with in situ precipitated silica, observing at room temperature T_1 values in the range of 1.19–1.26 s for PDMS samples loaded with 1.9–4.7 wt % silica, thus like the pure PDMS. The results on neat PDMS and composites are presented in Table 9. In the present work, all the relaxation data are successfully fitted with a single exponential and the found values are comparable, showing no clear difference among the samples, according to spin-diffusion averaging [188]. With the 21% load, the small T_{1H} value reduction (evidenced also in the measure of the carbon T_{1C}) could be ascribed to a reduced mobility, expected with a high load of inorganic filler addition [189]. To further investigate the dynamics of the systems, spin-spin relaxation (T_2) was evaluated, probing the segmental motion of the polymer chains on the picosecond time scale; these motions are usually affected by NP presence [190]. The data were successfully fitted with a single exponential decay speaking for low MW unentangled linear polymer network [191]. Again, only small variations among the values can be detected. As expected, the addition of the NPs causes a faster relaxation dependent on the dopant amount and related to the progressively reduced chain mobility.

Table 9 Chemical shift, linewidth, and relaxation parameters of PDMS composites

Sample	T_{1H} (±0.03s)	T_{1C} (±0.03s)	T_{2H} (±5 ms)
P_neat	1.26	2.39	230
P_3.5_BTH	1.26	-	218
P_3.5_BTH_G	1.34	-	219
P_21_BTH_G	1.12	2.24	207

Finally, the spin-lattice in the rotating frame $T_{1\rho H}$ has been also measured at different B1 field strengths. Like T_2, $T_{1\rho H}$ is related to slower motions typical of the dynamics of long chains and it is expected to highlight the possible impact on motion of the NP functionalization. The trends at different RF fields (B1) are shown for PDMS, as an example, in Figure 50. The data can be fitted with a single exponential decay in all cases except at the very low field, where at least two exponentials are necessary suggesting the presence of two different domains in the sample (for example, bulk and surface). All the analyzed samples behave similarly. The related decay constants $T_{1\rho H}$, which are directly dependent on the B1 value, are reported in Table 10.

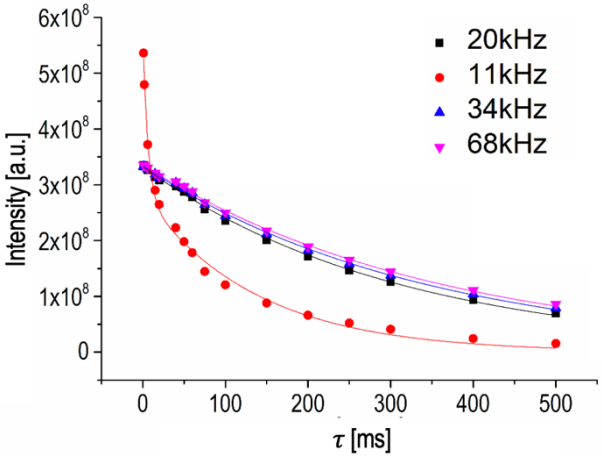

Figure 50 $T_{1\rho H}$ curves at different B1 for the representative PDMS neat sample. The trends of the other samples are similar. The Y-relative error for every point is below 0.05% (not visible). The relaxation constant $T_{1\rho H}$ obtained through the fitting with exponential curves with the relative errors are reported in Table 10.

Table 10 $T_{1\rho H}$ (ms) relaxation parameters of PDMS-composites

Sample	$T_{1\rho H}$ (±2ms) 11 kHz fast	$T_{1\rho H}$ (±15 ms) 11 kHz slow	$T_{1\rho H}$ (±9 ms) 20 kHz	$T_{1\rho H}$ (±9 ms) 34 kHz	$T_{1\rho H}$ (±9 ms) 68 kHz
P_neat	6	137	309	340	358
P_3.5_BTH	4	120	306	337	349
P_3.5_BTH_G	5	130	304	337	358
P_21_BTH_G	5	131	285	319	338

The relaxation data are directly field dependent as expected. It can be noticed that at every B1 value, the 3.5% NP load does not affect PDMS dynamics independently from the functionalization, whereas a small reduction of the $T_{1\rho H}$ can be seen with a 21% NP load.
In conclusion, the nanocomposites are obtained by dispersing $BaTiO_3$ NP at different loads, with and without functionalization in a non-reactive elastomeric matrix. Accordingly, the NMR data point out a certain sensitivity of the protons, since they are exposed to the different environments created by the NP dispersion with respect to the PDMS chain, but no other structural effects can be detected due to the intrinsic inertness of the matrix. Moreover, the study of NMR dynamics at the molecular level confirms the average insensitivity of the PDMS, revealing just a minor effect of filler concentration that induces a reorganization of the polymer chains around the NPs.

In conclusion of section A, the main achievements in the synthesis and functionalization of ceramic fillers and the production of nanocomposites can be summarized:

- highly homogeneous $BaTiO_3$ NPs with controlled aspect ratio and narrow size distribution (average size 117±27 nm) were synthesized via wet chemical synthesis after optimization of process parameters, such as the hydrothermal reaction time.
- the produced NPs have good values of tetragonality (c/a=1.0074) in comparison with particles prepared through the traditional but more energy-demanding solid-state route (c/a=1.0100).

- NPs were successfully surface-functionalized with different organosilanes, namely 3-glycidyloxypropyltrimethoxysilane, 2-[acetoxy(polyethyleneoxy)propyl]triethoxy silane and (triethoxysilyl-propoxy(polyethyleneoxy)dodecanoate; a high degree of grafting was calculated for all the samples, the highest value (10.6 molecules·nm^{-2}) was found for NPs functionalized with GPTMS.
- flexible nanocomposites were produced by embedding bare and functionalized nanoparticles both in epoxy resin and PDMS; filler loadings up to 21% vol. were achieved, and the presence of functionalizing agents resulted in higher particle dispersibility and improved processability of composites; interestingly, the thermal curing cycle with the combined application of heat and electric field led to particle alignment along the direction of the applied electric field in PDMS composites.

Part B) Electric, Dielectric, and Piezoelectric Characterization of Nanocomposites

3.5 Piezoelectric Behavior

The piezoelectric coefficient d_{33} of bulk disk nanocomposites was measured with a Belincourt-type piezo-d_{33}-meter. The samples are placed between the two testing electrodes, clamped with 8-9 N force, and subjected to a 0.25 N force oscillating at a fixed frequency of 110 Hz. Results are summarized in Table 11.

Table 11 Values of piezoelectric coefficients (d_{33}) for epoxy and PDMS bulk composites (thick disks)

Sample (Epoxy)	d_{33} [pC/N]	Sample (PDMS)	d_{33} [pC/N]
E_neat	2.7 ± 0.1	**P_neat**	9.8 ± 4.6
E_3.5_BTH	2.8 ± 0.1	P_3.5_BTH	9.8 ± 0.1
E_3.5_BTH_G	2.8 ± 0.1	P_3.5_BTH_G	9.7 ± 0.2
E_3.5_BTH_A	2.8 ± 0.2	P_3.5_BTH_A	9.9 ± 0.2
E_21_BTH	3.0 ± 0.3	P_21_BTH	10.0 ± 0.3
E_21_BTH_G	2.9 ± 0.1	P_21_BTH_G	9.9 ± 0.1

The values of d_{33} show little variation between neat epoxy and composites. The same occurs for PDMS-based nanocomposites. Since the piezoelectric behavior of nanoparticles synthesized in this work was assessed (piezoelectric measures on pellets produced with $BaTiO_3$ nanoparticles gave d_{33} constants values up to 85 pC/N), there are different possible explanations related to the filler content [192,193] and an inhomogeneous electric field inside the material during the curing/poling procedure, since the simultaneous presence of particles, agglomerates, and interfaces could interfere with the applied electric field [20]. In addition, the reason for these data could be attributed to the fact that the load is carried by the polymeric matrix. The piezo-active part in the composite material is the ceramic filler, if the particles are not stressed when compressive stress is applied no piezoelectric effect will be exploited. In this case, given the available experimental setup, probably the compressive stress is not transferred from the polymeric matrix to the particles resulting in a non-detectable piezoelectric effect.

3.6 Dielectric/Electric Characterization of PDMS-films

In consideration of the impossibility of obtaining reliable measurements of the piezoelectric properties, the project focused on PDMS as a matrix, and PDMS films loaded at 3.5 and 14 vol.% with bare and functionalized particles were produced to explore their potential for energy harvesting application as dielectric elastomer generator (DEG). In this sense, as explained in the introduction, the evaluation of the dielectric constant and dielectric breakdown is very important to understand the potential energy-storage performances of the composites. To accomplish this objective, Dielectric Spectroscopy (DS) and electric breakdown measurements were done on PDMS films.

3.6.1 Dielectric Spectroscopy

All PDMS-based samples underwent DS measurements, which involve the analysis of dielectric properties in relation to frequency and temperature. Measurements were collected at different frequencies and temperatures, under the experimental conditions reported in paragraph 2.6.2. These studies focused on the evaluation of permittivity (real and imaginary parts), conductivity, and tangent delta with the aim of highlighting their dependence on the activation of different polarization mechanisms.

Permittivity

Figure 51a shows the real part of the dielectric constant of PDMS film composites.

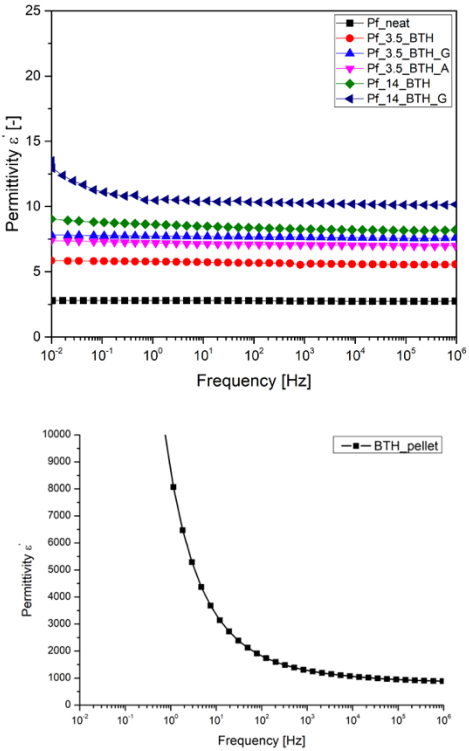

Figure 51 Top: Real part of the permittivity for PDMS-based films as a function of the frequency (range 10^{-2} to 10^{6} Hz); Bottom: Real part of the permittivity for BTH powders pellet (the calculated error on the measures is < 5%).

The permittivity value of the neat PDMS matrix is 2.7, which is consistent with the value reported on the technical datasheet, while the BTH powders have a value of permittivity of about 1000 (Figure 51b). The BTH pellet's permittivity curve (Figure 51b) is dominated by interfacial polarization due to the high number of particle-particle interfaces. The addition of BTH powders to PDMS increases the permittivity, especially at low frequencies and, as expected, the magnitude of this effect depends on the amount of filler [128,194]. As reported in the literature, the dielectric properties of the ceramic fillers are dependent on different factors such as grain size

and other microstructural features [195,196]. The increase in the base value of the dielectric constant is not linear with the quantity of the ceramic filler, a large filler content results in more particle-particle interactions and the formation of aggregates but induces more polarized matrix-filler interfaces with higher permittivity values at low frequencies (<10^2 Hz) [163,197]. For the same filler's amount, the particles' surface functionalization produces a further increase in permittivity [128,198], because functionalization activates polarization mechanisms. The phenomenon seems independent of the nature of the organosilane. In fact, films prepared with 3.5% of BTH_G and BTH_A do not show relevant differences in permittivity.

The permittivity increase, more pronounced at lower frequency values and in samples with functionalized particles, is likely due to a combination of interfacial and dipole polarization. Filler functionalization leads to higher particle dispersibility resulting in more homogeneous samples and higher dielectric constants of the nanocomposites. Furthermore, the improvement of matrix-filler interfaces through the organosilanes leads to the activation of dipolar polarization due to the presence of polar groups in the molecular chain and the enhancement of Maxwell-Wagner-Sillars (MWS) interfacial interaction at the particle-matrix interface because of interfacial polarization phenomenon.

The impact of temperature on the dielectric constant has also been examined, revealing distinct trends in the permittivity frequency sweeps at different temperatures; Figure 52 shows DS frequency sweeps of the real part of permittivity of all samples at different temperatures, ranging from -140 °C to 120 °C. For pure PDMS, it is amorphous above about -40 °C, its glass transition temperature is about -127 °C, and a cold crystallization is found around -90 °C depending on the experimental conditions and the type of PDMS. An increase in temperature results in a slight decrease in permittivity value. This trend is usual for apolar materials that follow the Langevin theory. At high temperatures, the low-frequency polarization phenomena become more prominent and begin at higher frequencies. When particles are added, the permittivity decreases with frequency, as polarization levels out and dipoles fail to keep up with the rapid alternation of the field. This effect is more pronounced at higher temperatures, perhaps due to thermal excitation. At lower filler content, particle-particle interactions seem to be overlooked compared to particle-macromolecule interaction [199]. Lastly, the sharp increase at low frequency and high temperatures of the A and G-functionalized samples may be attributed to other

phenomena linked to the functionalizing agent's molecular structure, as the presence of conductive PEO units combined with high temperatures may result in some conduction mechanisms.

In Figure 53, the temperature-dependent imaginary part is shown for all samples, while Figure 54 displays the tangent delta of the same samples. These two parameters, the imaginary part of the permittivity and tan(δ), are indicative of energy losses. The higher the values of these parameters, the greater the dielectric losses in the polarization process. Since the real part of the permittivity (shown in Figure 52) remains nearly constant, the trends of Figures 53 and 54 are very similar.

For all samples, tan(δ) has low values (<0.01) from 10^6 Hz down to 10^2 Hz. The strong increase of tanδ with the lowering of the frequency is the consequence of the ac conductivity of the electric charges at long distances which settles in the material. Mathematically, this conductivity is an imaginary term that is added to the dielectric losses. When this conductivity becomes preponderant compared to the dielectric losses, one sees only the effect of this conductivity, which is the case here in the low frequencies, and which is accentuated by the increase in temperature. When the filler concentration is low, the functionalization appears to be beneficial for both tan(delta) and dielectric loss, probably due to the stronger particle-matrix interface.

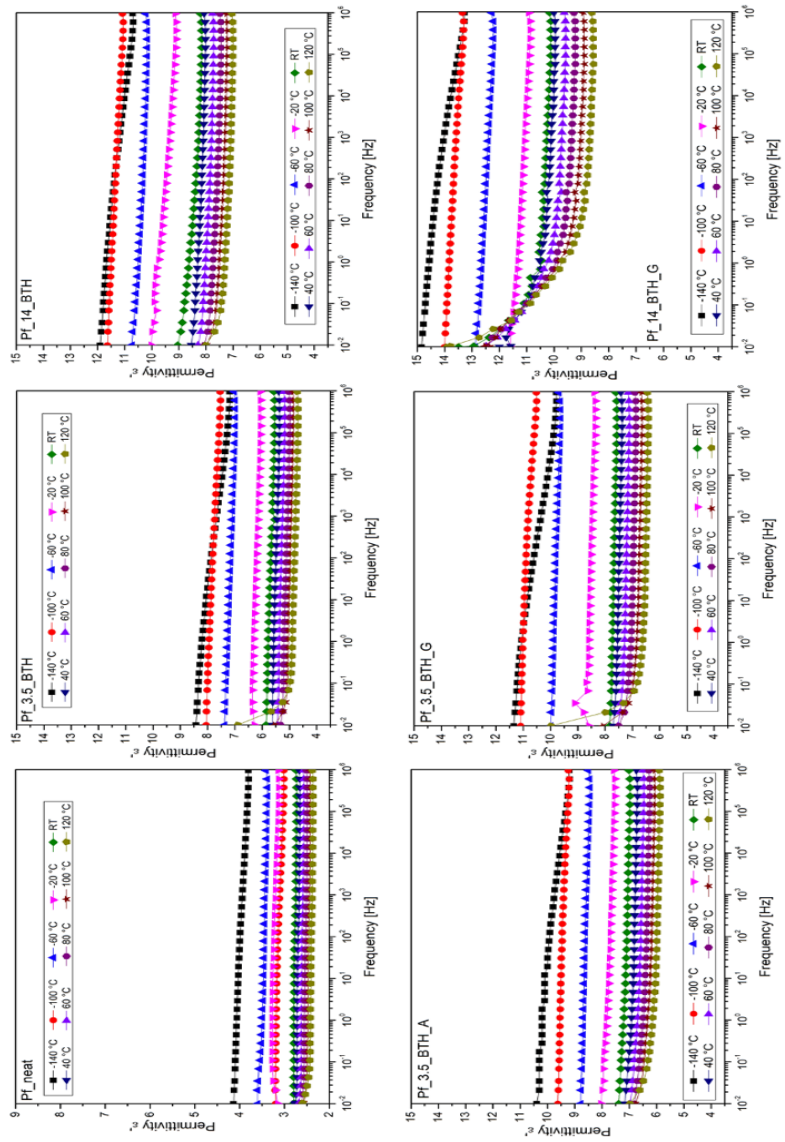

Figure 52 Frequency sweeps (from 10^{-2} to 10^{6} Hz) of the real part of permittivity of all PDMS-based composites at different temperatures (from -140 °C to 120 °C)

However, at higher filler concentrations, the tan(δ) is higher at lower frequencies. This can be attributed to the formation of clusters and particle aggregates, which act as inhomogeneities and result in higher losses. An increase in conductivity within these clusters cannot be excluded and could contribute to this increase in losses. At low temperatures, the dielectric loss is minimal and remains on the order of magnitude of 10^{-2}. As temperature increases, dielectric loss also increases, which is correlated to higher thermal excitation. Conversely, as the temperature decreases to -60 and -100 °C, the dielectric loss begins to decline. As mentioned above, below -40 °C, PDMS becomes semi-crystalline and the movement of polymer chains is thus reduced due to the crystallization of certain polymer chains: less chain mobility thus leads to lower losses, which is consistent with the results. It is noteworthy that the loss tangent at -140 °C is consistently higher at high frequencies relative to the base value.

The trend of tan(δ) is influenced by the polymeric matrix, as different relaxation mechanisms can be activated at various temperatures and frequencies. At very low temperatures, the increase in dielectric loss (or tan(δ)) for the neat matrix at low frequency is due to α-relaxation mechanisms (polymeric chain re-arrangement), while at higher temperatures, the effect of other phenomena like MWS and β-relaxation are observed. As the temperature rises to and overcomes the Tg, the molecular chains exhibit swift movement and orientation, resulting in the visible manifestation of the relaxation process in the dielectric spectrum. For the material to experience dielectric loss ε", the orientation of the dipole chain segments in the direction of the applied electric field must overcome inertia and rotational resistance [200]. The addition of fillers tends to slightly reduce the overall loss factor, and the effect of low-frequency polarization appears at higher frequencies compared to the neat matrix. This phenomenon becomes more evident with increasing temperature [201]. Furthermore, particle functionalization also plays a role. The effects of MWS (interfacial interaction) become more apparent and begin at much higher frequencies compared to bare particles. This could suggest concurrent dipolar polarization, as functionalizing agents have polar groups in their molecular structure. However, the dielectric loss tangent at room temperature is quite low for all composites, indicating that most of the electric energy can be converted into mechanical energy with minimal energy dissipation.

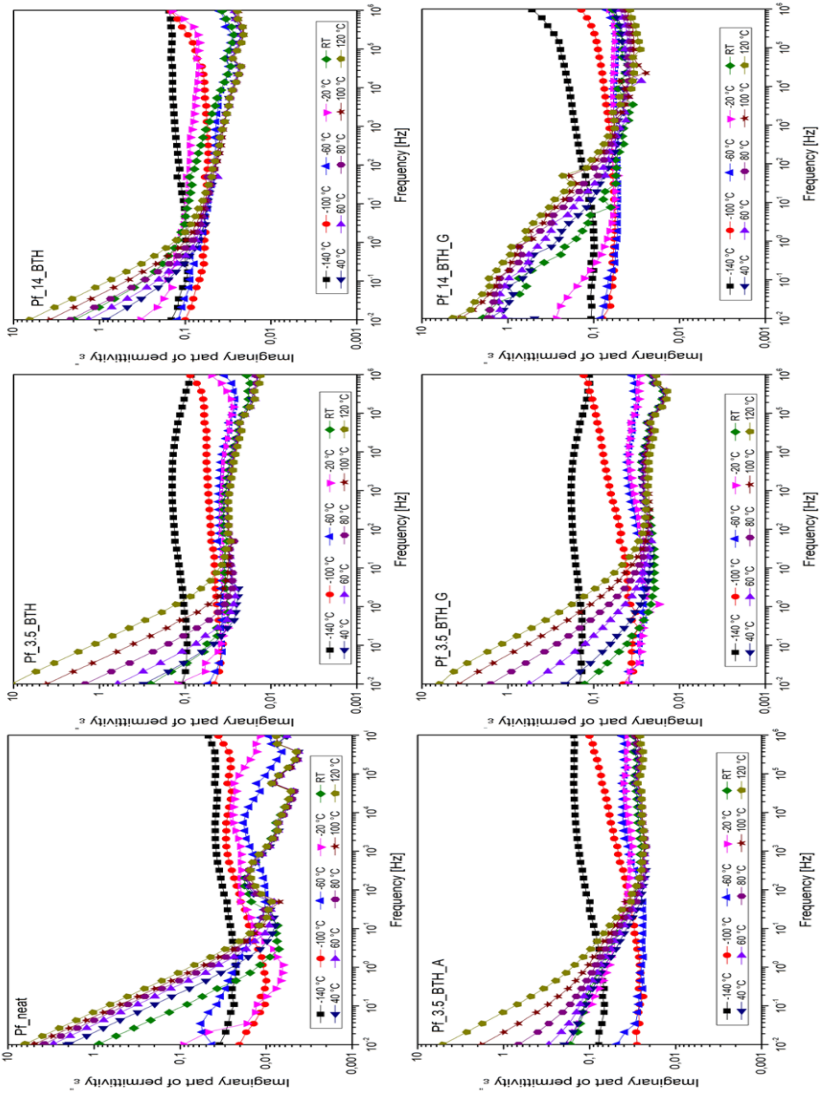

Figure 53 Frequency sweeps (from 10^{-2} to 10^{6} Hz) of the imaginary part of permittivity of all PDMS-based composites at different temperatures (from -140 °C to 120 °C).

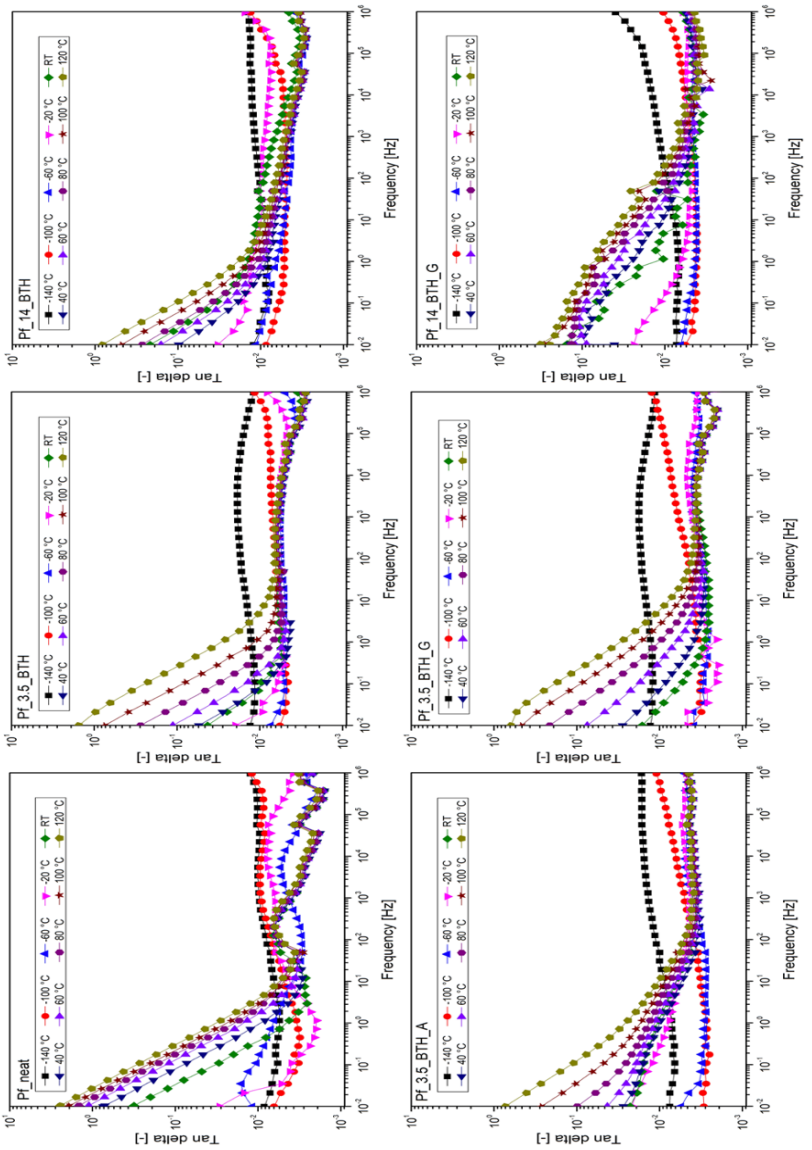

Figure 54 Frequency sweeps (from 10^{-2} to 10^{6} Hz) of the tan delta of all PDMS-based composites at different temperatures (from -140 °C to 120 °C).

Conductivity

Conductivity trends of composites were extrapolated from DS measurements. All the composites display insulating properties according to conductivity measurements. Figure 55 illustrates the conductivity trends for all samples as a function of frequency and temperature. The observed behavior is similar to the universal Jonscher law: $\sigma_{ac}(\omega) = \sigma_{dc} + A\omega^n$, Where σ_{ac} is the conductivity in ac regime, σ_{dc} is the direct current conductivity, and $A\omega^n$ is the dispersive component of ac conductivity, directly related to the frequency ω and an exponent n ($0 \leq n \leq 1$). The conductivity exhibits a nearly linear behavior (on a log-log scale) ranging from 10^{-8} to 10^{-14} – 10^{-15} S/cm by going from high (10^6 Hz) to low frequencies (10^{-2} Hz). Accordingly, an AC-conductivity regime specific to short-range bound charges is shown. At low frequencies, a frequency-independent plateau is observed for almost all samples. Nanocomposites conductivity is strongly affected by frequency and temperature, as the samples are insulating in nature: at very low frequencies, the conductivity values decrease as the frequency decreases in consequence of dipole polarization or Maxwell-Wagner-Sillars (MWS) interfacial polarization [202]. This is confirmed by the fact that neat PDMS displays a marked plateau region at low frequencies (<10^0 Hz), especially by increasing the temperature. The plateau region is less evident by increasing the filler content due to interfacial polarization as explained before and it almost disappears when the particles are functionalized. Conductivity is influenced by temperature: at higher temperatures, below 10 Hz, the conductivity presents a plateau, indicating a DC-conductivity component specific to long-range moving charges [201], and this effect is more pronounced in Pf_neat [201]. These changes correspond to the thermally activated character of the AC conductivity and the increase of the DC bulk conductivity [203]. This is likely associated with the increased mobility of organic modifier chains at higher temperatures [204]. At lower temperatures, long-range movement is suppressed due to lower charge mobility, and the linear trend is maintained with no DC plateau. The presence of the filler also plays a role. The conductivity of PDMS/BTH composites increases as the frequency increases for all filler concentrations. The small increase in the room temperature conductivity can be linked to the introduction of ceramic fillers: at 1 kHz the conductivity value is $5.2 \cdot 10^{-12}$ S/cm for Pf_neat and increases to $6.6 \cdot 10^{-11}$ S/cm and $2.6 \cdot 10^{-11}$ S/cm respectively for Pf_3.5_BTH and Pf_14_BTH.

When the filler concentration increases, the interfacial polarization also increases, leading to an increase in conductivity that may be caused by ion hopping in the polymer chain [205]. However, despite the higher conductivity of the filler (ranging from 10^{-3} (at 10^{6} Hz) to 10^{-9} S/cm (at 10^{-2})) with respect to the neat matrix, the addition of the filler does not significantly affect the final values of the conductivity. The presence of functionalizing agents has also an effect on the conductivity, this is probably due to the enhanced interfacial polarization phenomena, considering that MWS polarization is caused by local changes in conductivity across internal interfaces and charge accumulation at the boundaries between components with different conductivity [201]. The presence of organosilanes at the interface between the matrix and the particles can be responsible for charge accumulation. The RT conductivity at 1 kHz of functionalized samples (Pf_3.5_BTH_G and A) is around $1.2 \cdot 10^{-11}$ S/cm which is almost 6 times higher than Pf_3.5_BTH. Furthermore, with the polar functionalizing agents a shoulder is observed rather than a plateau with an onset of around 10 Hz.

This is particularly evident in the Pf_14_BTH_G sample, confirming previous findings at RT analyses. The effect becomes more pronounced with increasing temperature and is more evident with APEOPTES. The greater effect of APEOPTES may be due to its molecular structure, as the conductive PEO units can behave as longer-range charge carriers. When the plateau region is enlarged to higher frequencies, the mobility of long-range charge carriers is enhanced. The outside APEOPTES shell layer (containing conductive PEO segments) can improve the connection of functionalized particle clusters and form a more conductive path through-going the filler network. A similar behavior was reported by Guan et al. [206] using carbon nanotubes functionalized BT particles in a PDMS matrix. In conclusion, the presence of both ceramic fillers and functionalizing agents influences the conductivity behavior of the composites, offering further hints on the activation of different polarization mechanisms.

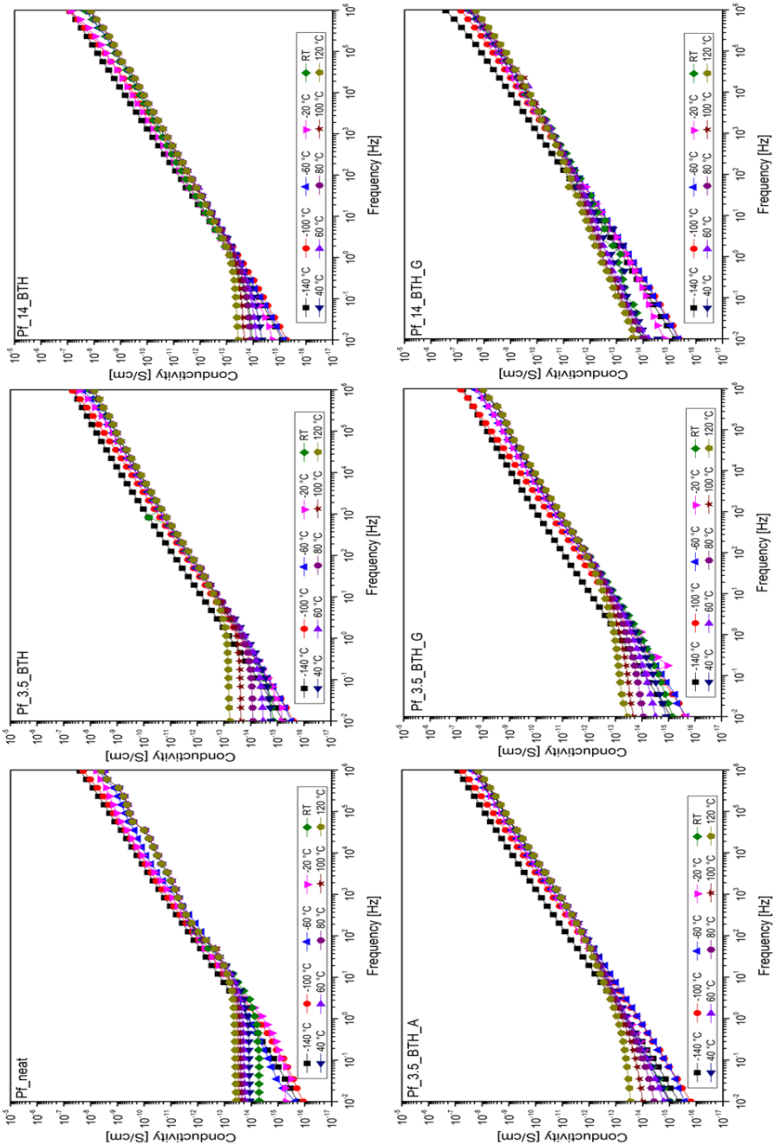

Figure 55 Frequency sweeps (from 10^{-2} to 10^{6} Hz) of the conductivity value for all PDMS-based composites at different temperatures (from -140 °C to 120 °C).

3.6.2 Electric Breakdown

The breakdown voltage of the PDMS-based composites was measured, and the results are presented in Table 12. The composites exhibit a dielectric breakdown voltage between 33 and 42 kV/mm. The dielectric breakdown of the neat PDMS was found to be 33.8 ± 5.4 kV. At low-filler loading (3.5%), a slight increase in the dielectric breakdown is observed for bare particles, while the functionalization of particles appears to have a very positive impact on the breakdown. The beneficial effect of the functionalization on the breakdown strength can be discussed in terms of a) better particle dispersibility of fillers, resulting in more homogenous composites with fewer defects and voids; b) the presence of a functionalizing agent that could impede leakage current of composites [207]; c) polar groups and conductive paths present in the G and A functionalized samples, which act as charge traps, storing electric charges before the breakdown region [208–210]. However, the situation is different for samples at high loading (14 vol%) which display an average value of the breakdown voltage almost similar to that of neat PDMS. This lack of improvement may be attributed to the lower homogeneity of highly loaded samples, as they contain some large particle agglomerates that act as defects and inhomogeneities in the samples, reducing the beneficial effect of particle addition. This large amount of filler (14 vol%) also favors conduction paths due to the high probability of interconnection among the particles.

Table 12 Values of dielectric breakdown for PDMS-based composite films with their relative standard deviation and the percentage difference with respect to the neat matrix.

Sample	E_{BD} [kV/mm]	Std. Dev.	Δ(neat)
Pf_neat	33.8	5.4	-
Pf_3.5_BTH	34.6	6.1	+ 2.4 %
Pf_3.5_BTH_G	39.9	6.9	+ 18.0 %
Pf_3.5_BTH_A	42.1	6.8	+24.5 %
Pf_14_BTH	33.0	5.2	-2.4 %
Pf_14_BTH_G	34.8	5.0	+2.9 %

3.6.3 Stretching

With the idea of exploring the possible use of these composites as dielectric elastomer generators the dielectric constant and the dielectric breakdown of the composites were evaluated in a deformed state. Samples have been stretched slowly and manually with a simple homemade apparatus reported in Figure 56. The PDMS films were cut into slices (50 mm length, 10 mm width) and put on paper frames (as in the tensile test for polymeric fibers). The frames were then clamped on the slit and stretched to $\lambda = 2$ (the initial length was doubled). The central part of the stretched samples was then blocked on epoxy rigid substrates covered by a copper layer that should act as the bottom electrode while a gold electrode was sputtered on the top as shown in the inset of Figure 56. With this configuration, both dielectric spectroscopy and dielectric breakdown measurements were carried out to evaluate the effect of stretching on the samples.

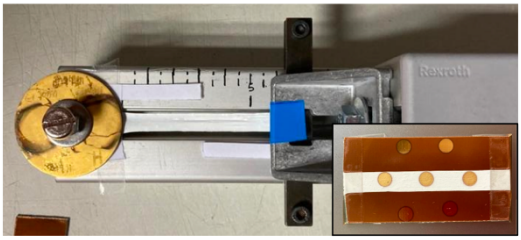

Figure 56 Home-made apparatus for uniaxial deformation of the samples; the inset shows the substrate on which deformed samples were clamped and used for dielectric spectroscopy measurements and dielectric breakdown evaluation.

It is worth noting that this configuration does not foresee the presence of an interface medium material (no Au-sputtered electrode) between the bottom electrode and the material. Samples were placed carefully on the copper layer ensuring good adhesion and trying to remove or reduce as much as possible air trapping. However, it should be considered that some air bubbles might be present at the interface between the electrode and the dielectric material, and this could have some effects on dielectric spectroscopy measurements and dielectric breakdown evaluation. As for dielectric spectroscopy, air trapping [211], together with surface

inhomogeneities [212], could be responsible for higher dielectric losses and dampened spectrum that could lead to underestimation of the electromechanical coupling factor. Additionally, the eventual presence of a thin layer of trapped air could be responsible for an underestimation of the permittivity; in fact, the system could be seen as two capacitors in series (dielectric + air), with a permittivity that is an average of the values of the permittivity of the dielectric and air weighted with respect to the relative thickness of the layers. Anyway, by ensuring a good contact between the material and the bottom electrode the eventual thickness layer of the air should be minimized with respect to the material, resulting in an almost negligible effect. About the dielectric breakdown, it is worth noting that the eventual presence of air trapped between the electrode and the dielectric material could result in early failure, but this risk can be minimized by ensuring good adhesion of the films to the bottom electrode. However, these limitations should result in an eventual underestimation of both permittivity and dielectric breakdown, and, consequently, of the theoretical energy density, meaning that real energy harvesting performance is probably higher, accordingly, this is a conservative approach.

Dielectric Spectroscopy

Figure 57 shows the real part of the permittivity of stretched samples plotted against the frequency. Stretching affects the value of the dielectric constant. All the samples, except the neat PDMS matrix, show a decrease in the dielectric constant once subjected to a stretching ratio $\lambda = 2$. This phenomenon is also reported in the literature [213–215]. However, it is interesting to note that samples prepared with non-functionalized particles at low and high loading (3.5 and 14%, red and green curve in Figure 57) have practically the same values of the dielectric constant. Functionalization helps to keep the permittivity dependent on the loading, but values found for composites prepared with functionalized particles are more or less half of the value of unstretched samples. In the specific, the decrease in the dielectric constant is less evident in the A-functionalized sample. The reasons for the dependence of dielectric permittivity on the deformation can be different but are mainly related to [213]:

- Presence of dipoles in the polymeric chain that can be subjected to orientation/reorientation [215].

- Strain crystallization mechanisms due to the deformation process.
- Effects of local constraints (such as particles and/or fillers) in the bulk and/or at the interface level that can affect the final permittivity [214].

The absence of a decrease in the permittivity of the neat matrix strengthens the consideration of local effects related to interfaces. However, the effect of stretching on the dielectric constant is still largely misunderstood or even not considered and seems to be strongly dependent on the experimental protocol: different results can be obtained depending on stretching ratio, initial/final thickness, electrode type, or measurement technique [214].

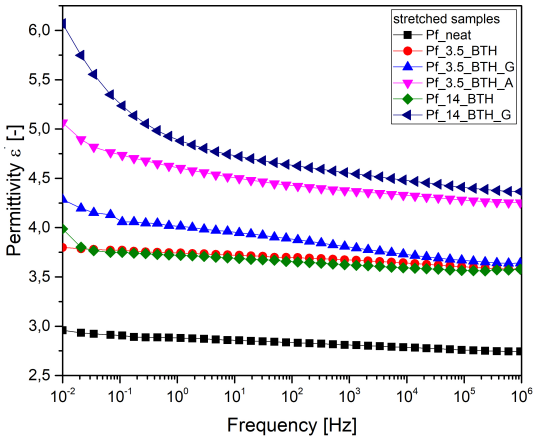

Figure 57 Real part of the permittivity for PDMS-based films in the function of the frequency (range 10^{-2} to 10^{6} Hz).

Figure 58 shows the RT behavior of the conductivity of stretched (Figure 58A) and unstretched samples (Figure 58B). The conductive behavior of stretched samples is quite similar to that of unstretched samples, with a few differences observed in Pf_3.5_BTH_G and Pf_3.5_BTH_A. Specifically, these samples exhibit conductivity values at low frequencies higher by two orders of magnitude in their deformed state (10^{-13} vs 10^{-15}) and present a plateau from 10^{0} Hz. The increased conductivity in the stretched G and A-functionalized samples could be due to the re-

orientation of the polar polymeric chain of the functionalizing agent, which creates a conducting path and leads to an increase in charge carrier concentration [216]. In contrast, this behavior is not observed in Pf_14_BTH_G, possibly due to damage to the local contact in the polymer composite structure and a resulting decrease in the conductive pathway [217,218].

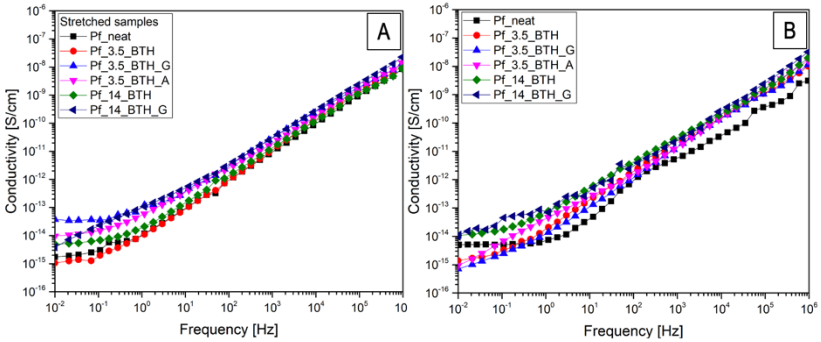

Figure 58 Conductivity trend for PDMS-based films in the function of the frequency (range 10^{-2} to 10^{6} Hz) of stretched samples (A), and in the undeformed state (B).

Dielectric Breakdown

The breakdown voltage of the PDMS-based composites after stretching was measured, and the results are presented in Table 13.

Table 13 Values of dielectric breakdown for deformed PDMS-based composite films with their relative standard deviation and the percentage difference with respect to the neat matrix and with respect to their undeformed state.

Sample (stretch λ =2)	E_{BD} [kV/mm]	Std. Dev.	Δ(neat)	Δ(stretch/unstretch)
Pf_neat	34.2	3.5	-	+ 1.2 %
Pf_3.5_BTH	40.7	7.4	+ 18.0 %	+ 17.6%
Pf_3.5_BTH_G	44.8	9.4	+ 31.0 %	+ 12.3 %
Pf_3.5_BTH_A	44.8	7.8	+ 31.0 %	+ 6.4%
Pf_14_BTH	34.0	4.0	- 0.5 %	- 0.6 %
Pf_14_BTH_G	45.5	5.5	+ 33.0 %	+ 30.7 %

The stretching of the composite films results in an increase in dielectric breakdown strength at different intensities depending on the filler content and the possible functionalization. This effect is also reported in the literature, and it is probably related to the stiffening of the elastomeric material [213]. The higher the stretching ratio the stiffer the polymeric matrix and, consequently, the breakdown strength. The value of the stretched neat PDMS is 34.2 kV/mm (± 3.5) and it is very close to the value of the undeformed neat PDMS. The situation for low-loaded samples (3.5 vol%) is the following. All the low-loaded samples present higher values of dielectric breakdown with respect to their undeformed state with a relative increase from 6.4 to 17.6% depending on the sample. For highly loaded samples (14 vol%) the situation presents two opposite situations. The E_{BD} value for strained Pf_14_BTH remains basically unchanged with respect to its un-deformed counterpart (34.0 kV/mm vs 33.0 kV/mm). This is mainly due to the fact that the beneficial effect of the stiffening of the membrane is counterbalanced by the non-optimal particle dispersibility and by the presence of particle agglomerates and macro-aggregates that act as defects and are detrimental to the dielectric strength. On the other hand, the functionalized sample P_14_BTH_G presents improved breakdown strength, up to 45 kV/mm. Here the combined action of polymer matrix stiffening with the functionalization that results in dipole re-orientation with an increase of E_{BD} value of + 30.7 % with respect to the corresponding un-deformed sample.

3.6.4 Energy Density Evaluation

At this point, knowing the value of the dielectric constant and of the dielectric breakdown strength for all samples in both their un-deformed and deformed state it is possible to calculate the energy density of these materials. The energy density is calculated through the following equation:

$$U = \frac{1}{2}\varepsilon_0 \varepsilon_r E_{BD}^2$$

Where ε_0 is the vacuum permittivity, ε_r the permittivity value at the frequency of 1 kHz, and E_{BD} is the dielectric strength of the material, the results give an energy density calculated in J/cm^3. The results for stretched and un-stretched specimens are summarized in Table 14. It is worth noting that the results presented in Table 14 are just an estimation of the electrostatic energy density that can be stored in the dielectric in undeformed and deformed conditions, but the convertible energy density also depends on the maximum deformation that the DEG can sustain and on the type of deformation [41]. This is a limitation of this study that is more focused on exploring the energy harvesting potential of the nanocomposites by looking at the properties of the material; the characterization of the maximum stretchability and the experimental evaluation of the energy harvesting performance will be the subject of further studies.

Table 14 Summary of dielectric constant, dielectric breakdown value, and energy density for both un-deformed and deformed PDMS films composite.

Sample	ε_r (1 kHz)	E_{BD} [kV/mm]	U [J/cm^3]	ε_r (1 kHz) Stretch	E_{BD} [kV/mm] Stretch	U [J/cm^3] Stretch
Pf_neat	2.8	33.8	**0.028** -	2.8	34.2	**0.029** -
Pf_3.5_BTH	5.5	34.6	**0.058 (+107%)**	3.7	40.7	**0.054 (+86%)**
Pf_3.5_BTH_G	7.6	39.9	**0.107 (+282%)**	3.7	44.8	**0.065 (+124%)**
Pf_3.5_BTH_A	7.1	42.1	**0.111 (+296%)**	4.3	44.8	**0.076 (+162%)**
Pf_14_BTH	8.1	33.0	**0.078 (+178%)**	3.6	34.0	**0.036 (+24%)**
Pf_14_BTH_G	10.3	34.8	**0.110 (+294%)**	4.6	45.5	**0.084 (+190%)**

The neat PDMS has a base value of energy density of approximately 0.03 J/cm^3 and this value remains constant in standard and deformed conditions due to the unchanged dielectric constant and the only slight increase in the dielectric breakdown strength. The addition of bare particles at low filler levels (Pf_3.5_BTH) leads to an increase of +107%, and a further increase of +178% at high filler levels (Pf_14_BTH). However, functionalization causes a significant change in the situation, particularly at low filler levels for Pf_3.5_BTH_G and Pf_3.5_BTH_A, resulting in an increase in the energy density of up to 0.11 J/cm^3 for the BTH_A containing composite, which is up to +296% compared to the base value of PDMS. At high filler levels, there are no further advantages as the increase in dielectric constant is accompanied by a decrease in the dielectric breakdown due to the reasons explained in previous paragraphs. Thus, increasing the filler level too much cannot assure better results, while a low filler loading (3.5 vol%) is optimal for simultaneously increasing the dielectric constant and the dielectric breakdown strength, resulting in higher values of energy density and energy harvesting performance. The addition of a large amount of non-functionalized filler could also be problematic, particularly under strain. The presence of large agglomerates acting as defects are detrimental to the dielectric breakdown strength, leading to a decrease in overall energy harvesting performance.

The results obtained in this work point out that the chemical characteristics of the particle-matrix interface play a key role in determining structural and functional properties. The final values of the volumetric energy density are in line with similar materials presented in literature but achieved with a lower filler fraction. The value of energy density is linearly related to the dielectric constant and quadratically with the dielectric breakdown value. For example, concerning the dielectric constant, the value with low filler content rises to 7.6 (at 1 kHz) for Pf_3.5_BTH_G while values ranging from 4 to 6 have been reported at 5 vol% in similar works [219,220]. However, the base value of the electric breakdown of the polymeric matrix can strongly affect the final value of the energy density; In fact, this value can range from 10 up to 2-300 kV/mm for silicones and rubbers [42,116], resulting in a wide range of energy densities. For example, Banet et al. [116] reviewed several works in the literature about polymer ceramic composites for DEG reporting values of energy density from 0.05 to 0.1 J/cm^3 for silicone-$BaTiO_3$ composites with 20 vol% ceramic loadings; this value is in line with results for samples loaded with 3.5 vol% of functionalized BTH particles (Pf_3.5_BTH_G/A). It comes that the

functionalization of barium titanate nanoparticles with organosilanes is a simple and effective tool for gaining high dielectric performance of PDMS composites, at the same time keeping the benefits of the elastomeric matrix thanks to the possibility to employ low filler loadings. In particular, the remarkable increase in energy density obtained with 3.5% BTH_A particles, due to an increase in both E_{BD} and permittivity value, proves that silane coupling agents presenting PEO units in the organic chain, such as APEOPTES reported in this study, have a big potential to increase the dielectric performance of ceramic-elastomer nanocomposites.

The main results on the dielectric performance of PDMS-based films are summarized below:

- Both filler addition and particle functionalization affect the dielectric properties of PDMS; in the specific, they increased the dielectric permittivity, reduced the tangent delta (at low filler content), and influenced the conductivity behavior of the composites, offering further hints on the activation of different polarization mechanisms.
- The beneficial effect of the particle functionalization on the breakdown strength could be related to improved particle dispersibility, reduction of leakage current, and charge traps, capable of storing electric charges before the breakdown, favored by the presence of the organic functions on the particle surface.
- Stretching the composite films resulted in a decrease of the dielectric permittivity and an increase in the dielectric breakdown strength at different intensities depending on filler content and functionalization.
- The improved dielectric performance of nanocomposites leads to an increase in theoretical energy density, which depends both on particles amount and their functionalization.

Conclusions

This thesis focused on the production of polymer-ceramic composites to convert and harvest energy using the piezoelectric effect and mechanical deformation, performing all the steps from the production of the ceramic filler by sol-gel synthesis both at ambient and hydrothermal conditions, to particles' functionalization and embedding into different polymeric matrices.

Concerning the production of $BaTiO_3$ nanofillers:

- Both BT and BTH particles resulted from the agglomeration of primary particles and presented a regular spherical shape and smaller dimensions compared to commercial particles. Furthermore, good values of tetragonality were obtained.
- BTH powders, prepared by hydrothermal synthesis, were proven to exhibit superior characteristics, (aspect ratio, size distribution, organic residuals) if compared to traditional sol-gel synthesis, and the optimization of the hydrothermal reaction showed that 2h reaction time ensured better particle properties also reducing time and energy consumption.

To improve particles' dispersibility in organic matrices and add functionalities to modify the organic-inorganic interface, the possibility of functionalizing the inorganic fillers was evaluated.

Concerning particles functionalization:

- $BaTiO_3$ particle reactivity was enhanced thanks to the H_2O_2 treatment. Hydroxylation studies revealed that the 8h hydroxylation process results in the highest functionalization yield.
- BTH particles were functionalized with different organosilanes, namely GPTMS (G), APEOPTES (A), and TESPEOD (T). The functionalization was successful in all cases; the grafting density was higher for G (10.6 molecules·nm^{-2}) than for A and T (3.5 and 3.2 molecules·nm^{-2}, respectively), probably because of their longer organic chains, resulting in steric hindrance and electronic inductive effects.

Both bare BTH and particles functionalized with G (BTH_G), and A (BTH_A) were used to produce PDMS- and epoxy-based nanocomposites, in order to evaluate the effect of the particle-matrix interface on nanocomposites properties. Nanocomposite disks, prepared with low (3.5 vol%) and high (21 vol%) filler content, were produced by solution-casting followed by

thermal curing and the application of a DC electric field. The main achievements are summarized below:

- PDMS composites showed greater flexibility, smoother surfaces, and fewer defects than those made with epoxy.
- In both cases, the use of functionalized powders strongly reduced the occurrence of defects. With bare BTH NPs, aggregated clusters, and unfilled areas were observed, while a significant improvement in particle dispersion was found with BTH_G and BTH_A, due to the enhanced affinity with the matrix provided by the organic functions on the particle surface.
- SEM images of PDMS composites showed good matrix-filler continuity, but EDXS maps revealed significant variations and particle alignment related to DC field application and surface modification.
- NMR dynamic study showed that the molecular motion of PDMS chains is generally insensitive to the presence of particles, with only a minor effect of filler concentration that causes a reorganization of the polymer chains around the NPs with some stiffening.
- The piezoelectric coefficient d_{33} was measured for bulk disk nanocomposites using a piezo-d_{33}-meter. Measures on BTH pellets demonstrated that the produced powders have good piezoelectric properties (85 pC/N). Despite that, composites showed poor piezoelectricity. This is probably due to the fact that the particles were scarcely subjected to compression, the matrix carrying the load; moreover, relatively low filler content and inhomogeneous electric field during the curing/poling procedure could contribute to the observed behavior of the composites.

Because of the incapability to assess the piezoelectric properties, the potential of PDMS-based films with both bare and functionalized BTH particles as dielectric elastomers for energy harvesting was explored through dielectric spectroscopy and electric breakdown measurements.

- The addition of BTH powders was found to increase the permittivity, particularly at low frequencies, due to interfacial polarization between particles. The extent of this

effect depended on the amount of filler added, but the increase in the dielectric constant was not linear with the filler quantity.

- Interestingly, functionalization enhanced permittivity by activating polarization mechanisms, leading to increased values at lower frequencies because of both interfacial and dipole polarization.
- A stronger particle-matrix interface given by the presence of functionalizing agent was also found to be beneficial for the dielectric loss at low filler concentrations. However, at higher concentrations, inhomogeneities and particle aggregates led to higher losses.
- The sample conductivity showed linear behavior in the log-log scale, decreasing at low frequencies. The neat PDMS remained insulating at all temperatures exhibiting a plateau indicating a DC conductivity behavior at low frequencies. With increasing temperature, the plateau region shifted to a higher frequency and its magnitude increased due to the thermally activated character of the conductivity. The effect was more evident with particles functionalized with APEOPTES.
- PDMS-based composites exhibited a dielectric breakdown between 33 and 42 kV/mm, with functionalized particles having a positive impact on the breakdown strength thanks to better particle dispersibility resulting in more homogenous composites. However, highly loaded samples showed no significant improvement, since particle agglomerates reduced the beneficial effect of particle addition.
- Pre-stretching was studied for its impact on the dielectric properties of composites. The dielectric constant showed a decrease during stretching, which can be attributed to different factors such as dipoles in the polymeric chain, strain crystallization mechanisms, and local constraints like particles and fillers. Additionally, the dielectric breakdown strength increased, varying based on the filler content and functionalization, likely due to the stiffening of the elastomeric membrane.
- The potential energy harvesting performance of the samples was also evaluated by calculating the theoretical energy density. The addition of bare particles resulted in a significant increase in energy density with increasing filler amount in unstretched samples while the improvement was limited in stretched samples. It is worth noting

the significant effect of particles' functionalization particularly at low filler percentage, resulting in a remarkable increase in energy density due to the increase of both permittivity and electric breakdown.

To conclude, the functionalization of $BaTiO_3$ nanoparticles with organosilanes successfully enhances the dielectric performance of PDMS-based composites by incorporating small amounts of filler. The use of organotrialkoxysilanes containing PEO units positively affects particle-matrix interfaces, resulting in more uniform nanocomposites with improved dielectric properties. This approach can be extended to other ceramic perovskites and polymeric matrices. Understanding the complex interplay of factors affecting dielectric properties is crucial for nanocomposites. The filler-matrix interface is pivotal in achieving desired properties, and surface functionalization is essential for enhancing dielectric properties. This research demonstrates that particle functionalization enables achieving high dielectric permittivity with lower particle content compared to similar studies in the literature. Particle functionalization activates various polarization mechanisms, enhances dielectric breakdown, improves particle dispersibility, and potentially facilitates charge-trapping mechanisms. The hope is that this work will inspire further studies in this area; with this thesis, a simple method to effectively functionalize dielectric ceramics to be embedded in polymeric matrices was provided. Coupling the suitable functionalizing agent with different fillers and matrices is the first step to further increase the performance of the final products.

As further perspectives:

- Work must be done on the production of the composites, optimizing the process parameters of the particle dispersion step (solvent, time, temperature, sonication) and of deposition and curing steps (deposition speed, time, temperature, applied electric field). This will lead to the possibility to increase the filler content and, consequently, achieve enhanced dielectric performance.
- The possibility of producing aligned composites was proven. In this way, it would be possible to produce layered composites in which each layer has a different particle orientation accordingly to the applied electric field to have anisotropic properties.
- These actions can lead to a new class of high-performance dielectrics with tailored and anisotropic properties for energy-harvesting applications.

Appendix - Doping

This appendix presents the procedure, the results, and the discussion of the doping trials done on the BTH powders. This chapter reports data and discussion from "Effect of Hydrothermal Treatment and Doping on the Microstructural Features of Sol-Gel Derived $BaTiO_3$ Nanoparticles" by Zamperlin et al. [155].

5.1 Materials and Methods

5.1.1 Synthesis of Doped Particles

Doped powders were prepared using the 2 h hydrothermal synthesis shown in paragraph 2.2.2. The only difference stands in the fact that sodium acetate ($NaCH_3COO$) (Analyticals Carlo Erba, Milan, Italy, CAS 127-09-3), calcium nitrate tetrahydrate ($Ca(NO_3)_2{\cdot}4H_2O$) (Sigma Aldrich, Saint Louis, MO, USA, CAS 13477-34-4), and bismuth nitrate pentahydrate ($Bi(NO_3)_3{\cdot}5H_2O$) (Sigma Aldrich, Saint Louis, MO, USA, CAS 10035-06-0) were dissolved into the Ba-sol to obtain a theoretical composition $Ba_{0.9}X_{0.1}TiO_3$ (where X = Na^+, Ca^{2+}, Bi^{3+}). Doped particles were labeled BTH_Na, BTH_Ca, BTH_Bi, and BTH_NaBi.

5.1.2 Characterization

Inductive Coupled Plasma – Optical Emission Spectroscopy (ICP-OES)

Chemical analyses were carried out by ICP-OES with a Spectro Ciros Instrument (Spectro Analytical Instruments GmbH & Co, Klevee, Germany). 25 mg of sample were dissolved in 5 ml of concentrated HCl with the addition of a few droplets of H_2O_2, and de-ionized water was added up to a final value of 50 ml. M4M standards were used for the quantitative analysis of Ba, Ti, and dopants.

X-Ray Diffraction

See paragraph 2.6.1.

Raman

See paragraph 2.6.1.

SEM

See paragraph 2.6.1.

5.2 Results and Discussions

Chemical analysis was performed on BTH-doped powders to evaluate the effectiveness of doping ICP-OES. Table 15 summarizes the results, reporting the Ba/Ti ratio and the mol % of all the elements involved. The elemental analysis showed that the samples seem to be Ba deficient even if a Ba/Ti ratio of 1.1 was used. This agrees with the literature. It is difficult to obtain stoichiometric $BaTiO_3$ powders via wet chemical synthesis done in a strong basic environment [221–224]. Chemical analysis shows dopants (Na, Ca, and Bi) in the samples but in lower amounts with respect to the theoretical composition, indicating the low effectiveness of doping. Moreover, K is found in all samples, and it is probably due to the use of KOH during the synthesis. Traces of potassium are found when doping is done with a divalent ion (Ca^{2+}) or with a combination of monovalent and trivalent ions (Na^{+} and Bi^{3+}); on the other hand, higher amounts of K are evidenced in Na- and Bi-doped powders. Na is also detected in all samples probably due to its presence in KOH starting solution. Doped samples present a decreased Ba/Ti ratio, this is correlated to the substitution of Ba atoms in doped $BaTiO_3$. All the substituting ions, K^{+}, Na^{+}, Ca^{2+}, and Bi^{3+} are reported to substitute Ba^{2+} in the A-site since their ionic radius is similar [74,95,225–229]. More in detail, Ca^{2+} should effectively substitute Ba^{2+} since the charge balancing (divalent cation substitutes a divalent cation) is maintained. Na content is limited in BTH_Na while the amount of K is higher probably because its ionic radius is similar to the one of Ba. In the BTH_Bi sample, a trivalent dopant element is introduced resulting in a charge imbalance that leads to a large K penetration to compensate for trivalent ions. Similar considerations are valid also for BTH_NaBi. Concluding, in doping, the ionic radius of the dopant element together with the charge balance, plays a key role. These factors can affect the yield and the effectiveness of the substitution.

Table 15 Experimental molar composition of doped $BaTiO_3$ samples from ICP-OES results. [From [155] Zamperlin et al., Materials, 2021, 14(15), 4345]

	Ba/Ti mol ratio	Ba mol %	Ti mol %	K mol %	Na mol %	Ca mol %	Bi mol %

BTH	0.86	45.1	52.2	2.6	0.1	-	-
BTH_Na	0.76	40.0	52.6	5.5	1.9	-	-
BTH_Ca	0.74	38.6	52.1	0.2	1.7	7.6	-
BTH_Bi	0.82	37.9	46.3	10.1	3.4	-	2.3
BTH_NaBi	0.81	41.7	51.6	0.3	2.0	-	4.4

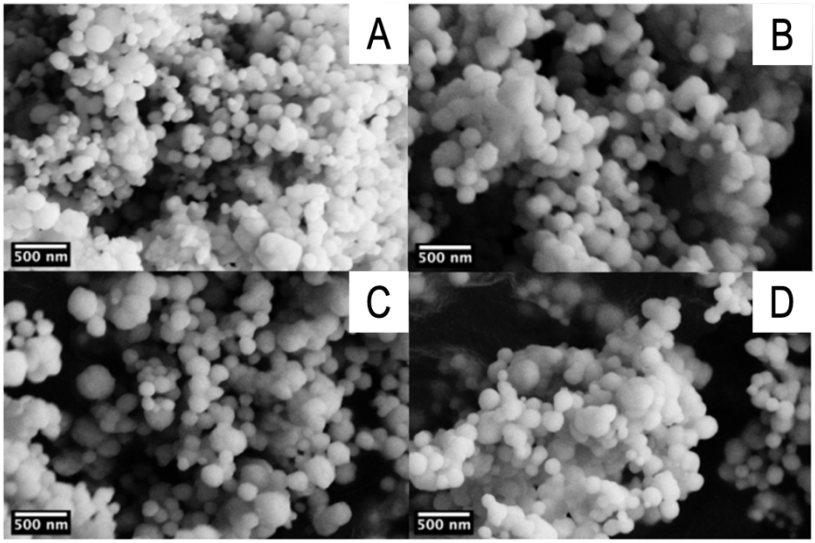

Figure 59 SEM micrographs of doped BTH particles: Na-doped BTH_Na (A), Ca-doped BTH_Ca (B), Bi-doped BTH_Bi (C), and Na-/Bi- doped BTH_NaBi (D). [Adapted from [155] Zamperlin et al., Materials, 2021, 14(15), 4345]

Figure 59 shows SEM images of doped samples and Table 16 summarizes the results from particle analysis in terms of mean size and distribution. The dimensions of particles, regardless of the dopant element have similar dimensions, with their mean in the range of 134 – 149 nm. However, the size distribution of doped BTH is slightly higher with respect to un-doped BTH powders.

Figure 60 shows XRD patterns of doped BTH, $BaTiO_3$ phase is found in all samples, and no additional phases are generally found except for BTH_Bi which reports traces of $Bi_2Ti_2O_4$ (PDF 32-0118) as reported also by Zhou et al.[226]. Results from Rietveld refinement are summarized in Table . All the simulations are reliable, with a good value of goodness of fitting and a low Rwp (%). The presence of Ca does not have noticeable effects on the tetragonality value or the relative amount of the tetragonal phase. The tetragonality value is almost unchanged (1.007) if compared with undoped samples. Also, the literature reports a decrease in the value of tetragonality value in the presence of heterovalent doping ions [228]; this is confirmed by the t values of BTH_Na, BTH_Bi, and BTH_NaBi. In both cases, the decrease of tetragonality is due to a shortening in the c direction of the lattice. Concerning the amount of tetragonal phase, Bi- and NaBi-doped samples present a higher amount of tetragonal phase with respect to undoped samples while Na-doping is responsible for a decrease, and in Ca-doped samples, the value is almost constant. Concluding, crystallite dimensions are generally lower concerning un-doped samples, in particular the crystallites related to the cubic component of $BaTiO_3$.

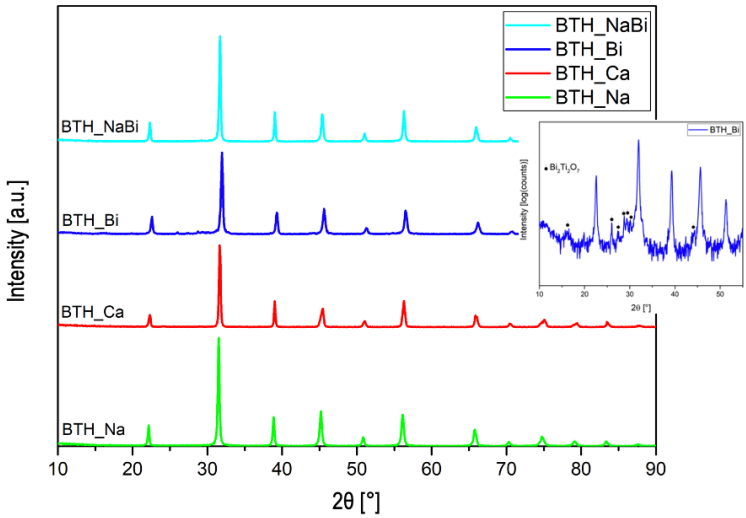

Figure 60 XRD patterns of doped BTH particles: BTH_Na, BTH_Ca, BTH_Bi, and BTH_NaBi. The inset highlights the BTH_Bi pattern in log scale to evidence traces of secondary phases such as $Bi_2Ti_2O_7$. [Adapted from [155] Zamperlin et al., Materials, 2021, 14(15), 4345]

Table 16 Size distribution, quantitative phase analysis, crystallite size, lattice parameters, and tetragonality value of particle produced via the sol-gel synthesis in hydrothermal conditions and doped with different elements, namely, Na, Ca, Bi, and a combination of Na and Bi. [Adapted from [155] Zamperlin et al., Materials, 2021, 14(15), 4345]

	BTH	**BTH_Na**	**BTH_Ca**	**BTH_Bi**	**BTH_NaBi**
Size [nm] (std. dev)	117 (27)	134 (37)	149 (33)	146 (39)	141 (37)
Phase [wt. %] (std. dev)	Tetragonal – Cubic 75(1) – 25(1)	Tetragonal – Cubic 56(2) – 44(2)	Tetragonal – Cubic 76(2) – 24(2)	Tetragonal – Cubic 84(4) – 16(3)	Tetragonal – Cubic 90(1) – 10(1)
Crystallite size [nm] (std.dev)	77(4) – 82(14)	27(1) – 57(1)	62(1) – 112(30)	47(2) – 12(1)	60(1) – 7(1)

a [Å]	4.0039	4.0101	4.0007	4.0020	4.0101
c [Å]	4.0333	4.0331	4.0286	4.0155	4.0221
t = c/a	1.0074	1.0057	1.0070	1.0034	1.0030
Rwp [%]	18.05	17.00	21.49	14.89	17.89

Raman spectroscopy was performed as a complementary structural study. Raman spectra of cation-doped BTH powders are presented in Figure 61. In agreement with XRD results, the Raman spectra of BTH_Ca powders do not present noticeable differences with respect to undoped samples, while the BTH_Na sample has a less intense peak at 306 cm^{-1} (B+E mode), a sign of a lower amount of tetragonal phase [179], this is confirmed by X-Ray diffraction. Then BTH_Bi and BTH_NaBi present a shifting at higher wavenumbers of A_1(TO) mode (250 to 270 cm^{-1}) and A_1E(TO) mode (510 to 520 cm^{-1}), the shifting is caused by Bi^{3+} structure, in agreement with the literature, as reported by Strathdee et al. [230].

In conclusion, doping was done using different dopant elements, namely, Na, Ca, Bi, and a combination of Na and Bi. It was demonstrated that the simultaneous addition of Na and Bi (BTH_NaBi) and Bi (BTH_Bi) leads to a higher amount of final tetragonal phase that is unfortunately, accompanied by a decrease in the value of tetragonality. Ca-doping seems to have negligible effects in modifying the structural features while Na-doping results in a decrease of both tetragonality and amount of tetragonal phase if compared with the undoped sample. Finally, K is found in all samples due to the synthesis process. To conclude, doping efficiency was lower than what was expected theoretically, and it seems that charge balance and, ionic radius and balance of the unit cell deformation play key roles in ruling the final dopant concentration.

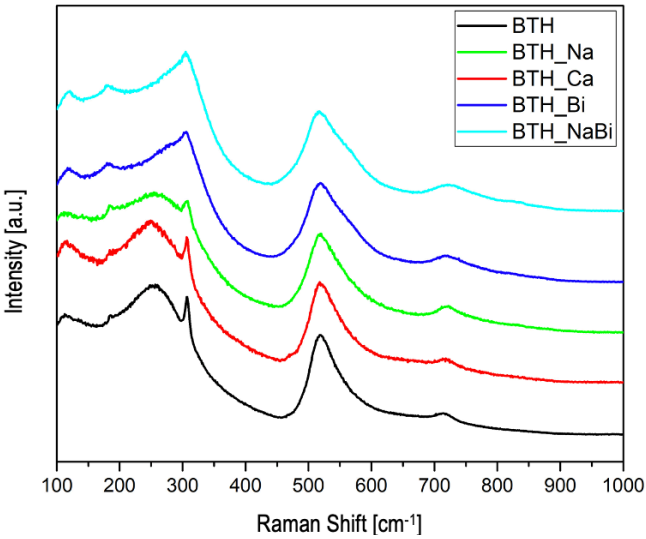

Figure 61 Raman spectra of cation-doped BTH systems: BTH_Na, BTH_Ca, BTH_Bi, and BTH_NaBi. Pure BTH Raman spectrum is reported for the sake of comparison. [Adapted from [155] Zamperlin et al., Materials, 2021, 14(15), 4345]

Bibliography

1. Yang, Z., Zhou, S., Zu, J., et al. “High-Performance Piezoelectric Energy Harvesters and Their Applications,” *Joule*, V. 2, No. 4, 2018, pp. 642–97.
2. Fan, F. R., Tang, W., and Wang, Z. L. “Flexible Nanogenerators for Energy Harvesting and Self-Powered Electronics,” *Advanced Materials*, V. 28, No. 22, 2016, pp. 4283–305.
3. Stuber, V. L., Deutz, D. B., Bennett, J., et al. “Flexible Lead-Free Piezoelectric Composite Materials for Energy Harvesting Applications,” *Energy Technology*, V. 7, No. 1, 2019, pp. 177–85.
4. Qing, X., Li, W., Wang, Y., et al. “Piezoelectric transducer-based structural health monitoring for aircraft applications,” *Sensors*, V. 19, No. 3, 2019, p. 545.
5. Jiao, P., Egbe, K. J. I., Xie, Y., et al. “Piezoelectric sensing techniques in structural health monitoring: A state-of-the-art review,” *Sensors*, V. 20, No. 13, 2020, p. 3730.
6. Nguyen, V. C., Le, M. Q., Fimbel, A., et al. “Printing smart coating of piezoelectric composite for application in condition monitoring of bearings,” *Materials and Design*, V. 215, 2022, p. 110529.
7. Kalantarian, H., Alshurafa, N., Le, T., et al. “Monitoring eating habits using a piezoelectric sensor-based necklace,” *Computers in Biology and Medicine*, V. 58, 2015, pp. 46–55.
8. Priya, S., Song, H. C., Zhou, Y., et al. “A Review on Piezoelectric Energy Harvesting: Materials, Methods, and Circuits,” *Energy Harvesting and Systems*, V. 4, No. 1, 2019, pp. 3–39.
9. Cottone, F. “Introduction to Vibration Energy Harvesting,” *NiPS Energy Harvesting Summer School*, 2011.
10. Erturk, Alper., and Inman, D. J. “Piezoelectric energy harvesting,” First Edition, John Wiley & Sons, 2011, 343–348 pp.
11. Sodano, H. A., Inman, D. J., and Park, G. “A review of power harvesting from vibration using piezoelectric materials,” *The Shock and Vibration Digest*, V. 36, No. 3, 2004, pp. 197–205.

12. Shenck, N. S., and Paradiso, J. A. “Energy scavenging with shoe-mounted piezoelectrics,” *IEEE Micro*, V. 21, No. 3, 2001, pp. 30–42.
13. Moro, L., and Benasciutti., D. “Harvested power and sensitivity analysis of vibrating shoe-mounted piezoelectric cantilevers,” *Smart Materials and Structures*, V. 19, No. 11, 2010, p. 115011.
14. Zhao, J., and You, Z. “A shoe-embedded piezoelectric energy harvester for wearable sensors,” *Sensors*, V. 14, No. 7, 2014, pp. 12497–510.
15. Abidin, H. E. Z., Hamzah, A. A., Yunas, J., et al. “Interdigitated MEMS Supercapacitor for Powering Heart Pacemaker.” Supercapacitor Design and Applications. InTech, 2016.
16. Moretti, G., Papini, G. P. R., Daniele, L., et al. “Modelling and testing of a wave energy converter based on dielectric elastomer generators,” *Proceedings of the Royal Society A: Mathematical, Physical and Engineering Sciences*, V. 475, No. 2222, 2019.
17. Wang, W., He, X., Wang, X., et al. “A bioinspired structure modification of piezoelectric wind energy harvester based on the prototype of leaf veins,” *Sensors and Actuators, A: Physical*, V. 279, 2018, pp. 467–73.
18. Li, S., Yin, G., Chen, G., et al. “Short-term breakdown and long-term failure in nanodielectrics: A review,” *IEEE Transactions on Dielectrics and Electrical Insulation*, V. 17, No. 5, 2010, pp. 1523–35.
19. Barber, P., Balasubramanian, S., Anguchamy, Y., et al. “Polymer composite and nanocomposite dielectric materials for pulse power energy storage,” *Materials*, V. 2, No. 4, 2009, pp. 1697–733.
20. Shen, Y., Lin, Y., Li, M., et al. “High dielectric performance of polymer composite films induced by a percolating interparticle barrier layer,” *Advanced Materials*, V. 19, No. 10, 2007, pp. 1418–22.
21. Sun, Y., Zhang, Z., and Wong, C. P. “Influence of interphase and moisture on the dielectric spectroscopy of epoxy/silica composites,” *Polymer*, V. 46, No. 7, 2005, pp. 2297–305.
22. Lewis, T. J. “Interfaces: Nanometric dielectrics,” *Journal of Physics D: Applied Physics*, V. 38, No. 2, 2005, pp. 202–12.

23. Lewis, T. J. “Interfaces are the Dominant Feature of Dielectrics at the Nanometric Level,” *IEEE Transactions on Dielectrics and Electrical Insulation*, V. 11, No. 5, 2004, p. 739.
24. AlTowireb, S. M., and Goumri-Said, S. “Core-Shell structures for the enhancement of energy harvesting in piezoelectric Nanogenerators: A review,” *Sustainable Energy Technologies and Assessments*, V. 55, 2023.
25. Zhou, Z., Du, X., Luo, J., et al. “Coupling of interface effects and porous microstructures in translucent piezoelectric composites for enhanced energy harvesting and sensing,” *Nano Energy*, V. 84, 2021.
26. Cho, S., Lee, J. S., and Jang, J. “Enhanced Crystallinity, Dielectric, and Energy Harvesting Performances of Surface-Treated Barium Titanate Hollow Nanospheres/PVDF Nanocomposites,” *Advanced Materials Interfaces*, V. 2, No. 10, 2015, p. 1500098.
27. Ballato, A. “Piezoelectricity: History and new thrusts.” Proceedings of the IEEE Ultrasonics Symposium, vol. 1. IEEE, 1996. pp. 575–83.
28. Yang, J. “An introduction to the theory of piezoelectricity,” v. vol. 9, Boston, Springer, 2005, 299 pp.
29. Covaci, C., and Gontean, A. “Piezoelectric energy harvesting solutions: A review,” *Sensors*, V. 20, No. 12, 2020, p. 3512.
30. APC International, L. “Piezoelectric Ceramics: Principles and Applications,” 2nd Edition, APC International, 2011, 2011.
31. Manbachi, A., and Cobbold, R. S. C. “Development and application of piezoelectric materials for ultrasound generation and detection,” *Ultrasound*, V. 19, No. 4, 2011, pp. 187–96.
32. Shung, K. K., Cannata, J. M., and Zhou, Q. F. “Piezoelectric materials for high frequency medical imaging applications: A review,” *Journal of Electroceramics*, V. 19, No. 1, 2007, pp. 139–45.
33. Gao, J., Xue, D., Liu, W., et al. “Recent progress on BaTiO3-based piezoelectric ceramics for actuator applications,” *Actuators*, V. 6, No. 3, 2017, p. 24.

34. Xu, K., Li, J., Lv, X., et al. “Superior Piezoelectric Properties in Potassium–Sodium Niobate Lead-Free Ceramics.,” *Advanced Materials*, V. 28, No. 38, 2016, pp. 8519–23.
35. Reichmann, K., Feteira, A., and Li, M. “Bismuth Sodium Titanate based materials for piezoelectric actuators,” *Materials*, V. 8, No. 12, 2015, pp. 8467–95.
36. Abinnas, N., Baskaran, P., Harish, S., et al. “0.8 V nanogenerator for mechanical energy harvesting using bismuth titanate–PDMS nanocomposite,” *Applied Surface Science*, V. 418, 2017, pp. 362–8.
37. Song, J., Zhao, G., Li, B., et al. “Design optimization of PVDF-based piezoelectric energy harvesters,” *Heliyon*, V. 3, 2017, p. e00377.
38. Arlt, K., and Wegener, M. “Piezoelectric PZT / PVDF-copolymer 0-3 composites: Aspects on film preparation and electrical poling,” *IEEE Transactions on Dielectrics and Electrical Insulation*, V. 17, No. 4, 2010, pp. 1178–84.
39. Mokni, M., Maggioni, G., Kahouli, A., et al. “Nanocomposite-parylene C thin films with high dielectric constant and low losses for future organic electronic devices,” *Beilstein Journal of Nanotechnology*, V. 10, No. 1, 2019, pp. 428–41.
40. Yucel, T., Cebe, P., and Kaplan, D. L. “Structural origins of silk piezoelectricity,” *Advanced Functional Materials*, V. 21, No. 4, 2011, pp. 779–85.
41. Moretti, G., Rosset, S., Vertechy, R., et al. “A Review of Dielectric Elastomer Generator Systems,” *Advanced Intelligent Systems*, V. 2, No. 10, 2020, p. 2000125.
42. Chen, Y., Agostini, L., Moretti, G., et al. “Dielectric elastomer materials for large-strain actuation and energy harvesting: A comparison between styrenic rubber, natural rubber and acrylic elastomer,” *Smart Materials and Structures*, V. 28, No. 11, 2019, p. 114001.
43. Di, K., Bao, K., Chen, H., et al. “Dielectric elastomer generator for electromechanical energy conversion: A mini review,” *Sustainability*, V. 13, No. 17, 2021, p. 9881.
44. Yahyaoui, H., Notingher, P., Agnel, S., et al. “Electrical breakdown of epoxy and PTFE under dc conditions.” Proceedings of the 2016 IEEE International Conference on Dielectrics, ICD 2016, vol. 2. Institute of Electrical and Electronics Engineers Inc., 2016.

45. Romasanta, L. J., Lopez-Manchado, M. A., and Verdejo, R. “Increasing the performance of dielectric elastomer actuators: A review from the materials perspective,” *Progress in Polymer Science*, V. 51, 2015, pp. 188–211.
46. Ibrahim, I. D., Sadiku, E. R., Jamiru, T., et al. “Prospects of nanostructured composite materials for energy harvesting and storage,” *Journal of King Saud University - Science*, V. 32, No. 1, 2020, pp. 758–64.
47. Coondoo, I., Panwar, N., Amorín, H., et al. “Enhanced Piezoelectric Properties of Praseodymium-Modified Lead-Free (Ba0.85Ca0.15)(Ti0.90Zr0.10)O3 Ceramics,” *Journal of the American Ceramic Society*, V. 98, No. 10, 2015, pp. 3127–35.
48. Nayak, S., Sahoo, B., Kumar Chaki, T., et al. “Development of polyurethane-titania nanocomposites as dielectric and piezoelectric material,” *RSC Advances*, V. 3, No. 8, 2013, pp. 2620–31.
49. Salaeh, S., Boiteux, G., Cassagnau, P., et al. “Flexible 0-3 ceramic-polymer composites of barium titanate and epoxidized natural rubber,” *International Journal of Applied Ceramic Technology*, V. 12, No. 1, 2015, pp. 106–15.
50. Banerjee, S., Cook-Chennault, K. A., Du, W., et al. “Piezoelectric and dielectric characterization of corona and contact poled PZT-epoxy-MWCNT bulk composites,” *Smart Materials and Structures*, V. 25, No. 11, 2016, p. 115018.
51. Ariati, R., Sales, F., Souza, A., et al. “Polydimethylsiloxane composites characterization and its applications: A review,” *Polymers*, V. 13, No. 23, 2021.
52. Furukawa, T., Ishida, K., and Fukada, E. “Piezoelectric properties in the composite systems of polymers and PZT ceramics,” *Journal of Applied Physics*, V. 50, No. 7, 1979, pp. 4904–12.
53. Babu, I., and de With, G. “Highly flexible piezoelectric 0-3 PZT-PDMS composites with high filler content,” *Composites Science and Technology*, V. 91, 2014, pp. 91–7.
54. Patnam, H., Dudem, B., Alluri, N. R., et al. “Piezo/triboelectric hybrid nanogenerators based on Ca-doped barium zirconate titanate embedded composite polymers for wearable electronics,” *Composites Science and Technology*, V. 188, 2020, p. 107963.

55. Testino, A., Buscaglia, M. T., Viviani, M., et al. “Synthesis of BaTiO3 Particles with Tailored Size by Precipitation from Aqueous Solutions,” *Journal of American Ceramic Society*, V. 87, No. 1, 2004, pp. 79–83.

56. Jing, L., Wang, G., Duan, Y., et al. “Synthesis and electromagnetic characteristics of the flake-shaped barium titanate powder,” *Journal of Alloys and Compounds*, V. 475, Nos. 1–2, 2009, pp. 862–8.

57. Jian, G., Jiao, Y., Meng, Q., et al. “3D BaTiO3 Flower Based Polymer Composites Exhibiting Excellent Piezoelectric Energy Harvesting Properties,” *Advanced Materials Interfaces*, V. 7, No. 16, 2020, p. 2000484.

58. Joshi, U. A., and Lee, J. S. “Template-free hydrothermal synthesis of single-crystalline barium titanate and strontium titanate nanowires,” *Small*, V. 1, No. 12, 2005, pp. 1172–6.

59. Chowdhury, A. R., Jaksik, J., Hussain, I., et al. “Multicomponent nanostructured materials and interfaces for efficient piezoelectricity,” *Nano-Structures and Nano-Objects*, V. 17, 2019, pp. 148–84.

60. Khanbareh, H., van der Zwaag, S., and Groen, W. A. “In-situ poling and structurization of piezoelectric particulate composites,” *Journal of Intelligent Material Systems and Structures*, V. 28, No. 18, 2017, pp. 2467–72.

61. Zhang, X., Le, M. Q., Zahhaf, O., et al. “Enhancing dielectric and piezoelectric properties of micro-ZnO/PDMS composite-based dielectrophoresis,” *Materials and Design*, V. 192, 2020, p. 108783.

62. Liu, X., Sun, H., Liu, S., et al. “Mechanical, dielectric and actuated properties of carboxyl grafted silicone elastomer composites containing epoxy-functionalized TiO2 filler,” *Chemical Engineering Journal*, V. 393, 2020, p. 124791.

63. Akdogan, E. K., Allahverdi, M., and Safari, A. “Piezoelectric composites for sensor and actuator applications,” *IEEE Transactions on Ultrasonics, Ferroelectrics, and Frequency Control*, V. 52, No. 5, 2005, pp. 746–75.

64. Tselikos, G., Rasul, S., Groen, P., et al. “In situ printing and functionalization of hybrid polymer-ceramic composites using a commercial 3d printer and dielectrophoresis—a novel conceptual design,” *Polymers*, V. 13, No. 22, 2021, p. 3979.

65. D'Ambrogio, G., Zahhaf, O., Hebrard, Y., et al. "Micro-Structuration of Piezoelectric Composites Using Dielectrophoresis: Toward Application in Condition Monitoring of Bearings," *Advanced Engineering Materials*, V. 23, No. 1, 2021, pp. 2000773-1–13.
66. Park, C., and Robertson, R. E. "Aligned microstructure of some particulate polymer composites obtained with an electric field," *Journal of Materials Science*, V. 33, 1998, pp. 3541–53.
67. Takahashi, T., Murayama, T., Higuchi, A., et al. "Aligning vapor-grown carbon fibers in polydimethylsiloxane using dc electric or magnetic field," *Carbon*, V. 44, No. 7, 2006, pp. 1180–8.
68. Randall, C. A., Newnham, R. E., and Cross, L. E. "History of the First Ferroelectric Oxide, BaTiO3," University Park, PA, 2004.
69. Vijatović, M. M., Bobić, J. D., and Stojanović, B. D. "History and challenges of barium titanate: Part I," *Science of Sintering*, V. 40, No. 2, 2008, pp. 155–65.
70. Vijatović, M. M., Bobić, J. D., and Stojanović, B. D. "History and challenges of barium titanate: Part II," *Science of Sintering*, V. 40, No. 3, 2008, pp. 235–44.
71. Kwei, G. H., Lawson, A. C., Billinge, S. J. L., et al. "Structures of the Ferroelectric Phases of Barium Titanate," *Journal of Physical Chemistry*, V. 97, 1993, pp. 2368–77.
72. Moulson, J., and Herbert, J. M. "Electroceramics: materials, properties, applications. ," 2nd edition, John Wiley & Sons, 2003.
73. Buscaglia, V., and Randall, C. A. "Size and scaling effects in barium titanate. An overview," *Journal of the European Ceramic Society*, V. 40, No. 11, 2020, pp. 3744–58.
74. de Andrade, M. C., Carneiro, G. N., Moreira, E. L., et al. "Synthesis and characterization of barium titanate by solid-state reaction," *Materials Science Forum*, V. 802, 2014, pp. 285–90.
75. Byrappa, K., and Adschiri, T. "Hydrothermal technology for nanotechnology," *Progress in Crystal Growth and Characterization of Materials*, V. 53, No. 2, 2007, pp. 117–66.

76. Hench, L. L., and West, J. K. “The Sol-Gel Process,” *Chemical Reviews*, V. 90, 1990, pp. 33–72.
77. Wang, W., Cao, L., Liu, W., et al. “Low-temperature synthesis of BaTiO3 powders by the sol-gel-hydrothermal method,” *Ceramics International*, V. 39, No. 6, 2013, pp. 7127–34.
78. Pfaff, G. “Sol-Gel Synthesis of Barium Titanate Powders of Various Compositions,” *Journal of Materials Chemistry*, V. 2, No. 6, 1992, pp. 591–4.
79. Hwang, U.-Y., Park, H.-S., and Koo, K.-K. “Low-Temperature Synthesis of Fully Crystallized Spherical BaTiO 3 Particles by the Gel-Sol Method,” *Journal of American Ceramic Society*, V. 87, No. 12, 2004, pp. 2168–74.
80. Hwang, U. Y., Park, H. S., and Koo, K. K. “Behavior of Barium Acetate and Titanium Isopropoxide during the Formation of Crystalline Barium Titanate.,” *Industrial & Engineering Chemistry Research*, V. 43, No. 3, 2004, pp. 728–34.
81. Ávila, H. A., Ramajo, L. A., Reboredo, M. M., et al. “Hydrothermal synthesis of BaTiO3 from different Ti-precursors and microstructural and electrical properties of sintered samples with submicrometric grain size.,” *Ceramics International*, V. 37, No. 7, 2011, pp. 2383–90.
82. Baiju, K. G., Nagarajan, A., Marappa Gounder Sadasivam, A., et al. “Hydrothermal synthesis, dielectric properties of barium titanate, cobalt doped barium titanate, and their graphene nanoplatelet composites,” *Asia-Pacific Journal of Chemical Engineering*, V. 15, No. 5, 2020, p. e2550.
83. Muniyappan, S., Solaiyammal, T., Sudhakar, K., et al. “Conventional hydrothermal synthesis of titanate nanotubes: Systematic discussions on structural, optical, thermal and morphological properties,” *Modern Electronic Materials*, V. 3, No. 4, 2017, pp. 174–8.
84. Lee, S. K., Choi, G. J., Hwang, U. Y., et al. “Effect of molar ratio of KOH to Ti-isopropoxide on the formation of BaTiO3 powders by hydrothermal method,” *Materials Letters*, V. 57, No. 15, 2003, pp. 2201–7.

85. Magnone, E., Kim, J. R., and Park, J. H. “The effect of the hydrothermal synthesis variables on barium titanate powders,” *Ceramics International*, V. 42, No. 8, 2016, pp. 10030–6.

86. Wu, Y. T., Wang, X. F., Yu, C. L., et al. “Preparation and characterization of barium titanate (BaTiO3) Nano-powders by pechini sol-gel method,” *Materials and Manufacturing Processes*, V. 27, No. 12, 2012, pp. 1329–33.

87. Kakihana, M., Arima, M., Nakamura, Y., et al. “Spectroscopic characterization of precursors used in the pechini-type polymerizable complex processing of barium titanate,” *Chemistry of Materials*, V. 11, No. 2, 1999, pp. 438–50.

88. Gomes, M. A., Lima, Á. S., Eguiluz, K. I. B., et al. “Wet chemical synthesis of rare earth-doped barium titanate nanoparticles,” *Journal of Materials Science*, V. 51, No. 10, 2016, pp. 4709–27.

89. Badapanda, T., Senthil, V., Panigrahi, S., et al. “Diffuse phase transition behavior of dysprosium doped barium titanate ceramic,” *Journal of Electroceramics*, V. 31, Nos. 1–2, 2013, pp. 55–60.

90. Kundu, T. K., Jana, A., and Barik, P. “Doped barium titanate nanoparticles,” *Bulletin of Materials Science*, V. 31, No. 3, 2008, pp. 501–5.

91. Rani, A., Kolte, J., and Gopalan, P. “Structural, electrical, magnetic and magnetoelectric properties of Co-doped BaTiO3 multiferroic ceramics,” *Ceramics International*, V. 44, No. 14, 2018, pp. 16703–11.

92. Vijatović Petrović, M. M., Bobić, J. D., Banys, J., et al. “Electrical properties of antimony doped barium titanate ceramics,” *Materials Research Bulletin*, V. 48, No. 10, 2013, pp. 3766–72.

93. Soni, M., Saleem, M., Bajpai, N., et al. “Structural and Optical Properties on Na Doped BaTiO 3.” AIP Conference Proceedings 2100. 2019. p. 020185.

94. Sun, D., Jin, X., Liu, H., et al. “Investigation on FTIR spectrum of barium titanate ceramics doped with alkali ions,” *Ferroelectrics*, V. 355, 2007, pp. 145–8.

95. Liao, J. X., Wei, X. B., Xu, Z. Q., et al. “Effect of potassium-doped concentration on structures and dielectric performance of barium-strontium-titanate films,” *Vacuum*, V. 107, 2014, pp. 291–6.

96. Sharma, V., Pilania, G., Rossetti, G. A., et al. “Comprehensive examination of dopants and defects in BaTiO3 from first principles.,” *Physical Review B*, V. 87, No. 13, 2013, p. 134109.

97. Pokorńy, J., Pasha, U. M., Ben, L., et al. “Use of Raman spectroscopy to determine the site occupancy of dopants in BaTiO3,” *Journal of Applied Physics*, V. 109, No. 11, 2011, pp. 114110-1-114110–5.

98. Jo, S. K., Park, J. S., and Han, Y. H. “Effects of multi-doping of rare-earth oxides on the microstructure and dielectric properties of BaTiO3,” *Journal of Alloys and Compounds*, V. 501, No. 2, 2010, pp. 259–64.

99. Chew, K. Y., Abu Bakar, M., and Abu Bakar, N. H. H. “Effects of sodium doping on phase composition and morphology of barium titanate particles.” AIP Conference Proceedings 1502, vol. 1502. 2012. pp. 348–67.

100. Sharma, H., Jindal, S., and Aggarwal, N. “Impact of copper doping on perovskite structure ferroelectric ceramic,” *Materials Today: Proceedings*, V. 33, No. 3, 2020, pp. 1632–6.

101. Chu, J. P., Chang, C. W., Mahalingam, T., et al. “Effects of Nb doping on properties of barium titanate thin films,” *Journal of Materials Science Letters*, V. 22, 2003, pp. 1269–73.

102. Maurya, D., and Priya, S. “Effect of bismuth doping on the dielectric and piezoelectric properties of Ba1-xBixTiO3 lead-free ceramics,” *Integrated Ferroelectrics*, V. 166, No. 1, 2015, pp. 186–96.

103. Ko, Y. S., Nüesch, F. A., and Opris, D. M. “Charge generation by ultra-stretchable elastomeric electrets,” *Journal of Materials Chemistry C*, V. 5, No. 7, 2017, pp. 1826–35.

104. Jiang, Y., Tian, C., Yao, J., et al. “Nano-Silica/Polydimethyl(methylvinyl)siloxane dielectric elastomer generator with high generating energy density, high efficiency and long fatigue life,” *Chemical Engineering Journal*, V. 439, 2022, p. 135339.

105. James, N. K., Van Den Ende, D., Lafont, U., et al. “Piezoelectric and mechanical properties of structured PZT-epoxy composites,” *Journal of Materials Research*, V. 28, No. 4, 2013, pp. 635–41.

106. Kim, H. J., and Kim, Y. J. “High performance flexible piezoelectric pressure sensor based on CNTs-doped 0–3 ceramic-epoxy nanocomposites,” *Materials and Design*, V. 151, 2018, pp. 133–40.

107. Jin, F. L., Li, X., and Park, S. J. “Synthesis and application of epoxy resins: A review,” *Journal of Industrial and Engineering Chemistry*, V. 29, 2015, pp. 1–11.

108. Sakib, M. N., and Iqbal, A. A. “Epoxy Based Nanocomposite Material for Automotive Application- A Short Review,” *International Journal of Automotive and Mechanical Engineering*, V. 18, No. 3, 2021, pp. 9127–40.

109. Bilyeu, B., Brostow, W., and Menard, K. P. “Epoxy Thermosets and Their Applications I: Chemical Structures and Applications,” *Journal of Materials Education*, V. 21, No. 6, n.d., pp. 281–6.

110. Shundo, A., Yamamoto, S., and Tanaka, K. “Network Formation and Physical Properties of Epoxy Resins for Future Practical Applications,” *JACS Au*, V. 2, No. 7, 2022, pp. 1522–42.

111. Mohan, P. “A Critical Review: The Modification, Properties, and Applications of Epoxy Resins,” *Polymer - Plastics Technology and Engineering*, V. 52, No. 2, 2013, pp. 107–25.

112. Cooke, H. G., Mc Whorter, W. F., and Strohscher, A. R. “Chemical Resistance of Epoxy Resins,” *Industrial and Engineering Chemistry*, V. 56, No. 5, 1964, pp. 38–41.

113. Mi, X., Liang, N., Xu, H., et al. “Toughness and its mechanisms in epoxy resins,” *Progress in Materials Science*, V. 130, 2022, p. 100977.

114. Tzetzis, D., Tsongas, K., and Mansour, G. “Determination of the mechanical properties of epoxy silica nanocomposites through FEA-supported evaluation of ball indentation test results,” *Materials Research*, V. 20, No. 6, 2017, pp. 1571–8.

115. Chen, J., Zheng, J., Gao, Q., et al. “Polydimethylsiloxane (PDMS)-based flexible resistive strain sensors for wearable applications,” *Applied Sciences*, V. 8, No. 3, 2018, p. 345.

116. Banet, P., Zeggai, N., Chavanne, J., et al. “Evaluation of dielectric elastomers to develop materials suitable for actuation,” *Soft Matter*, V. 17, No. 48, 2021, pp. 10786–805.

117. Wang, X., Yang, B., Liu, J., et al. “A flexible triboelectric-piezoelectric hybrid nanogenerator based on P(VDF-TrFE) nanofibers and PDMS/MWCNT for wearable devices,” *Scientific Reports*, V. 6, 2016, p. 36049.

118. Sappati, K. K., and Bhadra, S. “0-3 barium titanate-PDMS flexible film for tactile sensing.” I2MTC 2020 - International Instrumentation and Measurement Technology Conference, Proceedings. Institute of Electrical and Electronics Engineers Inc., 2020.

119. Gao, X., Zheng, M., Yan, X., et al. “The alignment of BCZT particles in PDMS boosts the sensitivity and cycling reliability of a flexible piezoelectric touch sensor,” *Journal of Materials Chemistry C*, V. 7, No. 4, 2019, pp. 961–7.

120. Zhou, J., Khodakov, D. A., Ellis, A. V., et al. “Surface modification for PDMS-based microfluidic devices,” *Electrophoresis*, V. 33, No. 1, 2012, pp. 89–104.

121. Nilagiri Balasubramanian, K. B., and Ramesh, T. “Role, effect, and influences of micro and nano-fillers on various properties of polymer matrix composites for microelectronics: A review,” *Polymers for Advanced Technologies*, V. 29, No. 6, 2018, pp. 1568–85.

122. Moczo, J., Fekete, E., Laszlo, K., et al. “Aggregation of Particulate Fillers: Factors, Determination, Properties,” *Macromolecular Symposium*, V. 194, 2003, pp. 111–24.

123. Khastgir, D., and Adachi, K. “Rheological and dielectric studies of aggregation of barium titanate particles suspended in polydimethylsiloxane,” *Polymer*, V. 41, 2000, pp. 6403–13.

124. Kiss, A., Fekete, E., and Pukánszky, B. “Aggregation of CaCO3 particles in PP composites: Effect of surface coating,” *Composites Science and Technology*, V. 67, Nos. 7–8, 2007, pp. 1574–83.

125. Domrzalski, J. N., Stevens, T. E., Van Ginhoven, R. M., et al. “Surface Functionalized Barium Titanate Nanoparticles: A Combined Experimental and Computational Study,” *ECS Journal of Solid State Science and Technology*, V. 11, No. 6, 2022, p. 063006.

126. Tawade, B. V., Apata, I. E., Singh, M., et al. “Recent developments in the synthesis of chemically modified nanomaterials for use in dielectric and electronics applications,” *Nanotechnology*, V. 32, No. 14, 2021.

127. Mensah, B., Kumar, D., Lee, G. B., et al. “Gold functionalized-graphene oxide-reinforced acrylonitrile butadiene rubber nanocomposites for piezoresistive and piezoelectric applications,” *Carbon Letters*, V. 25, No. 1, 2018, pp. 1–13.

128. Yang, D., Ruan, M., Huang, S., et al. “Dopamine and silane functionalized barium titanate with improved electromechanical properties for silicone dielectric elastomers,” *RSC Advances*, V. 6, No. 93, 2016, pp. 90172–83.

129. Sun, H., Qi, Y., and Zhang, J. “Surface organic modified magnesium titanate particles with three coupling agents: Characterizations, properties and potential application areas,” *Applied Surface Science*, V. 520, 2020, p. 146322.

130. Yang, D., Ni, Y., Xu, Y., et al. “Nitrile-butadiene rubber composites with improved electromechanical properties obtained by modification of BaTiO3 with co-deposited catechol/polyamine and silane grafting,” *Polymer*, V. 183, 2019, p. 121813.

131. Sundar, U., Lao, Z., and Cook-Chennault, K. “Investigation of piezoelectricity and resistivity of surface modified barium titanate nanocomposites,” *Polymers*, V. 11, 2019, p. 2123.

132. Dalle Vacche, S., Oliveira, F., Leterrier, Y., et al. “Effect of silane coupling agent on the morphology, structure, and properties of poly(vinylidene fluoride-trifluoroethylene)/BaTiO3 composites,” *Journal of Materials Science*, V. 49, No. 13, 2014, pp. 4552–64.

133. Fan, Y., Wang, G., Huang, X., et al. “Molecular structures of (3-aminopropyl)trialkoxysilane on hydroxylated barium titanate nanoparticle surfaces induced by different solvents and their effect on electrical properties of barium titanate based polymer nanocomposites,” *Applied Surface Science*, V. 364, 2016, pp. 798–807.

134. Siddabattuni, S., Schuman, T. P., and Dogan, F. “Improved polymer nanocomposite dielectric breakdown performance through barium titanate to epoxy interface control,” *Materials Science and Engineering B: Solid-State Materials for Advanced Technology*, V. 176, No. 18, 2011, pp. 1422–9.

135. Cai, Z., Wang, X., Luo, B., et al. “Dielectric response and breakdown behavior of polymer-ceramic nanocomposites: The effect of nanoparticle distribution,” *Composites Science and Technology*, V. 145, 2017, pp. 105–13.

136. Li, C. C., Chang, S. J., Lee, J. T., et al. “Efficient hydroxylation of BaTiO3 nanoparticles by using hydrogen peroxide,” *Colloids and Surfaces A: Physicochemical and Engineering Aspects*, V. 361, Nos. 1–3, 2010, pp. 143–9.

137. Zhu, M., Huang, X., Yang, K., et al. “Energy storage in ferroelectric polymer nanocomposites filled with core-shell structured polymer@BaTiO3 nanoparticles: Understanding the role of polymer shells in the interfacial regions,” *ACS Applied Materials and Interfaces*, V. 6, No. 22, 2014, pp. 19644–54.

138. Liu, Y., Li, Y., Li, X. M., et al. “Kinetics of (3-aminopropyl)triethoxylsilane (aptes) silanization of superparamagnetic iron oxide nanoparticles,” *Langmuir*, V. 29, No. 49, 2013, pp. 15275–82.

139. Thames, S. F., and Panjnani, K. G. “Organosilane Polymer Chemistry: A Review,” *Journal of Inorganic and Organometallic Polymers*, V. 6, No. 2, 1996, pp. 59–94.

140. Bandl, C., Krempl, N., Berger-Weber, G., et al. “Application of organosilane coatings for improved anti-adhesive properties enabling facilitated demolding in polymer processing,” *Journal of Applied Polymer Science*, V. 138, No. 30, 2021, p. e50714.

141. Liang, J., Wu, X. W., Ling, Y., et al. “Trilaminar structure hydrophobic graphene oxide decorated organosilane composite coatings for corrosion protection,” *Surface and Coatings Technology*, V. 339, 2018, pp. 65–77.

142. Kansara, A. M., Aswal, V. K., and Singh, P. S. “Preparation and characterization of new poly(dimethylsiloxane) membrane series via a ‘cross-linking’ reaction using monomolecular trichloro(alkyl)silane of different alkyl chain and type,” *RSC Advances*, V. 5, No. 64, 2015, pp. 51608–20.

143. Xia, L. L., Li, C. L., and Wang, Y. “In-situ crosslinked PVA/organosilica hybrid membranes for pervaporation separations,” *Journal of Membrane Science*, V. 498, 2016, pp. 263–75.

144. Boerio, F. J., and Williams, J. W. “Structure and Properties of Organosilanes Primers for Adhesive Bonding,” *Applications of Surface Science*, V. 7, 1981, pp. 19–31.

145. Wang, J., and Feldman, D. “Effect of organosilanes on the adhesive properties of epoxy-lignin polyblends,” *Journal of Adhesion Science and Technology*, V. 5, No. 7, 1991, pp. 565–76.

146. Al Othman, Z., and Apblett, A. W. “Synthesis of mesoporous silica grafted with 3-glycidoxypropyltrimethoxy-silane,” *Materials Letters*, V. 63, No. 27, 2009, pp. 2331–4.

147. Ma, P. C., Kim, J. K., and Tang, B. Z. “Functionalization of carbon nanotubes using a silane coupling agent,” *Carbon*, V. 44, No. 15, 2006, pp. 3232–8.

148. Wan, Y. J., Gong, L. X., Tang, L. C., et al. “Mechanical properties of epoxy composites filled with silane-functionalized graphene oxide,” *Composites Part A: Applied Science and Manufacturing*, V. 64, 2014, pp. 79–89.

149. Maitra, P., Ding, J., Huang, H., et al. “Poly(ethylene oxide) Silananted Nanosize Fumed Silica: DSC and TGA Characterization of the Surface,” *Langmuir*, V. 19, No. 21, 2003, pp. 8994–9004.

150. Rufin, M. A., Barry, M. E., Adair, P. A., et al. “Protein resistance efficacy of PEO-silane amphiphiles: Dependence on PEO-segment length and concentration,” *Acta Biomaterialia*, V. 41, 2016, pp. 247–52.

151. Hawkins, M. L., and Grunlan, M. A. “The protein resistance of silicones prepared with a PEO-silane amphiphile,” *Journal of Materials Chemistry*, V. 22, No. 37, 2012, pp. 19540–6.

152. Ngo, B. K. D., Barry, M. E., Lim, K. K., et al. “Thromboresistance of Silicones Modified with PEO-Silane Amphiphiles,” *ACS Biomaterials Science and Engineering*, V. 6, No. 4, 2020, pp. 2029–37.

153. Yan, H., Yuanhao, W., and Hongxing, Y. “TEOS/silane coupling agent composed double layers structure: A novel super-hydrophilic coating with controllable water contact angle value,” *Applied Energy*, V. 185, 2017, pp. 2209–16.

154. Smith, A. M., Huynh, P., Griffin, S., et al. “Strong, Non-specific Adhesion Using C-Lectin Heterotrimers in a Molluscan Defensive Secretion.” Integrative and Comparative Biology, vol. 61. Oxford University Press, 2021. pp. 1440–9.

155. Zamperlin, N., Ceccato, R., Fontana, M., et al. “Effect of Hydrothermal Treatment and Doping on the Microstructural Features of Sol-Gel Derived BaTio3 Nanoparticles,” *Materials*, V. 14, No. 15, 2021, p. 4345.

156. Lutterotti, L. “Maud: a Rietveld analysis program designed for the internet and experiment integration,” *Acta Crystallographica Section A: Foundations and Advances*, V. 56, No. s1, 2000, p. s54.

157. Fedel, M., Callone, E., Ziarelli, F., et al. “Influence of Gd3+ on molecular organization and electrochemical properties of Si-based organic/inorganic sol-gel layers,” *Electrochimica Acta*, V. 341, 2020, p. 136033.

158. Bakhmutov, V. I. “Solid-State NMR in Materials Science,” 1st Edition, CRC Press, 2016.

159. Kolodziejski, W., and Klinowski, J. “Kinetics of cross-polarization in solid-state NMR: A guide for chemists,” *Chemical Reviews*, V. 102, No. 3, 2002, pp. 613–28.

160. Voelkel, R. “High-Resolution Solid-state 13C-NMR Spectroscopy of Polymers New Analytical Methods (37),” *Angewandte Chemie - International Edition*, V. 27, 1988, pp. 1468–83.

161. Meiboom, S., and Gill, D. “Modified spin-echo method for measuring nuclear relaxation times,” *Review of Scientific Instruments*, V. 29, No. 8, 1958, pp. 688–91.

162. Carr, H. Y., and Purcell, E. M. “Effects of Diffusion on Free Precession in Nuclear Magnetic Resonance Experiments,” *Physical Review*, V. 94, No. 3, 1954, pp. 630–8.

163. Samet, M., Kallel, A., and Serghei, A. “Maxwell-Wagner-Sillars interfacial polarization in dielectric spectra of composite materials: Scaling laws and applications,” *Journal of Composite Materials*, V. 56, No. 20, 2022, pp. 3197–217.

164. Ritter, J. J., Roth, R. S., and Blendell, J. E. “Alkoxide Precursor Synthesis and Characterization of Phases in the Barium-Titanium Oxide System,” *Journal of the American Ceramic Society*, V. 69, No. 2, 1986, pp. 155–62.

165. Frey, M. H., and Payne, D. A. “Grain-size effect on structure and phase transformations for barium titanate,” *Physical Review B*, V. 54, No. 5, 1996, pp. 3158–68.

166. Ashiri, R. “Detailed FT-IR spectroscopy characterization and thermal analysis of synthesis of barium titanate nanoscale particles through a newly developed process,” *Vibrational Spectroscopy*, V. 66, 2013, pp. 24–9.

167. Xing, X., Deng, J., Chen, J., et al. “Phase evolution of barium titanate from alkoxide gel-derived precursor,” *Journal of Alloys and Compounds*, V. 384, 2004, pp. 312–7.

168. Vinothini, V., Singh, P., and Balasubramanian, M. “Synthesis of barium titanate nanopowder using polymeric precursor method,” *Ceramics International*, V. 32, No. 2, 2006, pp. 99–103.

169. Last, J. T. “Infrared-Absorption Studies on Barium Titanate and Related Materials,” *Physical Reviews*, V. 105, No. 6, 1957, pp. 1740–50.

170. Shahid, T., Arfan, M., Zeb, A., et al. “Preparation and physical properties of functional barium carbonate nanostructures by a facile composite-hydroxide-mediated route,” *Nanomaterials and Nanotechnology*, V. 8, 2018, pp. 1–8.

171. Zheng, C.-C., Cui, B., You, Q.-M., et al. “Characterization of BaTiO3 Powders and Ceramics Prepared Using the Sol-gel Process, with Triton X-100 Used as a Surfactant.” The 7th National Conference on Functional Materials and Applications. Changsha, Scientific Research Publishing, 2010. pp. 341–6.

172. Parra, R., Góes, M. S., Castro, M. S., et al. “Reaction pathway to the synthesis of anatase via the chemical modification of titanium isopropoxide with acetic acid,” *Chemistry of Materials*, V. 20, No. 1, 2008, pp. 143–50.

173. Socrates, G. “Infrared and Raman Characteristic Group Frequencies.” Third Edition. Chichester, John Wiley & Sons, LTD, 2001. pp. 115–34.

174. Jiang, B., Iocozzia, J., Zhao, L., et al. “Barium titanate at the nanoscale: Controlled synthesis and dielectric and ferroelectric properties,” *Chemical Society Reviews*, V. 48, No. 4, 2019, pp. 1194–228.

175. Wada, S., Yako, K., Kakemoto, H., et al. “Enhanced piezoelectric properties of barium titanate single crystals with different engineered-domain sizes,” *Journal of Applied Physics*, V. 98, No. 1, 2005, pp. 014109-1-014109–7.

176. Alkathy, M. S., Hezam, A., Manoja, K. S. D., et al. “Effect of sintering temperature on structural, electrical, and ferroelectric properties of lanthanum and sodium co-

substituted barium titanate ceramics," *Journal of Alloys and Compounds*, V. 762, 2018, pp. 49–61.

177. Yoon, D.-H. "Ceramic Processing Research Tetragonality of barium titanate powder for a ceramic capacitor application," *Journal of Ceramic Processing Research*, V. 7, No. 4, 2006, pp. 343–54.

178. Su, C. Y., Otsuka, Y., Huang, C. Y., et al. "Grain growth and crystallinity of ultrafine barium titanate particles prepared by various routes," *Ceramics International*, V. 39, No. 6, 2013, pp. 6673–80.

179. Hayashi, H., Nakamura, T., and Ebina, T. "In-situ Raman spectroscopy of BaTiO3 particles for tetragonal-cubic transformation," *Journal of Physics and Chemistry of Solids*, V. 74, No. 7, 2013, pp. 957–62.

180. Dixit, A., Majumder, S. B., Dobal, P. S., et al. "Phase transition studies of sol-gel deposited barium zirconate titanate thin films," *Thin Solid Films*, V. 447, 2004, pp. 284–8.

181. Scalabrin, A., Chaves, A. S., Shim, D. S., et al. "Temperature Dependence of the A1 and E Optical Phonons in BaTiO3.," *Physica Status Solidi*, V. 79, 1977, pp. 731–42.

182. Zamperlin, N., Bottacini, A., Callone, E., et al. "Barium Titanate Functionalization with Organosilanes: Effect on Particle Compatibility and Permittivity in Nanocomposites," *Molecules*, V. 27, No. 19, 2022, p. 6499.

183. Todd, M. G., and Shi, F. G. "Molecular Basis of the Interphase Dielectric Properties of Microelectronic and Optoelectronic Packaging Materials," *IEEE Transactions on Components and Packaging Technologies*, V. 26, No. 3, 2003, pp. 667–72.

184. Bicerano, J., Douglas, J. F., and Brune, D. A. "Model for the Viscosity of Particle Dispersions," *Journal of Macromolecular Science - Reviews in Macromolecular Chemistry and Physics*, V. C39, No. 5, 1999, pp. 561–642.

185. Webb, G. A. "Modern Magnetic Resonance," Springer International Publishing, 2008.

186. Offerdahl, T. J., Salsbury, J. S., Dong, Z., et al. "Quantitation of crystalline and amorphous forms of anhydrous neotame using 13C CPMAS NMR spectroscopy," *Journal of Pharmaceutical Sciences*, V. 94, No. 12, 2005, pp. 2591–605.

187. Garrido, L., Mark, J. E., Sun, C. C., et al. “NMR Characterization of Elastomers Reinforced with in Situ Precipitated Silica,” *Macromolecules*, V. 24, 1991, pp. 4067–72.

188. D’Arienzo, M., Diré, S., Masneri, V., et al. “Tailoring the Dielectric and Mechanical Properties of Polybutadiene Nanocomposites by Using Designed Ladder-like Polysilsesquioxanes,” *ACS Applied Nano Materials*, V. 1, No. 8, 2018, pp. 3817–28.

189. Foran, G., Verdier, N., Lepage, D., et al. “Use of solid-state NMR spectroscopy for the characterization of molecular structure and dynamics in solid polymer and hybrid electrolytes,” *Polymers*, V. 13, No. 8, 2021, p. 1207.

190. Dreiss, C. A., Cosgrove, T., Benton, N. J., et al. “Effect of crosslinking on the mobility of PDMS filled with polysilicate nanoparticles: Positron lifetime, rheology and NMR relaxation studies,” *Polymer*, V. 48, No. 15, 2007, pp. 4419–28.

191. Cosgrove, T., Roberts, C., Choi, Y., et al. “Relaxation studies of high molecular weight poly(dimethylsiloxane)s blended with polysilicate nanoparticles,” *Langmuir*, V. 18, No. 26, 2002, pp. 10075–9.

192. Nhuapeng, W., and Tunkasiri, T. “Properties of 0-3 Lead Zirconate Titanate-Polymer Composites Prepared in a Centrifuge,” *Journal of American Ceramic Society*, V. 85, No. 3, 2002, pp. 700–2.

193. Shrout, T. R., Schulze, W. A., and Biggers, J. V. “Simplified Fabrication of PZT/Polymer Composites,” *Material Research Bullettin*, V. 14, 1979, pp. 1553–9.

194. Meddeb, A., Ounaies, Z., and Lopez-Pamies, O. “Interfacial effects on the electrical behavior of elastomer nanoparticulate composites.” Proceedings of SPIE Vol. 10968. SPIE-Intl Soc Optical Eng, 2019. pp. 109680I1–9.

195. Yang, J., Deng, X. Y., Li, J. B., et al. “Broadband dielectric spectroscopy analysis of dielectric properties of barium titanate ceramics,” *Advanced Materials Research*, V. 744, 2013, pp. 323–8.

196. Hoshina, T., Takizawa, K., Li, J., et al. “Domain size effect on dielectric properties of barium titanate ceramics,” *Japanese Journal of Applied Physics*, V. 47, No. 9 PART 2, 2008, pp. 7607–11.

197. Samet, M., Boiteux, G., Seytre, G., et al. “Interfacial polarization in composite materials with spherical fillers: Characteristic frequencies and scaling laws,” *Colloid and Polymer Science*, V. 292, No. 8, 2014, pp. 1977–88.

198. Zafar, R., and Gupta, N. “Estimation of interface properties in epoxy-based barium titanate nanocomposites,” *Journal of Physics Communications*, V. 5, No. 7, 2021, p. 075003.

199. González, N., Custal, M. dels À., Tomara, G. N., et al. “Dielectric response of vulcanized natural rubber containing BaTiO3 filler: The role of particle functionalization,” *European Polymer Journal*, V. 97, 2017, pp. 57–67.

200. Yu, Y., Huang, B., Zhao, Y., et al. “Enhanced Dielectric Properties of Polydimethylsiloxane Elastomer-Based Composites with Cyanosilicone,” *ACS Applied Polymer Materials*, V. 5, 2022, pp. 259–68.

201. Asandulesa, M., Musteata, V. E., Bele, A., et al. “Molecular dynamics of polysiloxane polar-nonpolar co-networks and blends studied by dielectric relaxation spectroscopy,” *Polymer*, V. 149, 2018, pp. 73–84.

202. Fahmy, T., and Elzanaty, H. “AC conductivity and broadband dielectric spectroscopy of a poly(vinyl chloride)/poly(ethyl methacrylate) polymer blend,” *Bulletin of Materials Science*, V. 42, No. 5, 2019.

203. Damaceanu, M. D., Rusu, R. D., Musteata, V. E., et al. “Insulating polyimide films containing n-type perylenediimide moieties,” *Polymer International*, V. 61, No. 10, 2012, pp. 1582–91.

204. Kuznetsov, N. M., Shevchenko, V. G., Stolyarova, D. Y., et al. “Dielectric properties of modified montmorillonites suspensions in polydimethylsiloxane,” *Journal of Applied Polymer Science*, V. 135, No. 32, 2018, p. 46614.

205. Beena, P., and Jayanna, H. S. “Dielectric studies and AC conductivity of piezoelectric barium titanate ceramic polymer composites,” *Polymers and Polymer Composites*, V. 27, No. 9, 2019, pp. 619–25.

206. Guan, S., Tang, Y., Song, S., et al. “Influence of inter structure of BaTiO3-carbon nanotube hybrid particles on the dielectric properties of PDMS nanocomposites,” *Materials Science and Engineering B*, V. 271, 2021, p. 115280.

207. Yang, D., Ni, Y., Kong, X., et al. “A mussel-like inspired modification of BaTiO3 nanopartciles using catechol/polyamine co-deposition and silane grafting for high-performance dielectric elastomer composites,” *Composites Part B: Engineering*, V. 172, 2019, pp. 621–7.

208. Mahtabani, A., Rytöluoto, I., Anyszka, R., et al. “On the Silica Surface Modification and Its Effect on Charge Trapping and Transport in PP-Based Dielectric Nanocomposites,” *ACS Applied Polymer Materials*, V. 2, No. 8, 2020, pp. 3148–60.

209. Yeung, C., and Vaughan, A. S. “On the effect of nanoparticle surface chemistry on the electrical characteristics of epoxy-based nanocomposites,” *Polymers*, V. 8, No. 4, 2016, p. 126.

210. Li, S., Xie, D., Qu, G., et al. “Tailoring interfacial compatibility and electrical breakdown properties in polypropylene based composites by surface functionalized POSS,” *Applied Surface Science*, V. 478, 2019, pp. 451–8.

211. Lu, C., Lee, W. Y., Shih, C. C., et al. “Stretchable Polymer Dielectrics for Low-Voltage-Driven Field-Effect Transistors,” *ACS Applied Materials and Interfaces*, V. 9, No. 30, 2017, pp. 25522–32.

212. Mellinger, A. “Mellinger: Dielectric Resonance Spectroscopy: Versatile Tool in Quest for Better Piezoelectric Polymers Dielectric Resonance Spectroscopy: a Versatile Tool in the Quest for Better Piezoelectric Polymers,” *IEEE Transactions on Dielectrics and Electrical Insulation*, V. 10, No. 5, 2003, pp. 842–61.

213. Tröls, A., Kogler, A., Baumgartner, R., et al. “Stretch dependence of the electrical breakdown strength and dielectric constant of dielectric elastomers,” *Smart Materials and Structures*, V. 22, No. 10, 2013.

214. Jean-Mistral, C., Sylvestre, A., Basrour, S., et al. “Dielectric properties of polyacrylate thick films used in sensors and actuators,” *Smart Materials and Structures*, V. 19, No. 7, 2010, p. 075019.

215. Vu-Cong, T., Nguyen-Thi, N., Jean-Mistral, C., et al. “How does static stretching decrease the dielectric constant of VHB 4910 elastomer?” Proc. SPIE 9056, Electroactive Polymer Actuators and Devices (EAPAD), vol. 9056. SPIE, 2014. pp. 9056-90561P8.

216. Shanthala, V. S., Shobha Devi, S. N., and Murugendrappa, M. V. “Synthesis, characterization and DC conductivity studies of polypyrrole/copper zinc iron oxide nanocomposites,” *Journal of Asian Ceramic Societies*, V. 5, No. 3, 2017, pp. 227–34.

217. Zhu, S., Sun, H., Lu, Y., et al. “Inherently Conductive Poly(dimethylsiloxane) Elastomers Synergistically Mediated by Nanocellulose/Carbon Nanotube Nanohybrids toward Highly Sensitive, Stretchable, and Durable Strain Sensors,” *ACS Applied Materials and Interfaces*, V. 13, No. 49, 2021, pp. 59142–53.

218. Xu, S., Yu, W., Jing, M., et al. “Largely Enhanced Stretching Sensitivity of Polyurethane/Carbon Nanotube Nanocomposites via Incorporation of Cellulose Nanofiber,” *Journal of Physical Chemistry C*, V. 121, No. 4, 2017, pp. 2108–17.

219. Kim, T., Lim, H., Lee, Y., et al. “Synthesis of BaTiO3nanoparticles as shape modified filler for high dielectric constant ceramic-polymer composite,” *RSC Advances*, V. 10, No. 49, 2020, pp. 29278–86.

220. Cai, C., Chen, T., Chen, X., et al. “Enhanced Electromechanical Properties of Three-Phased Polydimethylsiloxane Nanocomposites via Surface Encapsulation of Barium Titanate and Multiwalled Carbon Nanotube with Polydopamine,” *Macromolecular Materials and Engineering*, V. 306, No. 6, 2021, p. 2100046.

221. Ćirković, J., Vojisavljević, K., Nikolić, N., et al. “Dielectric and ferroelectric properties of BST ceramics obtained by a hydrothermally assisted complex polymerization method,” *Ceramics International*, V. 41, No. 9, 2015, pp. 11306–13.

222. Woo, K., Choi, G. J., Sim, S. J., et al. “Synthesis and characteristics of near-stoichiometric barium titanate powder by low temperature hydrothermal reaction using titanium tetra(methoxyethoxide).,” *Journal of Material Science*, V. 35, 2000, pp. 4539–48.

223. Lee, S. K., Park, T. J., Choi, G. J., et al. “Effects of KOH/BaTi and Ba/Ti ratios on synthesis of BaTiO3 powder by coprecipitation/hydrothermal reaction.,” *Materials Chemistry and Physics*, V. 82, No. 3, 2003, pp. 742–9.

224. Choi, G. J., Lee Sang, K., Woo, K. J., et al. “Characteristics of BaTiO3 particles prepared by spray-Coprecipitation method using titanium acylate-based precursors,” *Chemistry of Materials*, V. 10, No. 12, 1998, pp. 4104–13.

225. Ho Han, Y., Appleby, J. B., and Smyth, D. M. “Calcium as an Acceptor Impurity in BaTiO3.,” *Journal of the American Ceramic Society*, V. 70, No. 2, 1987, pp. 96–100.

226. Zhou, L., Vilarinho, P. M., and Baptista, J. L. “Solubility of Bismuth Oxide in Barium Titanate,” *Journal of the American Ceramic Society*, V. 82, No. 4, 1999, pp. 1064–6.

227. Badapanda, T., Senthil, V., Rana, D. K., et al. “Relaxor ferroelectric behavior of ‘a’ site deficient Bismuth doped Barium Titanate ceramic,” *Journal of Electroceramics*, V. 29, No. 2, 2012, pp. 117–24.

228. Buscaglia, M. T., Buscaglia, V., Viviani, M., et al. “Influence of foreign ions on the crystal structure of BaTiO3,” *J. Eur. Ceram. Soc.*, V. 20, 2000, pp. 1997–2007.

229. Jing, W. A., Ng, B., Xu, G., et al. “Influence of doping on humidity sensing properties of nanocrystalline BaTiO3,” *Journal of Materials Science Letters*, V. 17, 1998, pp. 857–9.

230. Strathdee, T., Luisman, L., Feteira, A., et al. “Ferroelectric-to-relaxor crossover in (1-x)BaTiO3-xBiYbO3 ($0 \leq x \leq 0.08$) ceramics,” *Journal of the American Ceramic Society*, V. 94, No. 8, 2011, pp. 2292–5.